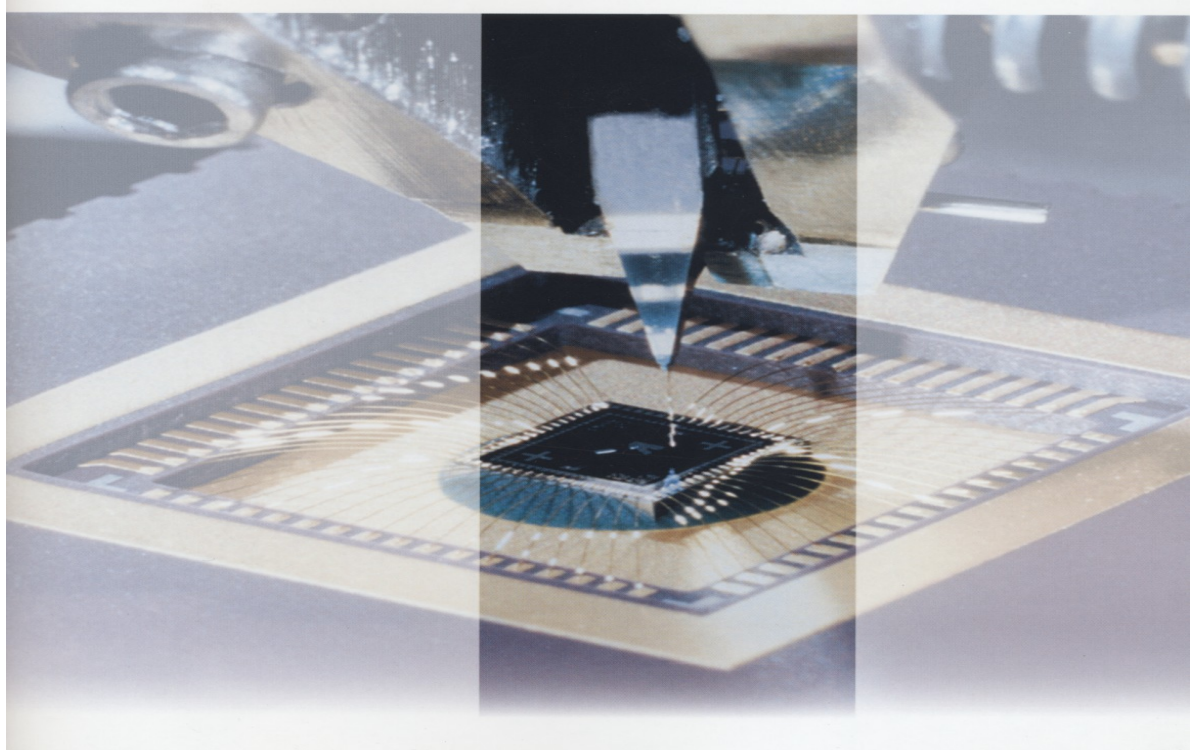


Quantum Rings Produced by Nanolithography with an Atomic Force Microscope

Dissertation Thesis

VLAD – ANDREI ANTOHE



Bucharest, February 2005

**Quantum Rings Produced by
Nanolithography with an Atomic Force
Microscope**

Research Thesis

made in

Institute for Solid State Physics
University of Hannover

supervised by

Prof. Dr. R. J. HAUG and Dipl.-Phys. A. MÜHLE

by

VLAD-ANDREI ANTOHE

Hannover, September 2004

Preface

The desire to explore new orders of magnitude seems to be a part of human nature. This tendency is reflected even in the language. If a particular megadeal is really stunning, we feel more and more obliged to call it a gigadeal. It won't take long before the first Terastar pops up. Each new generation of particle colliders, telescopes, or lasers, in fact of almost any scientific device or technique you can think of, extends the accessible interval of a physical quantity. It is rather the rule than the exception that novel phenomena are discovered in such a process, some of which have been anticipated, others have not. Such an evolution seems to gain speed as soon as it gets classified as useful, besides pure scientific interest. It is of course debatable what exactly should be considered as "useful". In any case, the miniaturization of electronic circuits during the past 50 years has been both scientifically rewarding and useful. It is certainly not necessary to support this statement by examples, since microprocessors are part of daily life. Scientifically, however, the expression "microstructure" no longer fuels our imagination. Meanwhile, the really exciting electronic circuits are *nanostructures*. As this name already suggests, nanostructures are objects with structures in the nanometer regime, which can mean just 1 nanometer, but also just a little less (in fact, in some cases even somewhat more) than 1000 nanometers. This point of nanostructure science is that within the last two decades, tremendous progress has been made in fabricating, controlling and understanding structures in this size regime. This is true for a wide variety of fields, including, for example, gene technology, crystal growth or microchip - excuse me, nanochip - fabrication. The resulting novel possibilities at hand are really breathtaking and get heavily explored by a significant fraction of the scientific community. In many cases, having control over the size and shape of an object in the nanometer regime means being able to control its chemical and/or physical properties. By now, the size reduction has actually reached the dimensions which are of interest for chemistry and biology, and there is a rapidly growing overlap. On the other hand, nanostructure physicists have started to use DNA strands as wires and templates for nanocircuit fabrication.

One branch of nanoscience deals with the electronic transport properties of solid state nanostructures. This field is often referred to as "mesoscopic transport", an expression which indicates that the explanations for the observed transport phenomena must be sought somewhere in between microscopic and macroscopic models.

The text contains many references and citations for encouraging the reader to go through selected, usually quite recent publications. They are referred to by [...] in the text.

This thesis was carried out in the *Institute for Solid State Physics, Nanostructures Department, University of Hannover* from Germany. The stage in this department was financed by the *University of Bucharest, Faculty of Physics* from Romania as a part of the *ERASMUS/SOCRATES National Agency from Romania*.

This work, and with it, its author, has enjoyed a lot of encouragement and support from many sides. I would like to thank particularly Professor Rolf Haug for giving me the opportunity to take part in a very modern and interesting research topic and for supervising my training as well as for guidance during the time spent in this laboratory. I would also like to express my gratitude to the Head of the department for providing the facilities for carrying out this work. I also want to thank the fantastic people in the laboratory for the pleasant environment and for their help in practical problems. A special thought and many thanks for my colleague and friend Alexander Mühle for both the theoretical and practical help. For all the things related with the accommodation, scientific, cultural and social programs during my stage here at Hannover University, I want to thank Professor Olaf Lechtenfeld and Ms. Christel Franko, too. And I want also to thank very much my parents: Prof. Dr. Stefan Antohe and Dr. Felicia Antohe, for their support during my studies, here in Germany, and in the last, but not least, I would like to thank my girl-friend Andreea Popescu for her selfless support.

*Vlad – Andrei Antohe
Hannover, September 2004*

Contents

1	Introduction to Nanotechnology	7
1.1	Nanotechnology and Moore's law	8
1.2	General Speaking	11
1.3	Outline	12
2	Theoretical reviews	15
2.1	Low-dimensional electron systems	15
2.1.1	Two-dimensional electron gas (2DEG)	15
2.1.2	One-dimensional electron system	16
2.1.3	Zero-dimensional electron system	17
2.2	One-dimensional ballistic transport	17
2.3	Tunnelling barriers	21
2.4	Conclusions	23
3	Heterostructures fabrication	25
3.1	Heterostructures	25
3.1.1	Single crystal growth	27
3.1.2	Growth of layered structures	29
3.1.3	Lateral patterning	30
3.1.4	Metallization	34
3.1.5	Bonding	35
3.2	Local depletion of heterostructures	36
3.3	Conclusions	39
4	Nanolithography with an AFM	41
4.1	Atomic force microscope	42
4.1.1	Working procedure	42
4.1.2	AFM modes	44
4.1.3	AFM tips	47
4.2	Controlled nanomachining	50
4.3	Local anodic oxidation of heterostructures	52

4.4	Conclusions	54
5	Experimental procedures	55
5.1	Elements of cryogenics	55
5.1.1	Properties of liquid helium	55
5.1.2	$^3\text{He}/^4\text{He}$ dilution refrigerators	61
5.2	Experimental setup	63
5.2.1	Cryogenic setup	64
5.2.2	Sample probe	64
5.2.3	Electronic setup	65
5.3	Sample preparation	69
5.4	Conclusions	75
6	Experimental results	77
6.1	Basic results	77
6.2	Aharonov-Bohm effect	79
6.2.1	Introduction	79
6.2.2	Transmission through a symmetric ring	81
6.2.3	Transmission through an asymmetric ring	81
6.2.4	Aharonov-Bohm setup and experiments	83
6.3	Shubnikov-de Haas oscillations	90
6.3.1	Landau levels	91
6.3.2	The quantum Hall effect and Shubnikov-de Haas oscillations	92
6.3.3	Measurements of Shubnikov-de Haas oscillations	94
6.4	Other possible phenomena	96
6.4.1	Fano resonances	97
6.4.2	Coulomb blockade regime	98
6.4.3	Kondo effect	98
6.5	Conclusions	100
7	Summary	103
A	The lithoscript-programs	107
B	Symbols and abbreviations	113

List of Figures

1.1	Comparison between micro and macro objects	9
1.2	Moore's Law for size	10
1.3	Moore's Law for transistors	11
2.1	A channel between two gates	18
2.2	The conductance of a QPC	20
2.3	A tunnelling barrier	21
2.4	A real tunnelling barrier	22
2.5	The I-V characteristic of a tunnelling barrier	23
3.1	A typical clean room	26
3.2	A GaAs/AlGaAs-heterostructure	27
3.3	The Czochralski scheme	28
3.4	Growing scheme for GaAs	28
3.5	The Molecular Beam Epitaxy scheme	30
3.6	Different lateral patterning	31
3.7	Contact illumination	32
3.8	Overcut and Undercut profile	33
3.9	Vacuum chamber for etching	34
3.10	Metallization	35
3.11	Ohmic contacts	36
3.12	Wedge bonding	37
3.13	Different band gaps	38
3.14	2DEG depletion	39
4.1	Tip on the surface	42
4.2	The AFM Design	43
4.3	Elements of the AFM. Cantilever and Laser	44
4.4	The force curve	45
4.5	Tapping mode	46
4.6	The AFM tip	47

4.7	A diamond tip	49
4.8	A silicon tip	49
4.9	Results of the engraving	50
4.10	Mechanical nanomachining	51
4.11	Oxidation system	53
4.12	Humidity system	54
5.1	The ${}^4\text{He}$ phase diagram	56
5.2	The superfluid HeII	58
5.3	An osmotic cell	58
5.4	A superfluid film	59
5.5	The ${}^3\text{He}$ phase diagram	60
5.6	The ${}^3\text{He}{}^4\text{He}$ phase diagram	61
5.7	The ${}^3\text{He}{}^4\text{He}$ mixture cryostat	62
5.8	A sample tube	64
5.9	A voltage divider and a low-pass filter.	66
5.10	The block diagram of the experimental setup	68
5.11	Our wafer	70
5.12	A star structure, a hall-bar structure	71
5.13	The AFM picture of two ring structures	74
6.1	Gate-gate plots	78
6.2	A ring structure as a beam splitter.	80
6.3	The transmission t through a symmetric ring.	82
6.4	The transmission t through an asymmetric ring.	83
6.5	The setup for measuring Ahoronov-Bohm effect.	84
6.6	A schematic picture of the ring.	85
6.7	Ahoronov-Bohm oscillations at $T = 18$ mK and $T = 8$ mK . .	86
6.8	Ahoronov-Bohm oscillations dependences for ring 1	88
6.9	Ahoronov-Bohm oscillations dependences for ring 2	89
6.10	Temperature dependence of Ahoronov-Bohm oscillations . .	90
6.11	Density of states of a Landau-quantized 2DEG	91
6.12	Shubnikov-de Haas oscillations and the quantum Hall effect .	93
6.13	SdH and QHE in a GaAs/AlGaAs-heterostructure	94
6.14	The setup for measuring Shubnikov-de Haas oscillations. .	95
6.15	Our Shubnikov-de Haas oscillations	95
6.16	Ring with 2 channels	97
6.17	Fano resonances	98
6.18	Fano resonances in a quantum ring with a dot in the middle .	99

Chapter 1

Introduction to Nanotechnology

The field of semiconductor physics has undergone significant changes in the last decade. Current emphasis is upon using Silicon and III-V semiconductor technology to make structures for the study of electronic and optical properties of systems with reduced dimensionality. Most of the work revolves around is the use of Molecular Beam Epitaxy machines which grow semiconductor layers of very high quality. In particular, it is now possible to produce thin films of Gallium-Arsenide in which, at low temperatures, electrons can travel 10^{-3} cm without being scattered. Under these circumstances the behavior of electrons is entirely wave-like and a range of interference effects can be observed.

The nanoparticles and the nanostructures have generated also much interest in recent years, mainly as a result of quantum confinement effects, a range of intriguing properties of such structures and new applications opened up in all the electronic fields [1]. The miniaturisation of electronic devices has led to rising interest in the transport properties of few atom systems (mesoscopic and nanoscopic systems). In addition, the possibility of studying the properties of very small systems has led to new insights on the interplay between quantum mechanics and physics at the macroscopic level. Molecular devices are the final horizon in the miniaturisation of electronic technology [2]. In nowadays it is possible to arrange atoms into structures that are only a few nanometers in size (1 nanometer is about four atom diameters, or 1/200 of a PentiumTM feature, or 1/50000 of a human hair) [3]. A particularly attractive goal is the self-assembly of nanostructures, which produces large amounts of artificial materials with new properties.

1.1 Nanotechnology and Moore's law

As we just said, it has been always a dream for experimentalists to design confinement potentials for electrons. In semiconductor physics these are realized in quantum structures consisting of up to several millions atoms (e.g. quantum dots, quantum wires, or quantum rings)

During last several decades the interests in nanotechnology have grown rapidly and the semiconductor industry has been progressing according to the Moore's law which predicts the doubling of the number of transistors on a chip, every year. In particular, the Semiconductor Industry Roadmap expects the minimum feature size of 70 nm by the year 2010 [4]. Could one project a classical description of electron transport further down to a scale which becomes comparable with the electron de Broglie wavelength ~ 50 nm in silicon? Is there an end of the Moore's law? The constant driving force from the industry for further device miniaturization is one of the main reasons why significant experimental and theoretical efforts all over the world are currently concentrated on studying the electronic properties of the devices of reduced size and dimensionality. Systems of this size (i.e. 10 nm \sim 1 μ m) are often referred to as mesoscopic. They are much smaller in respect with the macroscopic systems but still larger than microscopic objects like atoms and molecules. On the other hand, they clearly show individual behavior and their transport properties are non-ohmic. At low temperatures the classical description of electron transport in mesoscopic systems may fail completely and quantum effects take over, bringing about fundamental changes in electronic and transport properties of semiconductor structures.

So, what is the Nanotechnology?

The answer to this question varies depending on the person to whom it is asked. But in a broad sense, nanotechnology can be defined as the art of manipulating matter at the atomic scale. It can also be defined as the fabrication of devices with almost atomic precision. The word "nano" is itself derived from the Greek word for midget and means 10^{-9} or a billionth part. One nanometer, $1 \text{ nm} = 10^{-9} \text{ m}$, is roughly the distance from one end to the other of a line of five neighboring atoms in an ordinary solid. Devices with minimum feature size of less than 100 nanometers can be considered to be products of nanotechnology [5]. The nanoscale marks the boundary between the classical and quantum-mechanical worlds. The basic idea behind nanotechnology is that any property has a critical length scale, and when materials are synthesized in sizes that fall below this scale, their properties are dramatically altered. So the nanotechnology deals with natural and artificial

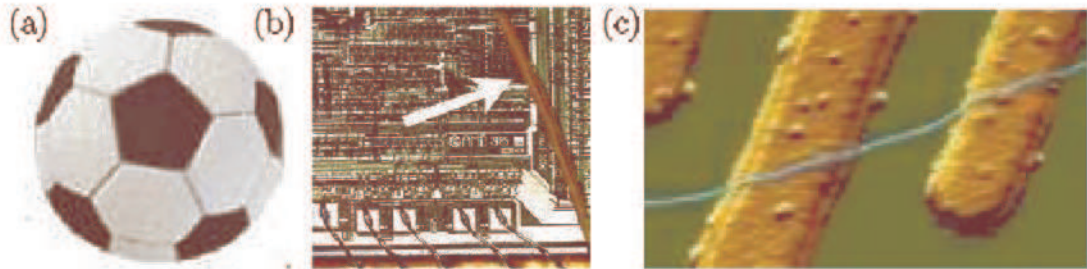


Figure 1.1: (a) A soccer ball with a diameter $\sim 30 \text{ cm} = 3 \times 10^{-1} \text{ m}$. (b) The width of a human hair (here placed on a microchip at the white arrow) is roughly 10^4 times smaller, i.e. $\sim 30 \mu\text{m} = 3 \times 10^{-5} \text{ m}$. (c) The diameter of a carbon nanotube (here placed on top of some metal electrodes) is yet another 10^4 times smaller, i.e. $\sim 3 \text{ nm} = 3 \times 10^{-9} \text{ m}$. [6]

structures on the nanometer scale, i.e. in the range from $1 \mu\text{m}$ down to 10 \AA . The nanometer scale can also be illustrated as in figure 1.1: if the size of a soccer ball ($\sim 30 \text{ cm} = 3 \times 10^{-1} \text{ m}$) is reduced 10000 times we reach the width of a thin human hair ($\sim 30 \mu\text{m} = 3 \times 10^{-5} \text{ m}$). If we reduce the size of the hair with the same factor, we reach the width of a carbon nanotube, for example ($\sim 3 \text{ nm} = 3 \times 10^{-9} \text{ m}$). It is quite remarkable, and very exciting indeed, that we today have a technology that involves manipulation of the ultimate building blocks of ordinary matter: single atoms and molecules [6]

Nanotechnology owes its existence to the astonishing development within the field of microelectronics. Since the invention of the integrated circuit nearly half a century ago in 1958, there has been an exponential growth in the number of transistors per microchip and an associated decrease in the smallest width of the wires in the electronic circuits. As a result extremely powerful computers and efficient communication systems have emerged with a subsequent profound change in the daily lives of all of us. A modern computer chip contains more than 10 million transistors, and the smallest wire width are incredibly small, now entering the sub 100 nm range. Just as the American microprocessor manufacturer, Intel, at the end of 2003 shipped its first high-volume 90 nm line width production to the market, the company announced that it expects to ramp its new 65 nm process in 2005 in the production of static RAM chips [6]. Nanotechnology with active components is now part of ordinary consumer products. Conventional microtechnology is a top-down technology. This means that the microstructures are fabricated by manipulating a large piece of material, typically a silicon crystal, using processes like lithography, etching, and metallization. However, such an approach is not the only possibility. There are other remarkable consequences

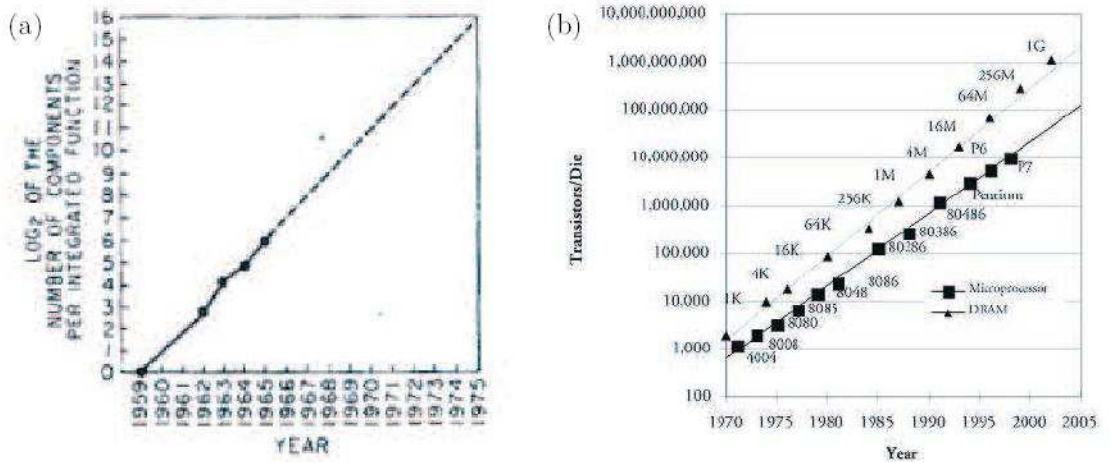


Figure 1.2: (a) Moore's law in the form of the original graph from 1965 suggesting a doubling of the number of components per microchip each year. (b) For the past 30 years Moore's law has been obeyed by the number of transistors in Intel processors and DRAM chips, however only with a doubling time of 18 months. [7]

of the development of microtechnology and nanotechnology.

Since the middle of the 1980, a number of very advanced instruments for observation and manipulation of individual atoms and molecules have been invented. Most notable are the atomic force microscope (AFM) and the scanning tunnel microscope (STM) that will be treated later in this thesis. These instruments have had an enormous impact on fundamental science as the key elements in numerous discoveries. The instruments have also boosted a new approach to technology denoted bottom-up, where it is possible to make small structures over large structures, using the direct writing. The top-down approach to microelectronics seems to be governed by an exponential time dependence. In 1965, when the most advanced integrated circuit contained only 64 transistors, Gordon E. Moore, director of Fairchild Semiconductor Division, was the first to note this exponential behavior in his famous paper *Cramming more components onto integrated circuits*: "When unit cost is falling as the number of components per circuit rises, by 1975 economics may dictate squeezing as many as 65,000 components on a single silicon chip." [7]. He observed a doubling of the number of transistors per circuit every year, a law that has become known as Moore's law and it is illustrated in figure 1.2. Today there exist many other versions of Moore's law. One of them is shown in figure 1.3. It concerns the exponential decrease in the length of the gate electrode in standard CMOS transistors, and relates

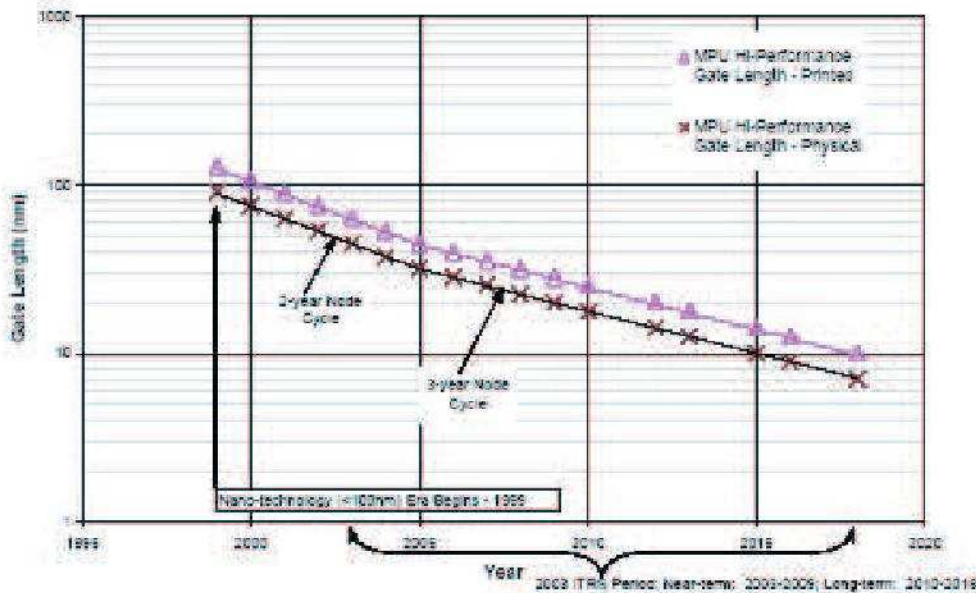


Figure 1.3: Moore's law applied to the shrinking of the length of the gate electrode in CMOS transistors. The length has diminished from about 100 nm in year 2000 to a projected length of 10 nm in 2015. [7]

to the previous quoted values of 90 nm in 2003 and 65 nm in 2005. Naturally, there will be physical limitations to the exponential behavior expressed in Moore's law [7]. However, also economic barriers play a major if not the decisive role in ending Moore's law developments. The price for constructing microprocessor fabrication units also rises exponentially for each generation of microchips. Soon the level is comparable to the gross national product of a mid-size country, and that might very well slow down the rate of progress.

1.2 General Speaking

Two key concepts in solid state physics have enabled the direct fabrication of small quantum structures, investigated in this thesis. The first is the invention of modulation doped GaAs/AlGaAs-heterostructures in 1978 allowing the production of high-quality two-dimensional electron gases (2DEG) [8]. The second milestone was the development of the scanning tunnelling microscope in 1982 by Binnig and Rohrer [9], which allowed the investigation of surfaces with atomic resolution and even the displacement of single atoms [10] in the following years. In 1986 the invention of the atomic force microscope (AFM) [11] boosted the development of the new field of nanotechnology in

all natural sciences ranging from biology to physics. In this thesis we shall combine 2DEG and AFM lithography for a realization of mesoscopic devices, especially quantum rings.

For the observation of quantum mechanical effects one has to shrink the dimensions of a quantum dot to the wavelength of electrons in the material system. Within a 2DEG the typical wavelength of the electrons lies around some ten nanometers which is more than two orders of magnitude longer than in metals. The typical tip of an AFM has a radius of below ten nanometers which is even smaller than the wavelength of the electrons. Therefore, an AFM tip is a natural candidate for the local manipulation of the electronic structure in a 2DEG.

The first demonstration of the depletion of a 2DEG with an AFM was published in 1995 [12] almost one decade after the invention of the AFM. In these experiments the AFM tip induced a local chemical oxidation at the surface of a heterostructure. As a consequence the band structure was distorted locally underneath the created oxide line and the 2DEG was depleted. A completely different technique is the removal of atoms from a surface with an AFM tip used as a nanoscopic engraving tool. This is the most direct method of modifying a 2DEG with an AFM [13].

The advantages of both techniques are obvious, no further processing of the samples is needed, no photo-resist, chemical etching, masks, or metallizations. Additionally, there are no limitations to the device geometry and the accuracy of the lithography lies in the range of a few nanometers. With the controlled nanomachining and the local oxidation a realization of quantum structures in a 2DEG is possible. In addition, we discuss the possibility to create multiple connected topologies with the AFM like rings with an inner and outer boundary. These devices allow to study interference phenomena like the Aharonov-Bohm effect or Fano resonances, where electron-electron correlation effects dominate the transport characteristic.

1.3 Outline

This thesis will start in **Chapter 2** with a theoretical review, concerning the electrons confined to low dimensional conductors, namely two-, one-, and zero-dimensional systems, respectively. As examples for transport phenomena we will discuss the ballistic transport through quantum point contacts and the tunnelling of electrons through potential barriers.

The **Chapter 3** will contain a detailed overview of the GaAs/AlGaAs-heterostructures used as a basis for the realization of the mesoscopic devices. With self-consistent calculations of the band structure of a 2DEG, the deple-

tion of heterostructures, has been described in some papers and this chapter will give a short overview about the principle techniques which are the base for the depletion of 2DEG. This thesis will contain, of course, a lot of references to certain papers, so the interested reader, can see the bibliography and look for papers.

The **Chapter 4** will start with an introduction to the AFM as a tool for investigating surfaces. Afterwards, two AFM techniques used for the direct fabrication of the mesoscopic devices, namely the controlled nanomachining and the local oxidation, will be described. Here you will see a brief overview, of the influence of the writing parameters on the oxide growth at the surface of heterostructures.

In the **Chapter 5** of our thesis, we will discuss our experimental equipment and setup. We will present, first, two different quantum ring structures, which are produced by us and we will present also all the experiments and measurements we have made on these two structures in the **Chapter 6**. This work will be finished with some conclusions about the studied phenomena.

Chapter 2

Theoretical reviews

In this chapter we will review the basic principles of low-dimensional electron systems. We will discuss the density of states of two- and one- dimensional electron gases. And, we will make an introduction to single-particle states in a zero-dimensional potential. In the second part of the chapter we describe two important transport phenomena for our thesis, namely ballistic conductance through quantum point contacts and tunnelling through potential barriers¹.

2.1 Low-dimensional electron systems

2.1.1 Two-dimensional electron gas (2DEG)

Electrons in a three-dimensional periodic potential can be described as plain waves with an energy [13]:

$$E(\vec{k}) = \frac{\hbar^2}{2m^*}(k_x^2 + k_y^2 + k_z^2) \quad (2.1)$$

In this equation, \vec{k} is the wave vector of the electron. Its components $k_i = \frac{2\pi}{\lambda_i}$ are the wave numbers and λ_i ($i = x, y, z$) the wavelength in all three dimensions x, y, z . m^* is the effective mass of the electrons that takes the specific band structure of the crystal into account. In general m^* is a tensor that is defined by the following expression [13]:

$$\left(\frac{1}{m^*} \right)_{ij} = \frac{1}{\hbar^2} \frac{\partial^2 E(\vec{k})}{\partial k_i \partial k_j} \quad (2.2)$$

¹Parts of this chapter are published in Keyser thesis, see ref. [13]

In a parabolic conduction band m^* will not depend on the energy of the electrons and:

$$m^* = m_{xx}^* = m_{yy}^* = m_{zz}^* \quad (2.3)$$

A two-dimensional electron system is created by applying an additional confinement potential $V(z)$ along the z -direction in a crystal. This leads to a quantization of the energy levels $E_z(n_z)$ where n_z is the number of the occupied levels. These levels will be named as subbands in the following. Instead of equation 2.1 we get [13]:

$$E(k_x, k_y, n_z) = \frac{\hbar^2}{2m^*} (k_x^2 + k_y^2) + E_z(n_z) \quad (2.4)$$

Apparently, the electrons can only move freely in the xy -plane perpendicular to the potential $V(z)$.

The density of states (DOS), $D_{n_z}(E)$ in the specific subband n_z in a 2DEG does not depend on the energy [13]:

$$D(E) = 2 \frac{L^2 m^*}{2\pi\hbar^2} \quad (2.5)$$

Here we use $\hbar = \frac{h}{2\pi}$ with h Planck's constant and L the size of the system. The factor two considers the electron spin. $D(E)$ for a system with several occupied subbands is just the sum of the Heaviside function Θ [13]:

$$D(E) = \sum_i D_i(E) = \frac{L^2 m^*}{\pi\hbar^2} \sum_i \Theta(E - E_i) \quad (2.6)$$

In \vec{k} -space, this system is a disc with a radius of $k_F = \sqrt{2\pi n_e}$ with n_e the density of the electrons in the 2DEG. k_F is defined as the wave number at the Fermi energy E_F at zero temperature. With this relation we get for the Fermi energy in a 2DEG:

$$E_F = \frac{\pi\hbar^2}{m^*} n_e \quad (2.7)$$

2.1.2 One-dimensional electron system

With another confinement potential along the y -direction we can further restrict, free motion to the x -axis of the system. The energy of the electrons is then quantized in the y and z -direction [13]:

$$E(k_x, n_y, n_z) = \frac{\hbar^2 k_x^2}{2m^*} + E_y(n_y) + E_z(n_z) \quad (2.8)$$

Each pair of n_y and n_z denotes a specific one-dimensional (1D) subband in this system. To simplify, we assume for the following considerations that $n_z = 1$ and the number of the occupied 1D-subbands depends only on n_y . The density of states $D(E)$ has to be modified [13]:

$$D(E) = 2 \frac{L}{\pi \hbar} \sqrt{\frac{m^*}{2E}} \quad (2.9)$$

The main difference to the two-dimensional electron gas is that the density of states is proportional to $\frac{1}{\sqrt{E}}$ instead of being constant. We will later see that this dependence has an important consequence for the transport through an 1D-system [13].

2.1.3 Zero-dimensional electron system

With a third confinement potential $V(x)$, the electrons are bound to a quasi zero-dimensional region of space. If $V(x)$, $V(y)$ and $V(z)$ are of the parabolic form, the energy of the electrons is quantized [13]:

$$E(n_x, n_y, n_z) = \hbar\omega_x \left(n_x + \frac{1}{2} \right) + \hbar\omega_y \left(n_y + \frac{1}{2} \right) + \hbar\omega_z \left(n_z + \frac{1}{2} \right) \quad (2.10)$$

with $n_i = 0, 1, 2, \dots$ the number of occupied levels in each direction and $\hbar\omega_i$ the energy of the harmonic oscillator that denotes the separation of the levels ($i = 0, 1, 2, \dots$). All energies are discrete and thus the electron is confined in the potential.

The density of states, $D(E)$ in a 0D-system is the sum over Dirac δ -functions [13]:

$$D(E) = 2 \sum_{n_x, n_y, n_z} \delta[E - E(n_x, n_y, n_z)] \quad (2.11)$$

The pre-factor considers the two-fold degeneracy of each state due to the electron spin.

In semiconductor physics such a system is often named quantum dot (QD) or even artificial atom because of the similarities with the energy spectra of real atoms [13].

2.2 One-dimensional ballistic transport

One possibility to create a one-dimensional system is to cut a narrow wire out of a 2DEG. On the left-hand side of figure 2.1 a schematic picture of a 1D-channel in a two-dimensional electron gas is depicted. The solid black

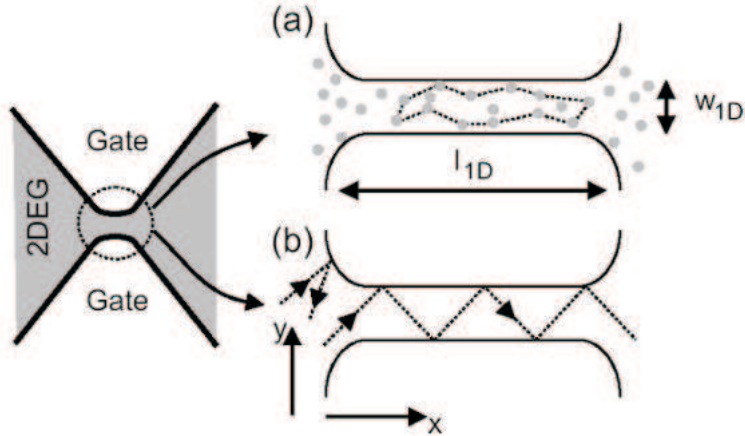


Figure 2.1: Microscopic picture of the channel between two gates: (a) diffusive transport regime ($l_e \ll l_{1D}$); (b) ballistic transport regime ($l_e \gg l_{1D}$) [13].

lines indicate insulating regions separating the gates from the rest of the 2DEG depicted in grey. The density of the electrons in the constriction and thus the electronic width w_{1D} is controlled by the voltages applied to the gates. Such a device works in principle like a field-effect transistor that is laid out flat on a surface.

Inside a constriction in a 2DEG a quasi one-dimensional channel of length l_{1D} and width w_{1D} might be formed. In the following we assume that w_{1D} is smaller compared to all other quantities. The channel is directly coupled to the two-dimensional reservoirs. A qualitative microscopic picture is shown in figure 2.1(a)+(b). The transport characteristic of such a system is classified in three different regimes: diffusive, quasi-ballistic, or ballistic [14].

The system is diffusive if the mean free path l_e of the electrons is smaller than the length of the channel: $l_e \ll l_{1D}$, figure 2.1(a). l_e is governed by scattering of electrons on impurities (indicated by the grey circles in figure 2.1(a)) or a rough surface of the channel boundaries. In a quasi-ballistic system l_e is larger than w_{1D} but still smaller than l_{1D} . When impurities are absent in the channel and its boundaries are smooth on the length scale defined by the Fermi wavelength of the electrons $l_e \gg l_{1D}$ follows. In this regime the electrons are ballistically transmitted through the channel and the scattering at the boundaries is specular, figure 2.1(b). In other words, due to the absence of scatterers all electrons that enter the channel will be transmitted through it which results in a transmittance $T = 1$ of the channel. In our experiments we will define very short channels of a few ten nanometers length. These kind of devices are known as ballistic quantum point contacts

(QPC). We will calculate the conductance G through a QPC. In a ballistic regime, the conductance through a classical point contact was first derived by Sharvin [15]:

$$G = \frac{2e^2}{h} \frac{k_F w_{1D}}{\pi} = \frac{2e^2}{h} \frac{2w_{1D}}{\lambda_F} \quad (2.12)$$

where $k_F = 2\pi/\lambda_F$ is the Fermi wave vector and λ_F the Fermi wavelength at E_F . The conductance is limited by scattering of the incident electrons at the entrance of the constriction and thus scales linearly with w_{1D} .

Quantum mechanical effects lead to deviations from a continuous dependence of G on w_{1D} when the Fermi wavelength λ_F of the electrons is comparable to the width of the point contact w_{1D} . As a consequence one obtains a quantized conductance. In a typical GaAs/AlGaAs-heterostructure used here we get $\lambda_F \sim 50$ nm, therefore the electronic width of a quantum point contact should be smaller than a few 100 nm to observe quantization.

A simplified explanation for the quantization of G in units of $2e^2/h$ is the formation of discrete energy levels inside the quantum point contact that are accessible for transport. By assuming a harmonic confinement potential perpendicular to the current direction the eigenvalues of the energy in the quantum point contact have the form [14]:

$$E(k_x, n_y) = \frac{\hbar^2 k_x^2}{2m^*} + \left(n_y + \frac{1}{2} \right) \hbar\omega_0 \quad (2.13)$$

which contains a free-electron kinetic energy in the longitudinal x-direction (parallel to the current flow). The energy levels are equally spaced with $\hbar\omega_0$. Since the electrons can only move freely in the x-direction this leads to quasi one-dimensional subbands. Each subband is characterized by a specific transmission coefficient T_n . Electrons can only pass the point contact if their energy matches the energy of the occupied subbands in the QPC.

We calculate the net current I flowing through a point contact with N occupied subbands at zero temperature. I is obtained by integrating over all electronic states between the electrochemical potentials of the source and drain contacts μ_S, μ_D :

$$I = e \sum_{n=1}^N \int_{\mu_D}^{\mu_S} dE \frac{1}{2} \frac{dN_n}{dE} v_n(E) T_n(E) \quad (2.14)$$

Again T_n is the transmission probability of each subband that is accessible for the electrons. The product of the 1D-density of states $dN_n/dE = 2/\pi \cdot (dE_n/dk_x)^{-1}$ and the velocity of the electrons $v = 1/\hbar \cdot (dE_n/dk_x)$ yields

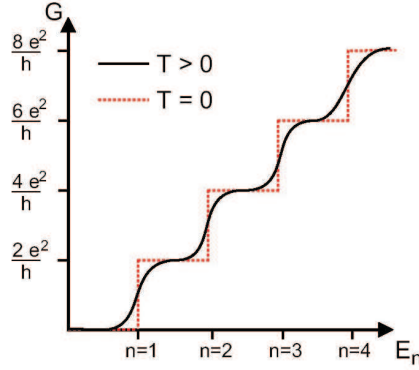


Figure 2.2: Conductance G of a ballistic quantum point as function of the number of occupied subbands n at temperature $T = 0$ and $T > 0$.

$(dN_n/dE_n) \cdot v_n = 4/h$. Formula 2.14 is simplified with this result and we calculate the conductance $G = I/V$ of the QPC to:

$$G = \frac{2e^2}{h} \sum_{n=1}^N T_n \quad (2.15)$$

which is the so-called *two-terminal Landauer-formula*. In the ballistic regime the transmission probability is $T_n = 1$ for $n = 1 \dots N$ with N the maximum number of populated subbands. According to these considerations the conductance is quantized:

$$G = \frac{2e^2}{h} N \quad (2.16)$$

The above considerations are valid at zero temperature ($T = 0$) and lead to sharp steps in the conductance G through a QPC as a function of the number of occupied subbands as shown in figure 2.2 by the dashed line. At finite T the steps are smeared out because of the Fermi-Dirac distribution of the electrons in the contacts is given by:

$$f(E) = \frac{1}{\exp\left(\frac{E-E_f}{k_B T}\right) + 1} \quad (2.17)$$

with k_B the Boltzmann constant. An ideal characteristic at finite temperature is shown by the solid line in figure 2.2.

Scattering in the quantum point contact, either at rough boundaries or impurities, lead to deviations from the ballistic case. If defects are present in the constriction the T_n of the subbands will differ. This will distort the characteristic and the clear quantization of the conductance is lost.

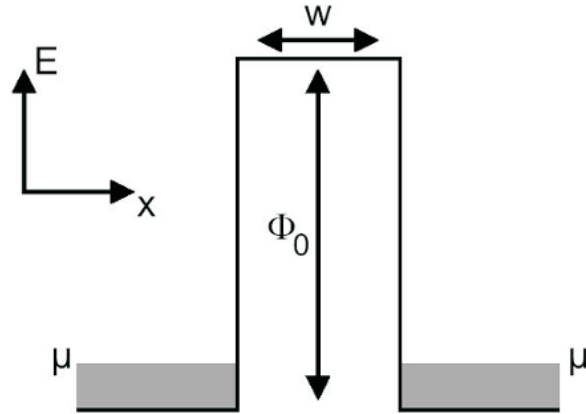


Figure 2.3: Idealized tunnelling barrier shown for an electrochemical potential $\mu \ll \Phi_0$ in the contacts.

2.3 Tunnelling barriers

After this short introduction to one-dimensional ballistic transport we introduce the tunnelling through potential barriers.

A potential or tunnelling barrier is described by its energetic height Φ_0 and the width w . A simple idealized example is shown in figure 2.3. A rectangular tunnelling barrier separates a continuum of electronic states that contain electrons up to the electrochemical potential μ indicated by the grey region, depicted at zero temperature $T = 0$ K. In a classical picture all incident electrons with a certain energy $E < \Phi_0$ are reflected at the barrier. Classical particles can only pass the barrier when their energy exceeds Φ_0 . In contrast, the quantum mechanical calculation of the transmission coefficient t results in $t > 0$ for a barrier with finite height even for electrons with $E < \Phi_0$: the electrons can tunnel through the barrier. The calculation of t in dependence of Φ_0 and w yields for $E < \Phi_0$ [16]:

$$t \propto \exp \left(-w \sqrt{\frac{2m^*}{\hbar^2} (\Phi_0 - E)} \right) \quad (2.18)$$

This result is only valid if the wavelength of the electrons λ is much shorter than the barrier width.

We are interested in the current-voltage (I-V) characteristic of a real tunnelling barrier as shown in figure 2.4 (a). In our case, a real barrier situated in a realistic semiconductor will be distorted compared to figure 2.3 because free electrons will screen the potential. This leads to an effective rounding of the barrier shape. This can be simulated by self consistent

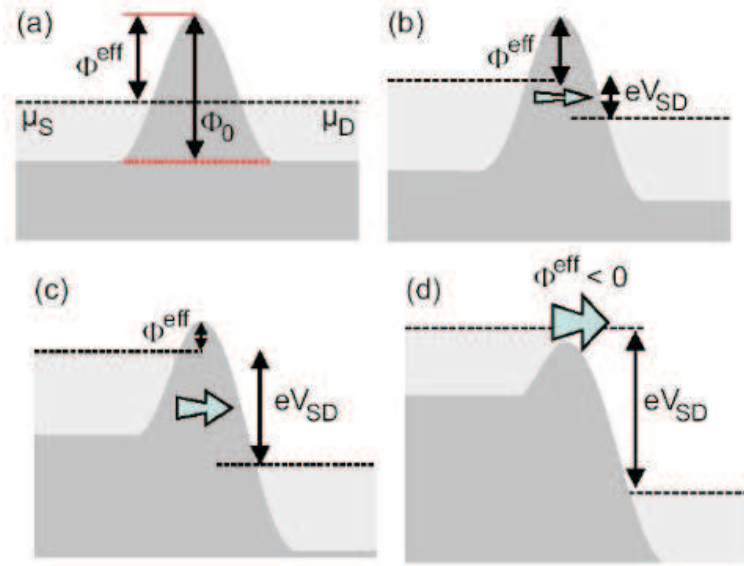


Figure 2.4: Tunnelling current through a barrier at different source-drain bias V_{SD} . The effective barrier height Φ^{eff} and Φ_0 change both with variation of V_{SD} .

calculations. Examples for real barriers is a two-dimensional electron gas can be found e.g. in the work of Peck [17].

A real barrier with different applied bias voltages is shown in figure 2.4. At zero bias ($V_{SD} = 0$), the electrochemical potentials μ_S , μ_D in the source and drain contacts are equal, figure 2.4(a). By raising V_{SD} ($\mu_S > \mu_D$) a current will start to flow eventually through the barrier, because empty states exist on the other side of the barrier, figure 2.4(b).

There is an additional effect for the real barrier: its effective height Φ^{eff} above the electrochemical potential in the source contact μ_D is reduced by an amount $\Delta\Phi = \alpha eV_{SD}$ with e the elementary charge and α a voltage-to-energy conversion factor. In general, the voltage drop over the barrier will be linear and in the case of a symmetrical barrier it follows $\alpha = 0.5$. This is depicted in figure 2.4 (b). For an asymmetric barrier α will be smaller than 0.5.

With even higher V_{SD} , Φ^{eff} is further reduced (figure 2.4(c)) and the tunnelling current grows accordingly. If Φ^{eff} falls below zero, the barrier is reduced to an ohmic resistor with a resistance $R = dV_{SD}/dI_{SD}$, and the current grows according to Ohm's law $I_{SD} = V_{SD}/R$ linearly for $eV_{SD} \gg \Phi_0$, figure 2.4(d).

The resulting IV-characteristic is shown in figure 2.5 for two symmetric

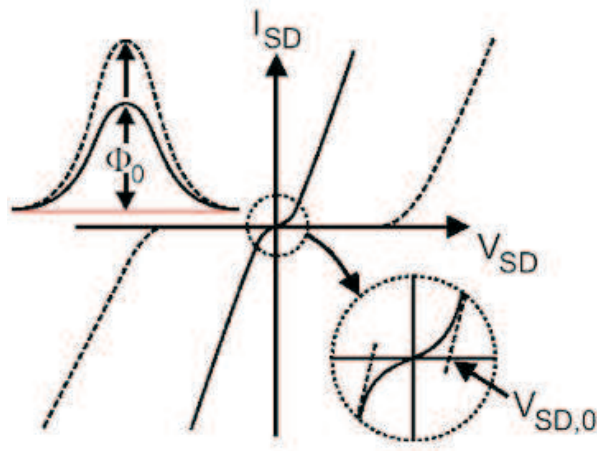


Figure 2.5: IV-characteristic of two tunnelling barriers with different height Φ_0 .

tunnelling barriers with the same width but different heights Φ_0 as shown in the upper left inset. The dashed line depicts the characteristic for the higher barrier, in which the tunnelling current is suppressed over a wide voltage range around $V_{SD} = 0$ (solid line in figure 2.5). Φ_0 can be estimated by extending the linear region of the characteristic to $V_{SD,0}$ at $I_{SD} = 0$, as indicated in the lower right inset of figure 2.5. For a symmetrical tunnelling barrier ($\alpha = 0.5$), $V_{SD,0}$ will be identical for both bias directions and thus:

$$\Phi_0 = 0.5eV_{SD,0} \quad (2.19)$$

This is a very simplified method for the estimation of Φ_0 . For an exact determination of α and Φ_0 temperature dependent measurements of the tunnelling current are required [18].

2.4 Conclusions

In this chapter, we saw that without any confinement, the electrons are free to move in all three dimensions (x, y, z). But if we apply a confinement potential along the x, y or z -direction, respectively, we can force the electrons to move only in 2, 1 or 0 dimensions, resulting 2DEG, 1DEG or 0DEG.

In fact the 2DEG can be formed only at very low temperatures (few K), we will talk later about this (see chapter 3). The other confinements for the electrons, are created using different technics such as the so-called local anodic oxidation or scratching. We create with these technics the tunnelling barriers described in section 2.3. With these tunnelling barriers we can confine the electrons to move only in a 1D and quasi 0D system.

Chapter 3

Heterostructures fabrication

In this chapter we describe the basis for all our experiments, namely two-dimensional electron gases (2DEG) in GaAs/AlGaAs-heterostructures. We also will introduce the experimental tools and technics involved in fabricating nanostructures. The major of the mesoscopic devices are made of semiconductor heterostructures. We will talk also about the depletion of the two dimensional electron gas, which is the base for creating this mesoscopic devices¹.

3.1 Heterostructures

Fabricating nanostructures for mesoscopic transport experiments is a major technological challenge. The requirements concerning material purity, lithographic resolution and process control are at the edge of present-day technology.

Silicon dominates in industry, while GaAs and other materials are essentially only used where silicon devices are significantly less useful, like in optoelectronics or in ultra-high speed, ultra-low noise applications. From a technological point of view, Si has several major advantages. First of all, the raw material is quartz sand, easily available and cheap. Second, its high mechanical stability simplifies all process steps. A very important point is the fact that Si can be easily oxidized into SiO_2 , which has excellent mechanical and electronic properties, like high breakdown electric fields and large resistivities. GaAs oxides, on the other hand, have poor electronic properties and are more or less useless for most electronic applications, like in capacitors [19].

¹Parts of this chapter are published in Thomas Heinzel book and in Keyser thesis, see ref. [19, 13]



Figure 3.1: A picture of typical cleaning room [20].

During fabrication, we have to prevent that dust particles hit the crucial area, since they may cause defects in the lithographic patterns, which get transferred into the nanostructure in subsequent process steps. Therefore, processing is usually done in a clean room in which the air is heavily filtered. Clean rooms are classified by the number N of dust particles per cubic foot, sized larger than 500 nm. For example, a class 100 clean room contains $N=100$ of such particles in one cubic foot. It is true that feature sizes have been scaled down to well below 500 nm, and along with this, the size of the relevant dust particles has decreased accordingly. Nevertheless, the clean room class as defined above is a useful quantity, as the particle size distributions in air are well known. You can see such a clean room in figure 3.1. Mesoscopic researchers typically fabricate a small number of individual samples, with an active area below a square millimeter. Of course, it is much harder to keep a 4 inch wafer free of dust particles, and the demands posed on an industrial clean room are much higher. Furthermore, although a high sample yield is desirable in research as well, a research lab has no problems living with yields below 100 %.

Figure 3.2 shows a processed GaAs/AlGaAs-heterostructure. It becomes immediately apparent that a whole bunch of fabrication steps is required. To begin with, the semiconductor heterostructure must be grown. This involves single crystal growth, plus some sort of epitaxy to add the layers of different materials. Next, a piece of the wafer has to be processed by lateral lithography. The two-dimensional electron gas is contained in the mesa, which should have a suitable geometry. Ohmic contacts and gate electrodes have to be patterned. Finally, wires must be connected to the electrodes. We will discuss these fabrication steps below. Although the details of the processes depend on the material used, the technological concepts are similar.

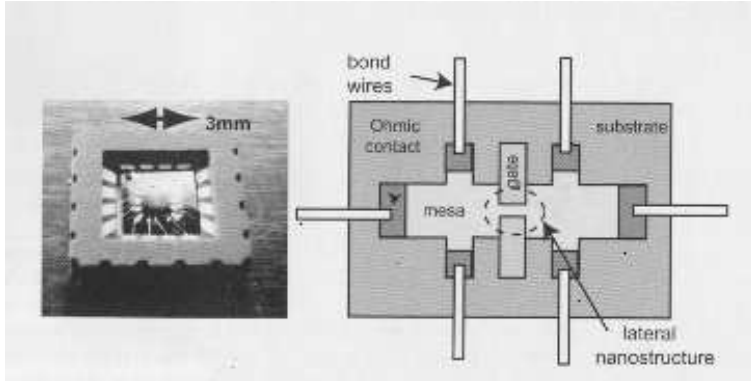


Figure 3.2: Left: photograph of an assembled GaAs/AlGaAs-heterostructure. The chip resides inside a ceramic chip carrier. Electric contacts between the carrier and the chip are made by bonded wires. The chip-carrier has a size of 5 mm x 5 mm. Right: schematic components of a typical microchip designed for mesoscopic transport measurements [19].

3.1.1 Single crystal growth

A standard method to grow single crystals is the so-called Czochralski method, figure 3.3. A small single crystal (the seed, which also determines the crystal direction) is immersed in a purified melt. The atmosphere should be inert; an argon atmosphere is often used. The seed is rotated ($\omega \approx 2\pi s^{-1}$) and slowly (with a speed of, say 1 mm/s) pulled out of the melt. The pulling speed determines the diameter of the crystal cylinder, which may be as large as 10 inches. A typical length is 1 m. GaAs is a binary material and as such more difficult to grow. A general problem with multi-component melts is the different vapor pressure of the components. In order to avoid compositional changes of the melt over time, the vapor pressures must be controlled. In case of GaAs, As has an overpressure of 0.9 bar, while e.g. in InP, the P overpressure is 60 bar. Two methods are common for compensating the overpressures. In the liquid encapsulated Chochralsky (LEC) technique, the melt is covered with a fluid that does not intermix, figure 3.4 (a). As a result, no gas can escape from the melt. In the Bridgman technique, the melt resides in a closed quartz tube, in which the correct As overpressure is established by heating solid As outside the melt to the corresponding temperature, figure 3.4 (b). Here, the crystal is grown by moving the melt along a suitable temperature gradient and at an appropriate speed [19].

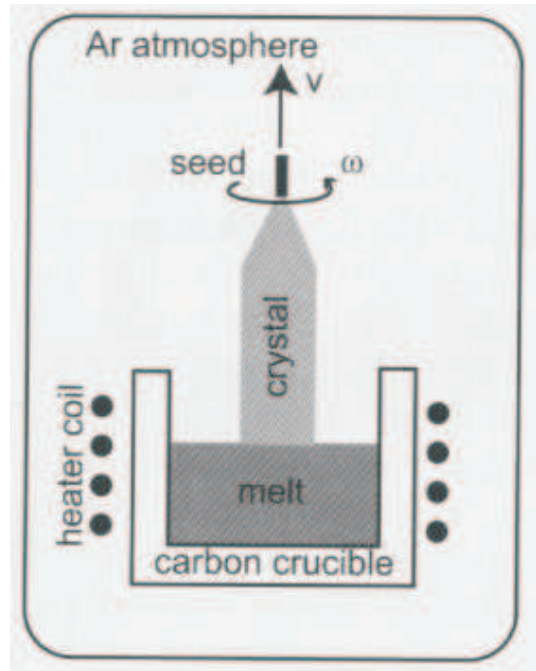


Figure 3.3: The Czochralski scheme for crystal growth used to grow Si single crystals. The angular velocity and the velocity are ω and v , respectively.

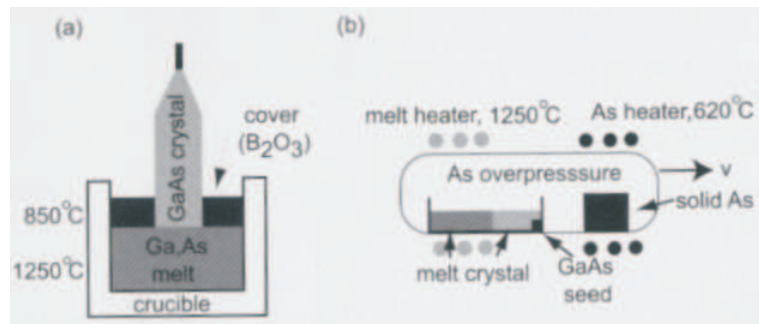


Figure 3.4: Schemes for growing of two-component crystals, such as GaAs. (a): in the technique (LEC), the melt is covered by an impenetrable liquid. The crystal is pulled through this cover layer. In the Bridgman technique (b), a closed tube contains a crucible that hosts the melt, a seed and the freshly grown crystal, as well as a piece of solid As. The temperature of the solid As is kept at a temperature that corresponds to an As overpressure of 0.9 bars. The melt solidifies at the location where the spatially varying temperature reaches 1238 °C. Crystal growth is established by moving the tube along the temperature profile.

3.1.2 Growth of layered structures

Pulling a crystal out of a melt is perfect for fabricating substrates, which are usually obtained by cutting the crystal cylinder into thin disks called wafers. A typical substrate thickness is $300\text{ }\mu\text{m}$, while surfaces roughnesses of a few nanometers can be achieved by mechanical polishing. These technics are not suited to grow layered structures, such as a GaAs/AlGaAs-heterostructure. Here, one need something that ideally provides ultra-clean growth of individual monolayer, and the material composition must be controllable. Several techniques are established for fabricating layered semiconductor structures, such as: "Metal organic chemical vapor deposition" (MOCVD), or "Molecular beam epitaxy" (MBE). A disadvantage of the first method is the high toxicity of the gases involved. In addition, the material grown is not so clean as that one obtained with the second method (MBE). Our heterostructure was grown using the molecular beam epitaxy technique by the *Walter-Schottky Institute*, that is why I will give a brief presentation of this technique.

The atomic layers are grown in a ultra-high vacuum chamber, with pressures of the order of 10^{-11} mbars . A substrate is inserted in the UHV chamber, heated and slowly rotated (figure 3.5). The components of the semiconductor are supplied by effusion cells, which can be individually heated to provide the flux needed, as well as opened and closed. For growing standard GaAs-heterostructures, for example Ga, As, Al and Si (for n-doping) effusion cells are needed. This way, monolayer by monolayer of the crystal can be grown, which can be selectively doped: the modulation doping can be easily incorporated. And also the modulation doping will give the position of the 2DEG. Typical growth rates are 0.1 mm/s . The growth can be calibrated and monitored with RHEED, which is an acronym for reflection of high-energy electron diffraction. Here, an electron beam with an energy of about 10 keV hits the surface under a very small angle (a degree or so), and gets reflected at the surface. Its penetration depth is a few monolayers only, such that the reflected interference pattern is highly sensitive to the roughness and the crystal structure of the surface. The reflected intensity shows a minimum if the coverage of the monolayer is 50 %, which corresponds to maximum roughness. When a monolayer has just been completed, the scattering has the highest specularity, and the reflected intensity shows a maximum. Although MBE is very expensive and time-consuming, it is widely used to grow heterostructures for mesoscopic transport experiments, since the quality of the samples is unsurpassed by any other methods. The high pressure is needed to make the residual gas monolayer formation time sufficiently large [19].

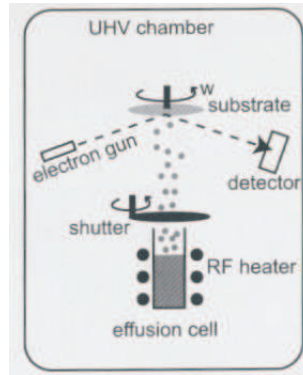


Figure 3.5: Schematic view into a UHV chamber for molecular beam epitaxy (MBE).

3.1.3 Lateral patterning

The special MBE techniques for lateral growth are by no means standard technology. It is more usual to grow a heterostructure with two-dimensional translation invariance parallel to the surface, and pattern the nanostructure subsequently by some sort of lateral processing.

Examples for typical sequences of process steps are given in figure 3.6. Column (a) is typical for many Si fabrication steps. The substrate is covered with a homogenous metal layer, which is subsequently coated with a suitable resist. Illumination development of the resist through a mask exposes some areas of the metal layer, while others are protected by the resist. The illumination is usually carried out with ultraviolet light or with electrons. An etch step follows, which selectively removes the free metal surfaces. Here, the resist acts as an etch mask. Finally, the resist gets removed and a patterned metal layer on the substrate results. This technique is rarely ever used in GaAs processing, since essentially all suitable metal etchants attack GaAs as well. Therefore, fabrication scheme (b) is typically used. Here, the substrate is first covered by resist, which gets illuminated and developed. Now, the metal is evaporated on the substrate, with the patterned resist acting as evaporation mask. The lift-off step follows, i.e., the resist is removed with the metal film on top. The final result is identical to that one of scheme (a). For selective etching of the substrate (c), steps 1 to 3 are identical to (b). Then, the pattern resist is used as an etch mask for the substrate. In the following, these fabrication steps are given in further detail.

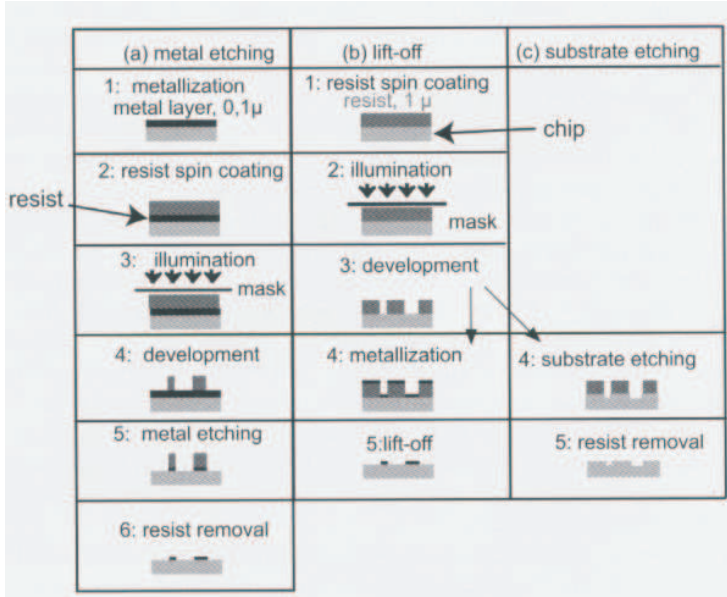


Figure 3.6: Comparison of different lateral patterning schemes for semiconductors [19].

Defining patterns in resists

The two standard techniques for imposing a pattern into a resist are optical lithography and electron beam lithography. We have used in our work the optical lithography, so we will talk more about this.

By this technique we mean illumination of a photoresist by visible or ultraviolet light. The sample is coated with a thin and homogenous photosensitive resist. This is done by dropping some resist solution onto the sample, which is then rotated for about one minute at high speed, typically a few thousand rpm. The spinning speed and the viscosity of the solution determine the thickness of the resist layer, which is of the order of 1 micron. After baking the resist, the sample is mounted into a mask aligner, a device designed for adjusting the sample with respect to a mask that contains the structure to be illuminated. The mask aligner is equipped with a strong light source that illuminates the resist film through the mask, see figure 3.7. The pattern sizes are Doppler limited, which means that the smallest feature sizes are about half the wavelength (≈ 150 nm), divided by the index of refraction of the resist (≈ 1.5), which limits the resolution to roughly 100 nm. The mask can be a quartz plate coated with a thin chromium film, which contains the pattern to be illuminated. In the contact illumination scheme, the Cr film is in mechanical contact with the resist and blocks the light, such

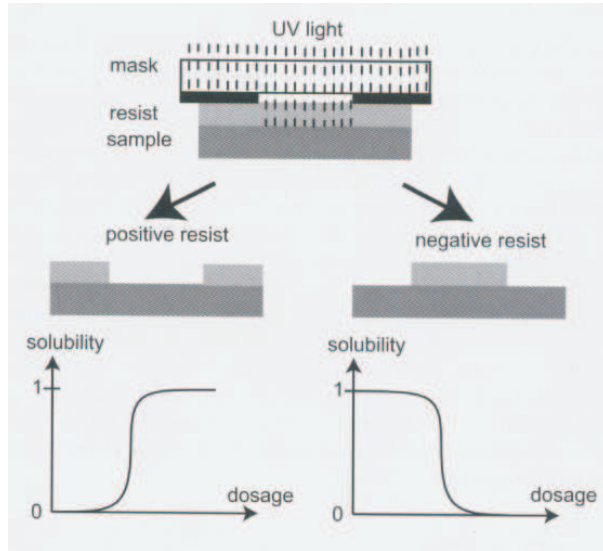


Figure 3.7: Top: contact illumination. The mask pattern is transferred into the resist via illumination and subsequent development. Center: resulting resist cross section for positive (left) and negative (right) resist. Bottom: Solubility characteristic for the two resist types.

that the resist underneath the Cr remains unexposed.

During contact illumination, the mask suffers contaminations due to dust particles on top of the resist, as well as by resist adhesion. This can be avoided by projection illumination, where the mask pattern is transferred into the resist via lenses. This technique is widely used in industry, but somewhat unusual in research labs [19].

The photoresist can be classified as positive and negative. The solubility of the exposed areas increases for a positive resist, while it decreases in negative resist, see figure 3.7. Immersing the sample into a suitable developer removes the corresponding sections of the resist film. Both types of resists have in common that their solubility as a function of the illumination dosage is a step-like function. This ensures high resolution and sharp edge profiles. It may seem irrelevant at first, what kind of resist is used in a particular process. There may, however, be some process specific requirements which favor one type or the other. Most importantly, negative resist predominantly produces an undercut profile, which means that after development, the resist area in contact with the sample is smaller than the area at the resist surface, figure 3.8. This is a consequence of the approximately exponentially decreasing intensity of the illumination light as it penetrates into the resist. An undercut profile is highly desirable for subsequent metallization steps,

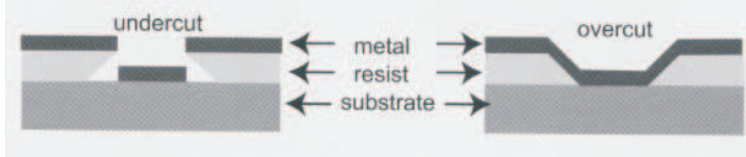


Figure 3.8: Overtcut (left) and undercut (right) resist profile after illumination, development, and surface metallization.

in which the resist itself serves as mask. After the metallization, the resist including the metal film on top usually has to be removed in a lift-off step, which is bound to fail for resists with an overcut profile, since the metal on the sample and that one on top of the resists are connected. An undercut profile avoids this problem, provided the thicknesses of metal layer and resist are properly selected. In principle, the resolution can be increased by using shorter wavelengths. In X-ray lithography, resists are illuminated with wavelengths in the 10 nm regime. While significant progress has been achieved over the past decade, severe technological obstacles have to be overcome before this version of optical lithography can be widely used. Photoelectrons limit the resolution to several 10 nm, and optical components as well as masks are difficult to fabricate, since metals get transparent in the UV. The ultimate limit of such lithographic techniques is set by the resolution of the resist, which contain organic polymers. The cross linking of the polymers is enhanced or reduced by the light, which modifies their solubility accordingly. Thus, the resolution cannot become better than the size of the corresponding monomers, which is of the order of 0.5 nm. For feature sizes between ≈ 150 nm, electron beam lithography is the current technique of choice [19].

Etching

An important technique of transferring the resist pattern into the sample is etching. Patterned resists can be used as etch masks, provided the etchant is sufficiently selective. We distinguish between dry etching and wet chemical etching.

1. Dry etching

The setup for dry etching techniques consists of a vacuum chamber with two electrodes at the top and the bottom. The sample is placed at the bottom, which may be the anode or the cathode, depending on the process. A gas discharge is ignited, and the ions of the etch gas hit the sample, figure

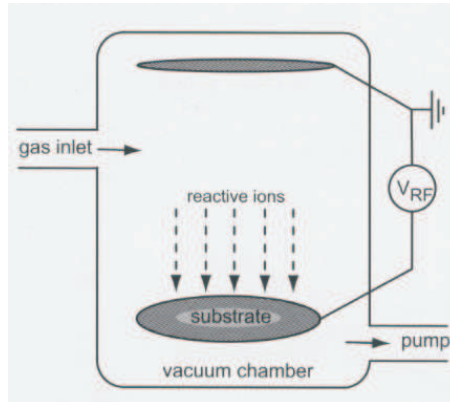


Figure 3.9: Scheme of a vacuum chamber for reactive ion etching.

3.9. One speaks of plasma etching if the reaction is purely chemical. Oxygen plasma etching is often used to remove resists layers. The low energy ions avoid damage of the semiconductor and metal components of the sample [19].

2. Wet chemical etching

Wet chemical etching means immersing the sample in a suited etchant solution. In contrast to metals, the majority of the common semiconductors are not attacked by pure acids. Therefore, the etch typically consists of a mixture of an oxidizer, such as H_2O_2 , an acid, like HCl , and water. H_2O_2 oxidizes the semiconductor, while the acid removes the freshly formed oxide. The oxidation and etch rates depend on the etch composition as well as on the crystal direction. The resulting edge profile can thus be tuned accurately. For many purposes, an overcut edge profile is desirable, since often, thin metal layers have to be deposited on the surface later on. A metal layer thinner than the etched depth may get disconnected across an etched step with undercut profile [19].

3.1.4 Metallization

By metallization, we mean the deposition of metal films on the semiconductor surface. This is usually done by evaporation of the metal in a vacuum chamber. The metals are molten (or sublimed, respectively) in a crucible made of tungsten or carbon, which can be done by heating the crucible with a current, or by focussing an electron beam onto the metal, see figure 3.10. At sufficiently large temperatures, the metal vapor pressure is so high that

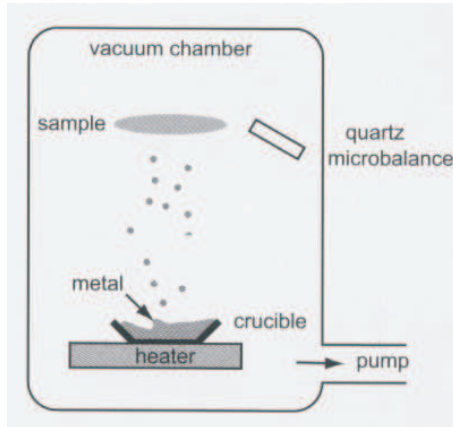


Figure 3.10: Scheme of an evaporation system for metallizations.

a metal film grows at the exposed surfaces with a rate of the order of one nanometer per second. The film thickness is monitored by an oscillating quartz plate. As the metal gets deposited on the quartz, its resonance frequency gets smaller. This effect can be calibrated, and the film thickness can be measured with high accuracy. For lift-off processes, the film thickness should be smaller than the thickness of the resist, for obvious reasons. Typical metallization layers measure thicknesses between 20 nm and a few μm . Another technique could be the so-called "angle evaporation", where the trick is to evaporate successive layers of metals from different angles and use the resist as a shadow mask [19].

In order to obtain an ohmic contact, suitable metal films are evaporated and afterwards alloyed into the semiconductor. Finally, one small technical note should be made here. Since in many cases, mesoscopic transport experiments involve application of strong magnetic fields, it is very important that the ohmic contacts extend across the mesa edge. Otherwise, the contact resistance increases sharply in strong magnetic fields, since the electrons move in cyclotron orbits on the electron gas, and localize within a small area around the contact, see figure 3.11. This problem arises in particular in two-dimensional electron gases and at cyclotron radii below the mean free path [19].

3.1.5 Bonding

Once the sample is patterned and everything looks good, the last step in the fabrication process is to mount the sample into a chip carrier and contact wires to the ohmic contacts and to the gate electrodes. Two versions of

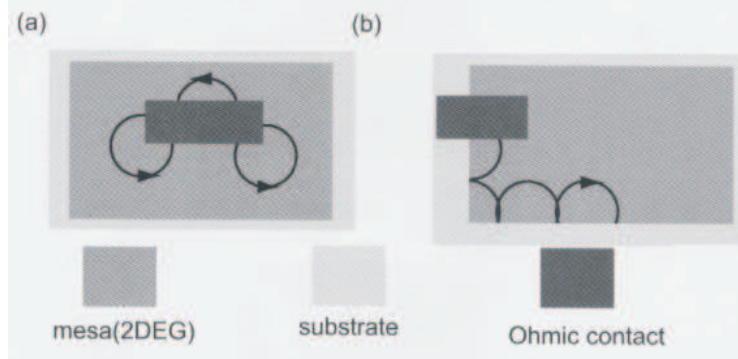


Figure 3.11: In strong magnetic fields, electrons move in cyclotron orbits and thus remain localized close to the Ohmic contact (a), unless the contact crosses the mesa edge (b).

this so-called bonding are widely used: "the ball bonding" and "the wedge bonding". Our structures have been bonded with the second method. The sample is heated to a moderate temperature, 100 °C, in our case, and a connection forms via thermo-compression. The wire is pressed against the bond pad and rubbed across it with an ultrasonic frequency. The friction force is sufficient to locally melt the materials, and an alloy is formed which holds the wire in place. After the second bond, the wire is pulled and breaks at the weakest point, which is right after the position of the wedge. See figure 3.12 [19].

3.2 Local depletion of heterostructures

We saw in the previous paragraph that one possibility to fabricate a semiconductor heterostructure is the growth by molecular-beam epitaxy (MBE). In general, a heterostructure consists of two or more semiconductors with different band gaps, which are combined in a single crystal. With a correct layer and doping sequence one can create e.g. a triangular potential well along the growth direction (z -direction), below the surface. The structure, then contains a two dimensional electron gas at liquid helium temperatures of 4.2 K. The electrons are confined within the potential and can only move in the plane perpendicular to the growth direction.

GaAs and AlGaAs are ideal candidates for the fabrication of heterostructures, because they have almost the same lattice constants but different band gaps: $a_{GaAs} = 5.6533 \text{ \AA}$ and $a_{AlAs} = 5.6611 \text{ \AA}$ [21]. The AlGaAs material system is preferred especially for the band-gap engineering of 2DEGs for

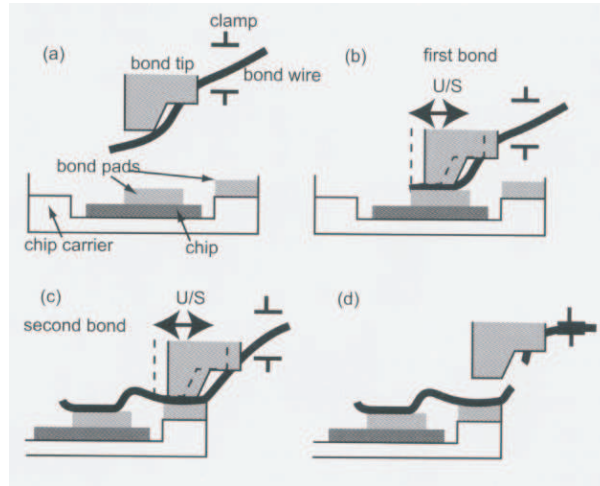


Figure 3.12: Wedge bonding. (a): the bond tip containing the wire is positioned on top of the bond pad on the sample. (b): the wire is wedged onto the bond pad, and the tip is retracted with the wire clamp open. (c): the second bond on the pad integrated in the chip carrier. Here, the tip retracts with the clamp closed, and the wire breaks behind the second wedge.

research applications because the band-gap of the ternary semiconductor $\text{Ga}_{1-x}\text{Al}_x\text{As}$ depends on the Al-content.

In the schematic picture in figure 3.13 the formation of a 2DEG in a $\text{GaAs}/\text{AlGaAs}$ - heterostructures is shown. An intrinsic semiconductor like GaAs with the Fermi energy E_F in the middle of the band gap between the valence band E_V and the conduction band E_C is shown. It is brought into contact with a doped semiconductor with larger band gap like AlGaAs . In equilibrium, E_F has the same value throughout the whole crystal and the band structure aligns itself consistently. At the interface there is a discontinuity in the conduction and the valence band. The conduction band of the intrinsic semiconductor is bent down and the conduction band of the doped material is bent up (lower part of figure 3.13). This leads to the formation of the triangular potential well with quantized energy levels, often named as subbands. By choosing a suitable doping concentration only the lowest subband is occupied.

In general, there are two different approaches for the doping of $\text{GaAs}/\text{AlGaAs}$ - heterostructures. One possibility is the bulk modulation doping where several 10 nm AlGaAs are doped with e.g. Si with a typical concentration of about 10^{18} m^{-3} . In contrast, wafers with a δ -doping contain a layer of Si-donors with a thickness of only a few Å sandwiched between two adjacent AlGaAs layers. The advantage of both heterostructures is the spatial sep-

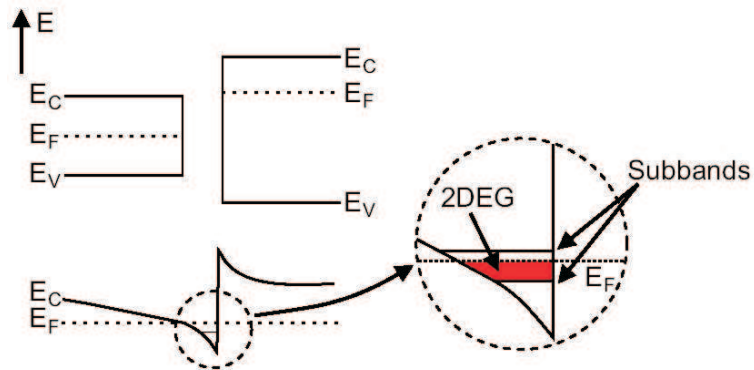


Figure 3.13: Formation of a triangular potential at the interface of two semiconductors with different band gaps.

aration of the electrons from the positively charged donors. This reduces the main scattering process at low temperatures, which limits the mobility of the electrons, namely the remote impurity scattering. Today, with the advancement of the MBE-techniques it is possible to produce 2DEGs with exceptional high electron mobilities of more than $3000 \text{ m}^2\text{V}^{-1}\text{s}^{-1}$. Our wafer with the code: C021212A will be present in chapter 5. In this work a tip of an atomic force microscope (AFM) has been used for the direct manipulation of the electronic structure in a two-dimensional electron gas inside a GaAs/AlGaAs-heterostructure. The actual techniques for the direct nanolithography will be described in chapter 4.

As an example for the depletion process, we will give here a simulation made in an GaAs/AlGaAs - heterostructures, see figure 3.14. This was taken from Keyser's thesis, see ref. [13, 22]. The reason is to show how a groove in the sample surface influences the band structures of our wafer. The band structure is depicted by the black line marked with a square in figure 3.14(b), the edge of the conduction band is shown. Because the minimum of the band structure lies below E_F , a 2DEG is formed inside the triangular potential well. To deplete the 2DEG, we can use a characteristic of the GaAs. At the surface the Fermi energy E_F is pinned near the middle of the band gap of GaAs due to the formation of surface states. By removing a small amount of material from the surface e.g. by using the local anodic oxidation with an AFM tip, this moves the interface closer to the 2DEG and because of the pinning of E_F in the band-gap the triangular potential well is lifted above E_F and the 2DEG is depleted. The band structure after depletion is depicted by the black line marked with a circle in figure 3.14(b) [13, 23].

It is important to notice that the influence is only local underneath the groove. As a consequence, it is possible to write insulating regions directly

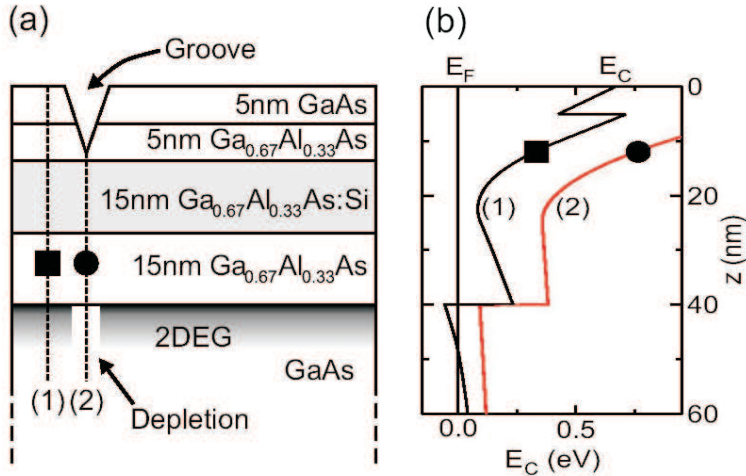


Figure 3.14: (a) Layer sequence of wafer 81016 with a 9 nm deep groove. (b) Simulated band diagram without squares and with circles the groove. This picture was taken from the Keyser thesis [13].

into a 2DEG with a resolution depending only on the width and the depth of the structures created at the surface. Another advantage is the spatial separation between the defect and the 2DEG. This avoids the creation of additional inhomogeneities in the 2DEG, because the "defect" is situated only at the surface.

3.3 Conclusions

This chapter give us an overview about the fabrication techniques used for fabrication of the GaAs/AlGaAs-heterostructures. You can understand already the formation of the 2DEG, at the very low temperatures (about 4 K and smaller), and see how the depletion of this 2DEG, take place. This is the underlying principle for fabricating of mesoscopic devices with an atomic force microscope. In the following chapter you will have a detailed description of the processing of the samples using AFM technique.

Chapter 4

Nanolithography with an AFM

The first scanning probe microscope (SPM) was invented in 1982 by Gerd Binning and Heinrich Rohrer at the IBM laboratory in Zurich [6]. Since that time, a vast family of scanning probe microscopes has been spawned, a few of which are represented in this family tree. All the scanning probe microscopes have a single thing in common. All of them used a tip which touches or not the surface, and measuring different parameters during the moving of the tip on the surface, they could give different information about the surface. The three most common scanning probe techniques are:

Atomic Force Microscopy (AFM) measures the interaction force between the tip and surface. The tip may be dragged across the surface, or may vibrate as it moves. The interaction force will depend on the nature of the sample, the probe tip and the distance between them.

Scanning Tunnelling Microscopy (STM) measures a weak electrical current flowing between tip and sample as they are held a very distance apart.

Scanning Near-Field Optical Microscopy (NSOM) scans a very small light source very close to the sample. Detection of this light energy forms the image. NSOM can provide resolution below that of the conventional light microscope.

Since SPMs achieve atomic resolution, they are highly promising tools for achieving a further, significant size reduction. Meanwhile, SPMs have been used in a wide variety of operational modes in order to modify surfaces. Moving single atoms with an SPM tip, material deposition from the tip on the substrate, has been demonstrated experimentally, for example. Amazing nanodevices can also be fabricated by scratching with AFM. Another widely investigated technique is local oxidation of the substrate. This is also, the case of the AFM. A variety of substrates can be locally oxidized by applying a negative voltage to the tip of an SPM with respect to the grounded substrate. Local oxidation with an atomic force microscope has also been used to pattern

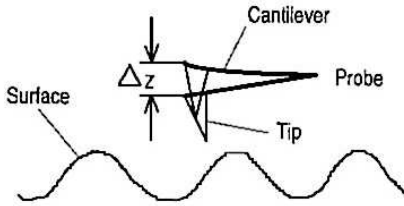


Figure 4.1: Principle of AFM.

the electron gas in GaAs/AlGaAs-heterostructures directly.

Our ring-structures were produced using an atomic force microscope, that is why we will give in this chapter a larger overview about this device.

4.1 Atomic force microscope

The atomic force microscope (AFM) is a powerful tool for producing mesoscopic devices directly in GaAs/AlGaAs-heterostructures. We introduce two different fabrication techniques in which the tip of an AFM is used for manipulation of the surface. We will also give an overview about the working procedure, about the AFM tips and finally about the AFM operating modes.

4.1.1 Working procedure

Atomic force microscope is now becoming a standard instrument in surface science laboratories for obtaining images with atomic resolutions. The technique is based on the principle that when a tip, integrated to the end of a spring cantilever, is brought within the interatomic separations of a surface, potentials will be developed between the atoms of the tip and the atoms of the surface. As the tip travels across the surface, the interatomic potentials will then force the cantilever to bounce up and down with the contours of the surface (figure 4.1). Therefore, by measuring the deflection of the cantilever, the topographic features can be mapped out [24]. The AFM can be operated in two principal modes: with feedback control and without feedback control. If the electronic feedback is switched on, then the positioning piezo which is moving the sample (or tip) up and down can respond to any changes in force which are detected, and later the tip-sample separation to restore the force to a pre-determined value. This mode of operation is known as constant force, and usually enables a fairly faithful topographical image to be obtained (hence the alternative name, height mode). If the feedback electronics are switched off, then the microscope is said to be operating in



Figure 4.2: A Nanoscope Digital Instruments AFM [26].

constant height or deflection mode. This is particularly useful for imaging very flat samples at high resolution. Often it is best to have a small amount of feedback-loop gain, to avoid problems with thermal drift or the possibility of a rough sample damaging the tip and/or cantilever. Strictly, this should then be called error signal mode. The error signal mode may also be displayed whilst feedback is switched on; this image will remove slow variations in topography but highlight the edges of features [25].

A schematic diagram showing some of the essential elements of an atomic force microscope is given in figure 4.3(a). An AFM device is shown in figure 4.2. The atomic forces between a sample and tip are measured using a laser and a detector to monitor the cantilever motion. A negative feedback loop moves the sample up and down via a piezoelectric tube (PZT) so as to maintain the interaction force to a preselected level (Reference Force). A three dimensional image can finally be constructed by recording the cantilever motion in Z direction as a function of the sample's X and Y position. Theoretically for any material which has a certain rigidity, such a instrument is always capable of producing surface images with atomic resolutions as latest development in laser technology has allowed the deflection of the cantilever to be detected down to the Angstrom scale and also, if the tip is suitable enough.

The diagram in figure 4.3(b), illustrates that the light from the laser is reflected onto the split photo-diode. By measuring the difference signal (A-B), changes in the bending of the cantilever can be measured [25]. Since the cantilever obeys Hooke's law for small displacements, the interaction force between the tip and the sample can be found. The movement of the tip or sample is performed by the piezoelectric tube made from piezo-electric

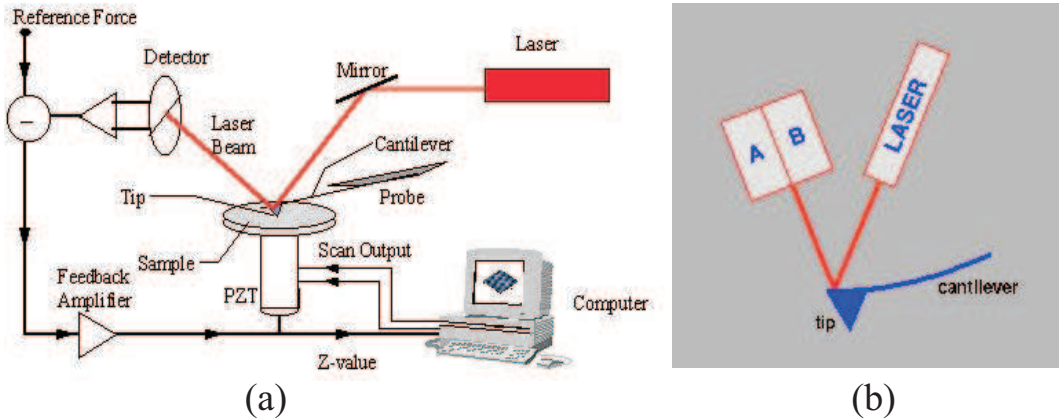


Figure 4.3: (a) Essential elements of the AFM [24]. (b) Working procedure of the laser beam [25].

ceramics. The scanner is capable of sub-angstrom resolution in x-, y- and z-directions. The z-axis is conventionally perpendicular to the sample.

I have to mention, that one of the operating modes of the AFM was described here. This is the so-called "contact mode". This is not the only mode in which the AFM could be working. The AFM can also work in the "tapping mode", where the tip vibrates on the surface and the photo-detector measures the laser-beam oscillations. But the feedback control and the other working procedures are quite similar. These operating modes will be better described in the section 4.1.2.

4.1.2 AFM modes

The way in which image contrast is obtained can be achieved in many ways. The three main classes of interaction are contact mode, tapping mode and non-contact mode.

1. Contact mode

Contact mode is the most common method of operation of the AFM. As the name suggests, the tip and sample remain in close contact as the scanning proceeds. By "contact" we mean in the repulsive regime of the inter-molecular force curve (see figure 4.4) [25]. In contact mode AFM the deflection of the cantilever is sensed and compared in a DC feedback amplifier to some desired value of deflection. If the measured deflection is different from the desired value the feedback amplifier applies a voltage to the piezo

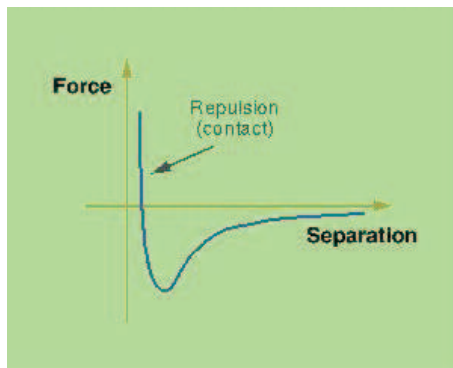


Figure 4.4: Force curve in contact mode.

to raise or lower the sample relative to the cantilever to restore the desired value of deflection. The voltage that the feedback amplifier applies to the piezo is a measure of the height of features on the sample surface. It is displayed as a function of the lateral position of the sample. A few instruments operate in UHV but the majority operate in ambient atmosphere, or in liquids. Problems with contact mode are caused by excessive tracking forces applied by the probe to the sample. The effects can be reduced by minimizing tracking force of the probe to the sample, but there are practical limits to the magnitude of the force that can be controlled by the user during operation in ambient environments. Under ambient conditions, sample surfaces are covered by a layer of adsorbed gases consisting primarily of water vapor and nitrogen which is 10-30 monolayers thick. When the probe touches this contaminant layer, a meniscus forms and the cantilever is pulled by surface tension toward the sample surface. The magnitude of the force depends on the details of the probe geometry, but is typically on the order of 100 nanonewtons. This meniscus force and other attractive forces may be neutralized by operating with the probe and part or all of the sample totally immersed in liquid. There are many advantages to operate an AFM with the sample and cantilever immersed in fluid. These advantages include the elimination of capillary forces, the reduction of Van der Waals' forces and the ability to study technologically or biologically important processes at liquid solid interfaces. However there are also some disadvantages involved in working in liquids. These range from nuisances such as leaks to more fundamental problems such as sample damage on hydrated and vulnerable biological samples. In addition, a large class of samples, including semiconductors and insulators, can trap electrostatic charge (partially dissipated and screened in liquid). This charge can contribute to additional substantial attractive forces between the probe and sample. All of these forces combine

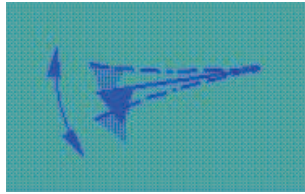


Figure 4.5: The tip in the tapping mode.

to define a minimum normal force that can be controllably applied by the probe to the sample. This normal force creates a substantial frictional force as the probe scans over the sample. In practice, it appears that these frictional forces are far more destructive than the normal force and can damage the sample, dull the cantilever probe and distort the resulting data. Also many samples such as semiconductor wafers can not practically be immersed in liquid [26]. As a design, a contact mode tip has a cantilever much longer than the other types of tips. And this kind of tip may be used in generally for writing oxide lines. Our structures were written using a contact mode tip.

2. Tapping mode

Tapping mode is the next most common mode used in AFM. When operated in air or other gases, the cantilever is oscillated at its resonant frequency (often hundreds of kilohertz) and positioned above the surface so that it only taps the surface for a very small fraction of its oscillation period (see figure 4.5) [25]. This is still contact with the sample in the sense defined earlier, but the very short time over which this contact occurs means that lateral forces are dramatically reduced as the tip scans over the surface. When imaging poorly immobilised or soft sample, tapping mode may be a far better choice than contact mode for imaging. Taping mode operation in fluid has the same advantages as in the air or vacuum. However imagining in a fluid medium tends to damp the cantilever's normal resonant frequency. In this case, the entire fluid cell can be oscillated to drive the cantilever into oscillation. When an appropriate frequency is selected, the amplitude of the cantilever will decrease when the tip begins to tap the sample, similar to Tapping mode operation in air. Alternatively, the very soft cantilevers can be used to get the good results in fluid. The spring constant is typically 0.1 N/m compared to the tapping mode in air where the cantilever may be in the range of 1-100 N/m [26]. Usually the tapping mode tips have the cantilevers much shorter than the others, and they are used by us for the cleaning of the surfaces, because the different spring constant, which lets the tip oscil-

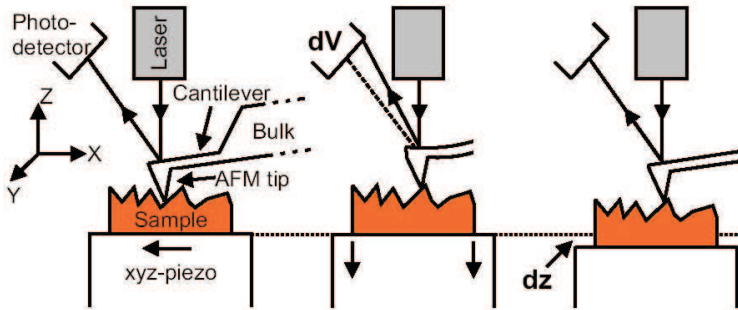


Figure 4.6: Schematic drawing of an AFM consisting of the tip, xyz piezo-resistive crystal, photo detector, and laser. From left to right: When the deflection of the cantilever and thus the contact force changes, the crystal is moved by dz to compensate for the voltage difference dV at the detector.

late much better in tapping mode and also provides a stronger tip-surface interaction in contact mode.

3. Non-contact mode

Non-contact mode operation is another method which may be employed when imaging by AFM. The cantilever must oscillate above the surface of the sample at such a distance that we are no longer in the repulsive regime of the inter-molecular force curve. This is a very difficult mode to operate in ambient conditions with the AFM. The thin layer of water contamination which exists on the surface of the sample will invariably form a small capillary bridge between the tip and the sample and cause the tip to "jump-to-contact". Even under liquids and vacuum, jump-to-contact is extremely likely, and imaging is most probably occurring using tapping mode [25].

4.1.3 AFM tips

A schematic picture of the interaction between tip and sample is shown in figure 4.6. The cantilever is connected to a bulk region needed for the handling of the AFM tips with tweezers. Normally the whole system consisting of tip, cantilever, and bulk, is fabricated of the same material, commonly silicon. In a simple picture, the cantilever is described as a leaf spring with a characteristic spring constant k . I'll describe how a tip works for the contact mode, but for tapping mode is similar. In the contact mode, see section 4.1.2, a contact force F_C is applied between the tip and the surface during the scanning of the surface with a xyz-piezo-resistive crystal. With the spring

constant k of the cantilever the force F_C is easily calculated with Hook's law: $F_C = k\Delta z$, where Δz is the deflection of the cantilever out of equilibrium. The AFM feedback loop measures the contact force between the tip and the surface with the help of the laser that is focused onto the cantilever. The laser beam is reflected at the cantilever top and shines onto a photo detector. The deflection and thus the change of the contact force is monitored by measuring the voltage variation dV at the detector. The height information is obtained by recording the voltages applied to the z-piezo, which are needed to keep the signal of the photo detector constant. Finally, the sample topography is visualized by converting the voltage applied to the z-piezo into height information dz and plotting the data array in a color-coded image [13].

The idea to keep F_C minimal and constant reduces the probability to damage the sample by an AFM tip, which is usually harder than the substrate. When the force constant of the cantilever is exactly known, the AFM can be used to detect ultra-low forces in the range of 10^{-18} N or less. These capabilities enabled to investigate e.g. the Casimir force between an AFM tip and a surface.

For different experiments using the AFM we can use different tips, for example standard silicon tips, or new all-diamond tips. Both types of tips have relatively high force constants of more than 40 N/m.

The diamond tips were grown by hot-filament chemical vapor deposition of polycrystalline diamond onto a prepatterned silicon substrate. A scanning electron microscope (SEM) image of an all-diamond tip is shown in figure 4.7 [13]. Please note, that all components (cantilever, tip, bulk) consist of diamond which is very unusual. Despite the rough surface, the tip radius is still smaller than 50 nm. A magnification of a tip apex is shown in the upper right inset in figure 4.7. Please note the different length scale of the pictures. Despite the rough surface there are some very sharp peaks, which form the active tip used normally for the nanomachining, see section 4.2. A SEM picture of a silicon tip you can see in figure 4.8, before and after being used, to write structures.

It is pretty obvious that for different writing methods, we should use different tips. For example, for nanomachining, see section 4.2, we should use diamond tips, because they are harder, and we can write several good structures without any changing of the tip. In addition, the depth of the lines is also quite good, resulting in a better depletion of the 2DEG. Although the depletion is good, the basic disadvantage is that we cannot write very complex structures with it, see section 4.2. You will see in section 5.3, that our structures have a quite high complexity. If we use a silicon tip for this kind of writing, the tip will be damaged very quickly, after one writing, see

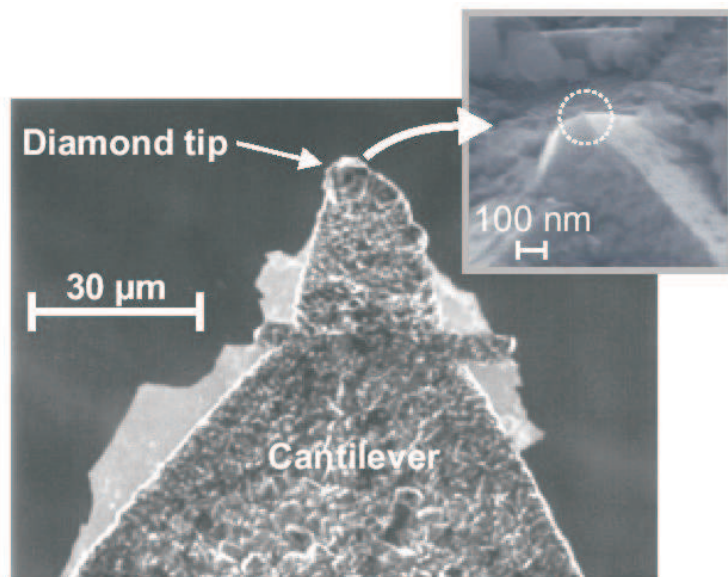


Figure 4.7: Scanning electron microscope image of an all-diamond AFM tip. The inset shows a magnification of the tip that has a radius smaller than a few ten nanometers (indicated by the circle).

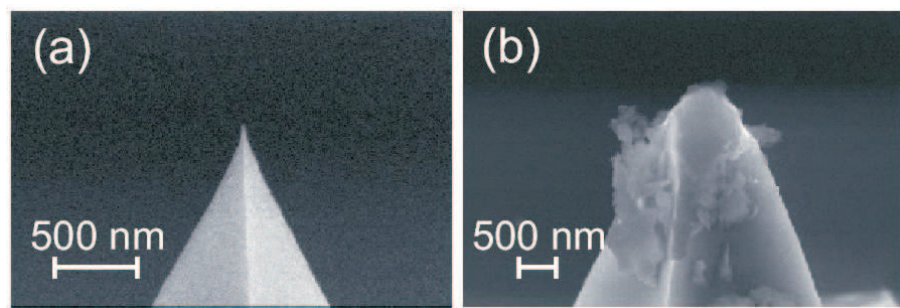


Figure 4.8: Scanning electron microscope image of a silicon AFM tip before (a) and after (b) the nanomachining, the picture is taken from ref. [18]. Please note the different length scales.

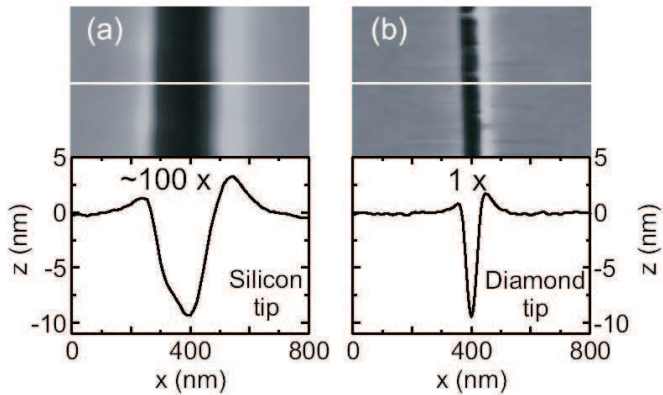


Figure 4.9: Results of the engraving with (a) a silicon tip and (b) a diamond tip. Upper part: AFM micrograph of the grooves. Lower part: depth profile along the white lines. (a) After ~ 100 scans with a silicon tip, (b) after one scan with a diamond tip [13].

figure 4.8(b). But we can use a silicon tip for another kind of writing, called local anodic oxidation, see section 4.3. Here the tip resists longer in time. We can write a few structures without any changes, in the tip radius. A very important advantage is that we can write very complex structures with it, but often the depth of the lines isn't so good. However, with applying a certain back gate voltage, see section 6, we can obtain a good depletion of the 2DEG. Our structures were written using a silicon tip, and you will see in section 4.3, how this is works. For a better comparison between the two types of tips, you can see in figure 4.9 the results of the engraving with a silicon tip and with a diamond tip, respectively [13].

4.2 Controlled nanomachining

We could use the tip of an AFM as nanolithographic tool for engraving grooves into the surface of a GaAs/AlGaAs-heterostructures. This removal of material is the most direct approach to the manipulation of surfaces. This technique is also known as mechanical nanomachining and was demonstrated by several groups on polymer films [27], Langmuir-Blodgett films [28, 29], metals [30] and oxides [31]. The first experiments to modify the electronic structure of a metal film were done by Wendel et al [32].

The nanomachining was also applied on a variety of relatively hard semiconductor surfaces [33, 34, 35, 36]. For this technique it is essential to use a tip consisting of a material with a higher hardness than that of the substrate. Diamond-tips are often used for this kind of operation. We can use

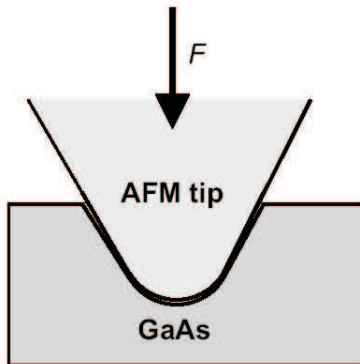


Figure 4.10: Mechanical nanomachining of GaAs with an AFM tip.

also silicon-tips for this, but as you see in section 4.1.3, they couldn't resist too much in time. An AFM tip will protrude into the surface and create a hole when we apply a high contact force of several μN . This will lead to a pressure of several GPa at the tip apex due to the small tip radius, which lies around 10 nm for standard commercial tips. This is depicted schematically in figure 4.10 [13].

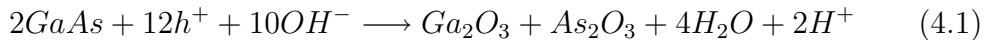
When the AFM tip is scanned over the surface with such high contact forces we can create grooves or lines with any desired geometry, e.g. on the surface of a GaAs/AlGaAs-heterostructure. In the previous chapter, we already mentioned that a groove in a heterostructure is one possibility to deplete the two-dimensional electron gas (2DEG). The big advantage of the AFM is the small radius which allows the width of an engraved line to be below 50 nm [37]. In principle the minimal width of the groove depends only on outer experimental parameters like e.g. the radius of the tip, the angle at the tip apex, the contact force, and the number of times writing the same structure with the tip.

As a conclusion, the nanomachining is a good writing method, which let's us create very deep lines with the breakdown voltage of about $V = \pm 3 \text{ V}$ [13]. But a very big disadvantage is that we cannot create with the nanomachining very complex structures. Due to the fact that this is a scratching method, if we want to write a complex structure we will have some problems when the tip has to make curves, and the surface may be damaged. We need such a method which let's us write even quite complex structures without any risk for the surface. As you will see in section 5.3, our structures are quite complex having a ring shape. Even the lines aren't so deep, we used another method which will be described in section 4.3.

4.3 Local anodic oxidation of heterostructures

One way to create tunnelling barriers in a GaAs/AlGaAs-heterostructures is described already in the preceding part of this chapter. Another possibility to deplete a two-dimensional electron gas is the oxidation of the heterostructure in an electrolytic cell. The oxide grown during the process protrudes into the surface and the band structure underneath is lifted above the Fermi energy E_F in the material very similar to the controlled nanomachining. Despite the difference to the mechanical removal of atoms from the surface this technique uses the same underlying principles as described in Chapter 3. We will show in this section that the local oxidation gives us a direct control over the height of the tunnelling barriers.

In the semiconductor industry the anodic oxidation in macroscopic electrolytic cells is a common technique to oxidize the surface of wafers during the processing of integrated circuits [38]. For the chemical reaction the wafer is mounted into a container in which a noble metal serves as cathode and the wafer material as anode. Water or acids ($pH < 7$) serve usually as the electrolyte. From the chemical analysis of this macroscopic wet-chemical oxidation the reaction equation of GaAs is known [38]:



Here, h^+ stands for positively charged holes in the GaAs. This macroscopic process can be scaled down by using a conducting AFM tip to induce an oxidation of the GaAs locally beneath the tip.

Using a conducting AFM tip with a diameter of a few nanometers as cathode one can reduce the size of the above mentioned electrolytic cell dramatically to a few 100 nm^3 . Under ambient conditions, there is an adsorbed water layer on almost every surface and provides the required electrolyte. This thickness of the water film depends on the relative humidity of the surrounding air. In figure 4.11 a schematic picture of the electrolytic nanocell is shown [13]. We oxidize the surface with the AFM tip in the contact mode: the tip remains in contact with the underlying heterostructure during the whole writing process. With a current source, we apply a constant current to the tip that is negatively biased with respect to the sample. The oxide protrudes out of the surface because of the volume expansion due to the incorporation of oxygen atoms.

The growth of the oxide in our experiments is determined by the oxidation current I_{ox} and the voltage V_{ox} . In our experiments I_{ox} is kept constant throughout the oxidation process. (Because of the low tip-to-sample resistance of a few $\text{M}\Omega$ we can use $|V_{ox}| < 8 \text{ V}$). This reduces the probability of

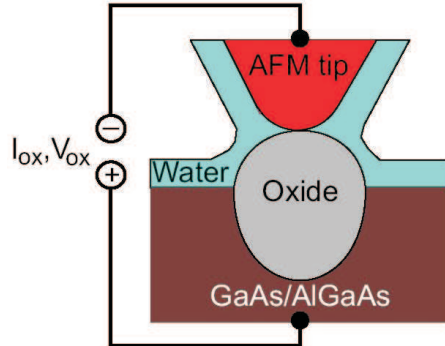


Figure 4.11: Electrolytic nanocell for the local anodic oxidation (LAO).

electrostatic discharging that often destroys the tip during the writing process. The oxidation in the constant current mode extends the lifetime of an AFM tip [39].

Since the first experiments on the local oxidation of the surface of silicon with an AFM, the electrochemical induced nanolithography became an important tool for the fabrication of Si-based semiconductor devices [40, 41, 42, 43]. After the pioneering work of Ishii and Matsumoto [12] several groups began to utilize the so-called local anodic oxidation for the direct patterning of the two-dimensional electron gas (2DEG) in GaAs/AlGaAs-heterostructures [44, 45, 46, 47].

To learn more about the nanooxidation, the characteristics of the writing process on GaAs/AlGaAs, the influence of the oxidation current, relative humidity, and writing speed on the oxide depth and height will be discussed next. In all experiments highly n-doped tips with low spring constants of less than 0.1 N/m fabricated by Nanosensors were used. Controlling the thickness of the water film and thus the efficiency of the oxidation process, was achieved with a continuous flow system built around the AFM. A schematic picture is shown in figure 4.12 [13]. A brass cover with openings (inlet and outlet) for gaseous Nitrogen allows an incessant gas stream during the scanning and oxidation. We supply the Nitrogen from a pressure tank and control the relative humidity by the flow of N_2 that was moistened with distilled water. Additional openings enable the manipulation of the sample from the outside. The relative humidity is measured by a commercial sensor that is mounted inside the brass cover. Using this setup we can vary the relative humidity up to 90 %.

With the local oxidation we can controllably write tunnelling barriers with a specific height into the 2DEG. But there are limitations to the maximum breakdown voltages to a few hundred meV. But as we just said before, this

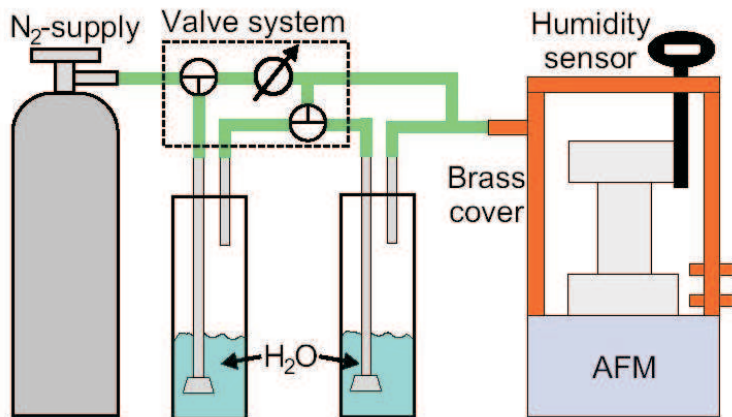


Figure 4.12: Schematic drawing of the continuous flow system for controlling the relative humidity for the local oxidation.

method has a higher accuracy for complex structures, and lines that do not damage the surrounding area. Our structures have been written using the local anodic oxidation, see section 5.3.

4.4 Conclusions

In the first part of this chapter we have described the working procedures of an atomic force microscope, and its working modes. We saw that each of its modes can be used mostly in a special applications such as cleaning or writing. After that we have introduced two techniques for writing mesoscopic devices. The first technique is the controlled nanomachining for the depletion of heterostructures. This is a technique of mechanical removing of the surface. We saw that we can use a diamond or a silicon tip, for this, and it is normal than the diamond tip is much better for this operation than the silicon tip. The second technique is the local anodic oxidation with an AFM. With this alternative approach to the depletion of heterostructures we have a technique that gives us a direct control over the height of the tunnelling barriers in a two-dimensional electron gas. The oxidation current determines the barrier high.

Chapter 5

Experimental procedures

We will describe in this chapter all our experimental procedures. As we already mentioned, we need for all our measurements very low temperatures. These temperatures can be obtained using special devices called cryostats (refrigerators). To obtain very low temperatures we use Helium and Nitrogen. We start this chapter with a short description of our used dilution refrigerator, looking at some properties of the liquid helium. After that we will present our sample and the fabrication steps. We will describe finally, the measurement setup used in our experiments.

5.1 Elements of cryogenics

Helium is the only element that remains liquid when cooled to the lowest possible temperatures (well below 1 mK) under atmospheric pressure. It is therefore the prime candidate as a refrigeration medium for temperatures below the condensation temperature of nitrogen (77 K). The vast majority of mesoscopic transport experiments are performed in this temperature range. The latent heat that has to be paid when liquid helium is evaporated is the cooling power made use of in helium cryogenics. Continuous evaporation of liquid is possible by pumping off the vapor pressure. Therefore, we will look at the properties of liquid helium (LHe), as well as cryostats, the devices used to establish low temperatures.

5.1.1 Properties of liquid helium

The physics of LHe is extremely interesting and rich, and experimentalists working on transport in nanostructures, will almost inevitably get in contact with its unusual properties.

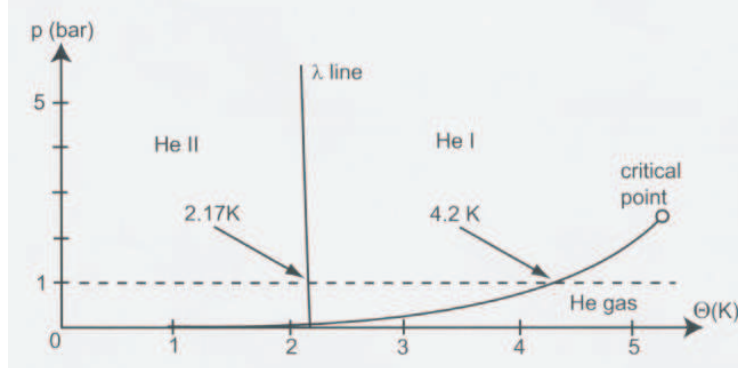


Figure 5.1: Phase diagram of the ${}^4\text{He}$ [19].

Helium comes in two isotopes, the boson ${}^4\text{He}$ and the fermion ${}^3\text{He}$. The mono-isotopic liquids have therefore very few properties in common. As a liquid is cooled, kinetic energy is taken away from the atoms. At the crystallization temperature, the attractive interatomic van der Waals forces start to dominate in any liquid other than LHe, and the crystallization sets in. He is the only element for which the van der Waals force is smaller than the kinetic energy of the atoms due to zero-point fluctuations. The van der Waals forces in He are particularly weak since the atoms have no dipole moment. On the other hand, the zero-point fluctuation energy is particularly large, due to the small atomic mass. Only by applying a pressure above ≈ 30 bars, the atoms are pressed sufficiently close together such that crystallization sets in [19]. We now look at some properties of the pure isotopic liquids, before we turn to the interesting issue of ${}^3\text{He}/{}^4\text{He}$ mixtures.

Properties of ${}^4\text{He}$

Figure 5.1 shows the phase diagram of ${}^4\text{He}$. Under atmospheric pressure, it liquifies at $\Theta = 4.2$ K. The density of the liquid $\rho(\text{L}{}^4\text{He}) = 125 \text{ kg/m}^3$. The vapor pressure drops approximately exponentially as LHe gets colder, and reaches 1 mbar at $\Theta = 1.2$ K. As we cool the liquid, we cross the λ -line at some temperature, which for atmospheric pressure happens at $\Theta_\lambda = 2.17$ K, also known as the λ -point. The λ -point got its name from the specific heat as a function of Θ around this transition, a function that looks like this omnipresent Greek letter. For $\Theta > 2.17$ K, ${}^4\text{He}$ behaves just like any ordinary liquid. As we lower Θ and cross the λ -point, ${}^4\text{He}$ undergoes a phase transition and develops highly remarkable properties. L ${}^4\text{He}$ in this phase is often referred to as HeII. In fact, the phase transition at the λ -point can be modelled as a Bose-Einstein condensation, i.e., the condensation of a boson

gas. Within such a model, the ${}^4\text{He}$ above the λ -point is described as a gas, which is not a bad approximation, considering the weak interactions. At $\Theta = 0$, on the other hand, all atoms of HeII are in the ground state. At higher temperatures, the energy levels in a Bose-Einstein condensate (BEC) are occupied according to the Bose-Einstein distribution function [19]:

$$f_{BE}(E, \Theta) = \frac{1}{e^{(E-\mu)/k_B\Theta} - 1} \quad (5.1)$$

A pure BEC, however, cannot explain the observed behavior of HeII. Rather, a two-liquid model was proposed, which treats HeII as a mixture of a normal fluid and a superfluid, which interpenetrate on a microscopic length scale, similar to the electronic state in a type II superconductor. The normal fluid behaves just like ${}^4\text{He}$ above the λ -point. In particular, it has a non-vanishing entropy and viscosity. The superfluid, on the other hand, has zero entropy and viscosity, which means, for example, that there is no flow resistivity. Furthermore the thermal conductivity of the superfluid is infinitely large. This two-component mixture has some unique properties we should know, in order to appreciate its behavior in cryogenic equipment.

1. Absence of bubbling.

If we heat a conventional liquid, it starts bubbling, since the liquid evaporates at some random spot, and the gas bubble rises to the surface. In HeII, the thermal conductivity is very large, and evaporation takes place at the surface only. Hence, HeII is perfectly quiet, even if it boils off. In a simple picture, we can understand the extremely high thermal conductivity as follows. Imagine we connect heat reservoirs to both ends of a tube filled with HeII. At the end with higher temperature, superfluid is transformed into normal fluid, with a final ratio in accordance with figure 5.2. The heat is transferred to the low-temperature end by normal fluid conversion. Here, the normal fluid is re-transformed into superfluid. Since the superfluid carries no heat (its entropy is zero), all the heat is thereby absorbed by the heat sink. The heat transfer is therefore very efficient. The heat conductivity is further increased by the extremely low viscosity of HeII, which means there is vanishingly small friction during the convection process [19].

2. HeII osmosis.

Consider two chambers filled with HeII, connected to each other by a superleak, i.e., a connection only permeable for superfluid helium, see figure 5.3. Such connections can be made by extremely fine capillaries, or by

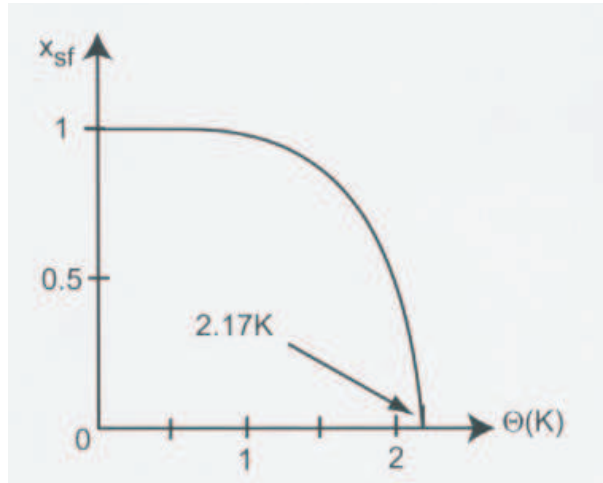


Figure 5.2: Superfluid fraction x_{sf} of HeII as a function of temperature.

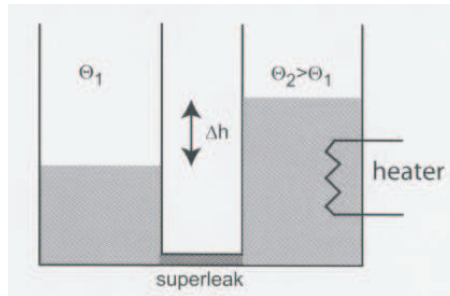


Figure 5.3: Sketch of a HeII osmotic cell.

tubes stuffed with powder. This setup immediately reminds us of an osmotic pressure cell, with the semipermeable membrane being the superleak, the solvent being the superfluid, and the normal fluid component starring as the solute. Recall that in osmosis the solute can be thought of a gas, and that the osmotic pressure evolves due to the tendency of the solvent to equalize the concentration in both chambers. As we heat HeII in one chamber, the fraction of normal fluid increases, and superfluid will enter this chamber, in order to dilute it. Consequently, a pressure difference is built up. In equilibrium, the hydrostatic pressure will compensate the osmotic pressure, and the surface positions in the two chambers will differ by Δh [19].

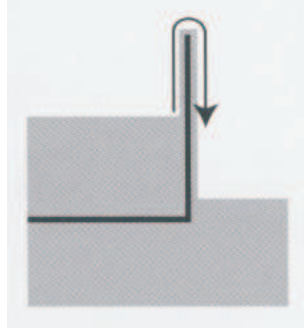


Figure 5.4: Superfluid film creeping across a wall.

3. Superfluid film creeping.

HeII tends to creep over any wall of reasonable height, as long as its temperature stays below the λ -point. Therefore, containers filled with HeII to different heights will equilibrate their surface levels, see figure 5.4. This effect has its origin in the extreme adhesion of HeII to surfaces. Within the framework of liquid-solid interfaces, this is known as "complete wetting". Since the shape of the liquid surface is determined by the condition that the tangential forces vanishes, this effect occurs for $-\sigma_{ls} > \sigma_{gl}$, where $\sigma_{ls}(\sigma_{gl})$ denote the liquid-solid (gas-liquid) interface tension [19].

Properties of ^3He

In figure 5.5, the phase diagram of ^3He is sketched. For our purposes, the additional phases occurring at extremely low temperatures below 2 mK are irrelevant. L^3He has a density of $\rho_{^3\text{He}} = 59 \text{ kg/m}^3$. Under atmospheric pressure, it liquifies at $\Theta = 3.19 \text{ K}$. This boiling point is about 1 K below that one of ^4He , which can be easily understood, since its mass is smaller, and thus the atoms have a larger average velocity at the same temperature. Consequently, the vapor pressure is also higher at identical temperatures. It drops to 10^{-3} mbars at about $\Theta = 270 \text{ mK}$. ^3He atoms are fermions, and the liquid can be approximated by a Fermi gas, with many analogies to electron gases.

Within the Fermi liquid picture, we can imagine that each ^3He is surrounded by a screening cloud, which results in quasiparticles with an effective mass given by the interactions. At atmospheric pressure, $m^*(^3\text{He}) \approx 3m(^3\text{He})$. For practical cryogenic purposes, ^3He behaves as an ordinary liquid.

A further important point concerning ^3He is its near-to-complete natural

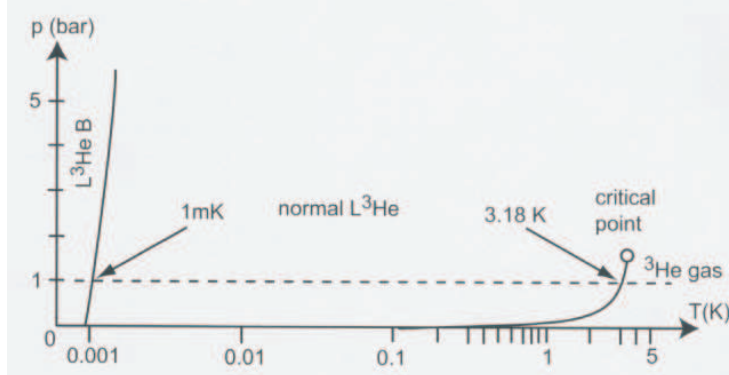


Figure 5.5: Phase diagram of ^3He [19].

absence on earth. It can be generated by nuclear reactions, and is consequently extremely expensive. Therefore all ^3He cryostats keep it in a closed cycle [19].

Properties of $^3\text{He}/^4\text{He}$

Let us first look at the phase diagram of this mixture, figure 5.6. For $\Theta > 860$ mK, nothing spectacular happens. The main effect of the ^3He is to reduce the λ -point of the homogeneous mixture. Below the λ -line, ^3He dissolved in HeII can be just thought of an additional fraction of the normal fluid component. For temperatures below 860 mK, a remarkable phase separation into a ^3He -poor phase (called the dilute phase-D) and a ^3He -rich phase (called the concentrated phase-C) takes place. At these temperatures, the pure HeII is almost completely superfluid, and the dissolved ^3He forms a normal fluid component.

A qualitative understanding of the phase separation can be obtained by recalling that ^3He is a fermi liquid, while ^4He in this regime is a Bose-Einstein condensate. The ^3He dissolved in ^4He can be thought of a dilute Fermi gas with an effective mass given by the interaction between the ^3He atoms and the surrounding ^4He , which is $m^*(^3\text{He in } ^4\text{He}) \approx 2.4m(^3\text{He})$. Since superfluid ^4He has zero viscosity, the ^3He atoms can move around without friction, once the ^3He - ^4He interaction is included in the effective mass. L^3He can be regarded as a Fermi gas as well. We just have to establish the conditions for which the chemical potentials of the C phase and the D phase are identical. Here, the superfluid ^4He plays no role, as all these atoms are in the ground state. Here, the common energy level is again the vacuum level, i.e., the energy of a ^3He atom at rest in the vacuum. The chemical potential $\mu(3)$ of the C phase is somewhat higher than that on $\mu_0(34)$ of a single ^3He in

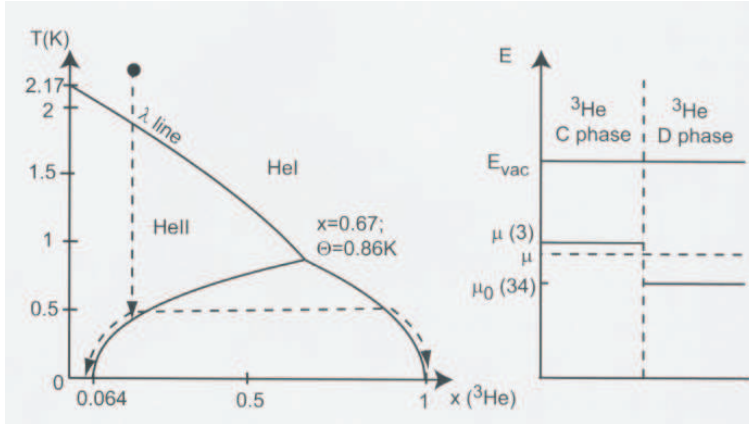


Figure 5.6: Left: phase diagram of the ${}^3\text{He}/{}^4\text{He}$ mixture vs. ${}^3\text{He}$ concentration x and temperature Θ . The tricritical point is at $x=0.67$ and $\Theta = 860$ mK. At lower temperatures, the mixture segregates into a ${}^3\text{He}$ -concentrated phase (the C-phase) and a ${}^3\text{He}$ dilute (D) phase. Right: sketch of the chemical potential of the two phases at $\Theta = 0$ [19].

${}^4\text{He}$, which can be understood by the fact that the (attractive) van der Waals forces are slightly larger in ${}^4\text{He}$, since the average separation of the atoms is smaller. Hence, ${}^3\text{He}$ atoms will go into ${}^4\text{He}$ until the chemical potentials have aligned. This is the reason why even at $\Theta = 0$, the D phase contains still 6.4 % of ${}^3\text{He}$ atoms. Note that it is energetically unfavorable for ${}^4\text{He}$ atoms to reside in the C phase [19].

5.1.2 ${}^3\text{He}/{}^4\text{He}$ dilution refrigerators

First of all we have to mention that the Helium cryostats can be classified according to the kind of helium mixture for which they are designed. Occasionally, liquid nitrogen cryostats are used as well, for temperatures between 77 K and larger. We used for our measurements a ${}^3\text{He}/{}^4\text{He}$ dilution refrigerator, that is why we will talk only about this type.

The ${}^3\text{He}/{}^4\text{He}$ dilution refrigerator uses the special properties of ${}^3\text{He}/{}^4\text{He}$ mixture in a clever way, and makes possible temperatures as low as about 3 mK and even below, but our cryostat system reaches only 20 mK. Since the D-phase of the mixture is approximately a dilute Fermi gas, it can be thought of the ${}^3\text{He}$ vapor of the C phase, with a significant vapor pressure even at $\Theta = 0$. Since the C phase has a smaller density, the "liquid will float on top of the gas", though. Pumping the ${}^3\text{He}$ atoms out of the D phase will surely cause ${}^3\text{He}$ from the C phase to evaporate, which pulls the corresponding

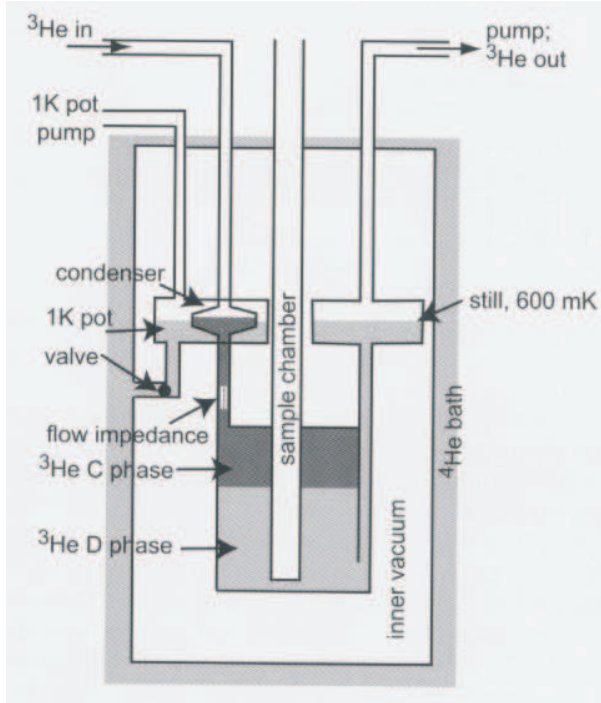


Figure 5.7: Essential components of a $^3\text{He}/^4\text{He}$ dilution refrigerator.

effective latent heat out of the mixture. This is the cooling mechanism in such a dilution refrigerator as sketched in figure 5.7 [19]. The mixture rests in the mixing chamber. The D phase is connected through a tube with the still, a pot that gets heated to about 600 mK. At this temperature, the vapor pressure of ^3He is significant, while that one of ^4He is negligible. The so-called still therefore effectively distills ^3He from the D phase. The missing ^3He in the D phase gets delivered by "evaporation" across the C-D phase boundary, and the mixture in the mixing chamber gets colder. The evaporated ^3He is recondensed into the mixing chamber by a pot filled with ^4He , that gets pumped below the condensation temperature of ^3He . This is the "1K pot". The freshly condensed ^3He has, of course, still a much higher temperature than the mixture. The heat flow in the mixing chamber is therefore optimized by a flow impedance in the condenser line. In addition, the outgoing gas at the still temperature is used to further precool the condensed ^3He via heat exchangers. Our mesoscopic transport experiments below 270 mK have been carried out by immersing it directly in the mixing chamber.

A real $^3\text{He}/^4\text{He}$ dilution refrigerator is a quite complex system. Its walls are made with special materials and they have few layers. First, there is a vacuum separation between the inside and the outside of the cryostat.

A nitrogen shield follows after the vacuum, so the helium is precooled. In this way a very good separation with the atmospheric temperature results. The cryostat has also a cleaning system called "cold-trap" which contains Nitrogen also. The cold trap is used for collecting the dirt particles from the cryostat. It is obvious that ^4He and N_2 are used in time by the system, and they have to be refilled periodically. Of course, the helium mixture have to be pumped all the time, as well as the ^4He . The evaporated ^4He is passed through a recovery line, and recollected, but the helium mixture is quite expensive so it is a closed circuit for this. If the cryostat system is stopped, the helium mixture is collected into a helium dump.

Due to the fact that many experiments should be made in strong magnetic fields, many cryostats are equipped with a superconducting magnet, which is cooled below the critical temperature by the LHe. Magnets are usually made from special alloys and they have a critical temperature. Our superconducting magnet is able to generate magnetic fields of 18 T. If we give more current than that, the magnet loses the superconducting properties and it is able to transfer a lot of heat to the helium main bath of the cryostat. This results in a big loss of helium and is quite dangerous for the system due to the big pressures involved in it. We can pump helium near the magnet, and so cool the magnet below its critical temperature for higher fields. This operation is called λ -stage (because we then cool beneath Θ_λ , see section 5.1.1) and makes it possible to reach in our case up to 20 T.

5.2 Experimental setup

Measuring the resistance and conductance of a sample requires the application of currents and/or voltages, as well as the detection of voltage drops and/or currents, respectively. Conceptually, these measurements are very simple. The greatest efforts in practice are usually related to the reduction of the electronic noise level. This is done by avoiding ground loops, filtering, and choosing the right cables, among other important issues. As in the previous section, we are not that much interested in these technical details. Our goal here is to present in brief some basic setups, just enough for the reader to know what type of setup has been used in the experiments to be discussed. In the previous section, we have seen that our cryostat set some limitations to the temperature range. Likewise, the measurement setup limits the physical quantities, as well as their ranges, that can be measured. We begin by showing how the samples are actually mounted in the low-temperatures environment, before we discuss the most important electronic measurements setup.

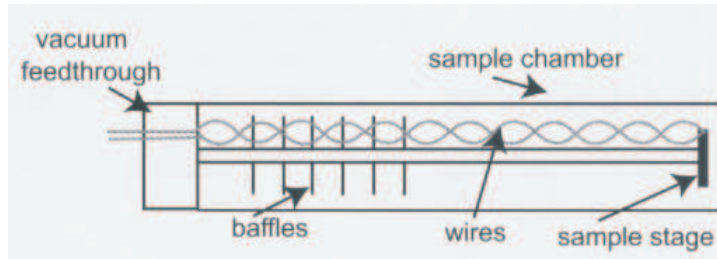


Figure 5.8: Sketch of a sample holder used to stick a specimen in the sample space of a cryostat.

5.2.1 Cryogenic setup

As you can see in figure 5.10, our samples are mounted in a $^3\text{He}/^4\text{He}$ dilution refrigerator, with help of a tube called probe, like that presented in the next section (see 5.8). The cryostat system was already described in section 5.1.2. For the magnetic field a special current source is necessary. The cryostat itself is a quite complex system and it has a lot of sensors for reading different parameters, as well as many valves and switches for opening, closing or changing the certain compartments properties. We will not talk to much about this stuff. This has been described in special books, see reference [19]. We just have to specify that all these valves are build into an electronic intelligent gas handling box which together with a measurements unit responsible for the reading of temperatures and He/N levels, are controlled by a computer through an ISO-bus connection (see figure 5.10). Our $^3\text{He}/^4\text{He}$ dilution refrigerator is build in the underground, for a few reasons. For the first, it is more easy to operate due to the fact that our sample tube is very high and doesn't fit into our laboratory. The second reason could be because the magnetic field is kept further away from the measurement setup and from the personnel.

5.2.2 Sample probe

The probe contains the sample in an appropriate way, and is mounted in the sample space of the cryostat. Its basic components are sketched in figure 5.8. The sample is mounted in some kind of carrier, which is placed in the center of the magnetic field. Cables are brought into the sample space via a vacuum feedthrough at the top end. Typically, the wires run in loops, which reduces the currents induced by the magnetic field due to vibrations, since the magnetic flux through adjacent loops points in opposite directions [19]. Furthermore, the sample holder contains baffles, i.e., polished metal plates

which reflect the thermal radiation from the top. On the other hand, we want to cool the sample very well. The wires could transfer some heat from the outside, and warm the sample. For this reason, in the very last part of the tube, the wires are, due to the loops, long enough (in the main bath of the cryostat) to be cooled together with the sample. And also in our case, a part of the sample carrier is made from Cu which is good conductor of heat and acts as a heat sink.

5.2.3 Electronic setup

For many experiments, measuring in a low temperature environment only make sense when the electric signals are kept sufficiently small. Suppose, for example, we plan to investigate the transmission properties of a tunnel barrier. The low temperature reduces the thermal smearing of the Fermi function, which corresponds to an energy scale of $\delta E = 3.52k_B\Theta \approx 300 \mu\text{eV/K}$. Therefore, the voltage drop across the barrier at, e.g., $\Theta = 1 \text{ K}$, should be small compared to $300 \mu\text{V}$. For larger voltage drops, the temperature does no longer determine the energy resolution [19]. Also, it has to be mentioned here that we used very small currents, in order to not heat the sample.

Measurements can be performed in AC or DC. AC measurements have the advantage that a lock-in amplifier can be used, a device that selectively detects signals with the source frequency, within a narrow band width. In addition, phase-sensitive measurements are possible, such that, e.g., capacitance measurements can be performed by measuring the voltage drop with a phase shift of $\pi/2$ with respect to the source signal. Although the frequency selection greatly reduces the noise, it is not always best to use an AC signal. For example, imagine the sample has a very large resistance, such that the capacitances, which are always present in the leads, cause significant phase shifts. This makes it hard to determine the resistive part of the impedance. Also, theoretical results are often obtained for DC transport [19].

Furthermore, it has to be clearly distinguished between the resistance and the resistivity (conductance and conductivity, respectively). The plain result of, say, applying a current I and measuring the voltage drop ΔV is the resistance $R = \Delta V/I$. If the sample is macroscopic, we can assume that the voltage drops homogeneously in between the voltage probes, and we can translate the resistance into a resistivity, an intrinsic property of the sample, by taking the sample geometry into account. This is no longer true in mesoscopic samples. Here, the measurements does not average over a large volume of randomly distributed scatterers, and the sample simply does not have a resistivity [19].

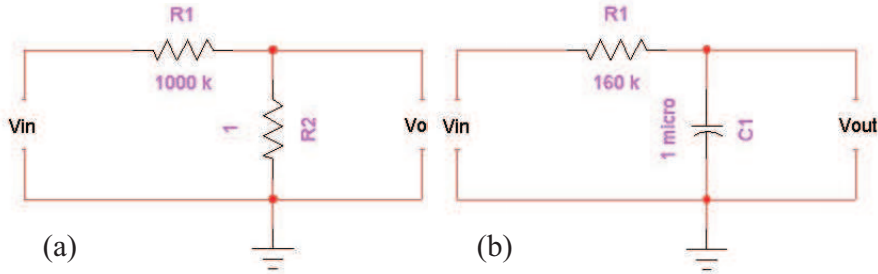


Figure 5.9: (a) A voltage divider, 1:1000 ; (b) A low-pass filters with the cut frequency of 1 Hz.

1. Voltage dividers

High quality commercial voltage sources typically provide voltages in the regime of Volts, with an accuracy of, say 10^{-6} . Hence, some conversion to smaller voltages, or to a small current, is often necessary. This is done by a voltage divider, or a voltage-to-current conversion, respectively. For example, in our experiments the source contact has a voltage divider like in figure 5.9(a). We see later why something like this is necessary. This voltage divider simply consists of two resistors in series connected to the output voltage V_S of the commercial voltage source. The potential in between the two resistors is applied to the sample with respect to ground. This voltage is given by:

$$V_{out} = V_{in} \frac{R_2}{R_1 + R_2} = V_{in} \cdot \frac{1}{1 + 1000} \simeq \frac{V_i}{1000} \quad (5.2)$$

So, we can notice that the output voltage is a thousand times smaller than the input voltage, that is why we can call this a 1 : 1000 voltage divider.

1. Low-pass filters

On the other hand for our experiments, we need filters for noise reduction and for preventing peaks and to avoid sharp steps when we charge e.g. gate voltages. We chose to use some low-pass filters with the cut frequency of 1 Hz. Such a filter is given in figure 5.9(b). We can calculate the cut-frequency from the relation below:

$$f_t = \frac{1}{2\pi RC} = \frac{1}{2\pi \cdot 160\text{k}\Omega \cdot 1\mu\text{F}} \simeq 1\text{Hz} \quad (5.3)$$

1. Measurement setup

In the following, we will discuss about our electronic setup. In the figure 5.10, you can see the complete block diagram used in our experiments. As we just said, in order to reduce the noise as much as possible, we used different techniques. The measurements can be performed (as I mention before) with AC and DC signals. We used for this, the lock-in technique. That means, we used a lock-in amplifier, which produced an AC signal in a certain frequency. We choose first, to use 13 Hz, for the reason that 13 is a prime number so it is not a harmonic of any artificial frequency. Due to this fact, the signal should be less noisy in this region. During the measurements we used different frequencies e.g. 89 Hz, 37 Hz, in order to eliminate the noise in a certain kind of measurement. The AC signal given by the lock-in amplifier can be added with a DC signal given by a Digital-Analog converter (DAC). The digital-analog converter gives DC signals and is being controlled by a computer. The resultant signal is passed through a 1:1000 voltage divider (see figure 5.9(a)) and after that it is applied to the source contact of our structure. Also, to the output of the adder, we put an electronic multimeter, in order to measure the exact value of the applied voltage. The DAC has four ports, so it can apply DC signals to four contacts. You can notice from the figure 5.10, that we used this lock-in technique just for the source contact, as a measurement technique, because, here, we are interested to read the pure signal and the noise should be as less as possible. The other contacts, for the gates, are performed with DC signals given directly by the DAC, but each of them, through a 1 Hz filter (see figure 5.9(b)). All our measurements consisted in measuring the conductance in the ring as a function of different parameters. The applied signal to the source contact has to be measured to the drain contact. In fact we have to measure the current through the source and drain contacts. For this we used a current amplifier that generates at its output a voltage proportional with the current. The DC part of current is measured also with an electronic multimeter. For the back-gate (BG) of our structure we used a voltage source, in order to apply voltages up to 200 V. For this reason we used a $1\text{ G}\Omega$ resistor, for limiting the current which passes through the BG in the case of break-through. We also have to mention, that all the electronic devices are connected to a GPIB bus, so they can be totally controlled by a computer.

You see in figure 5.10 a very simple block diagram of our experimental setup. Generally speaking it is much more complex than that. But, for simplicity we have represented, the most important blocks. For example as you see we used 2 different computers, for the controlling of our measurement setup for the reason that the one which controls the cryostat, has to run

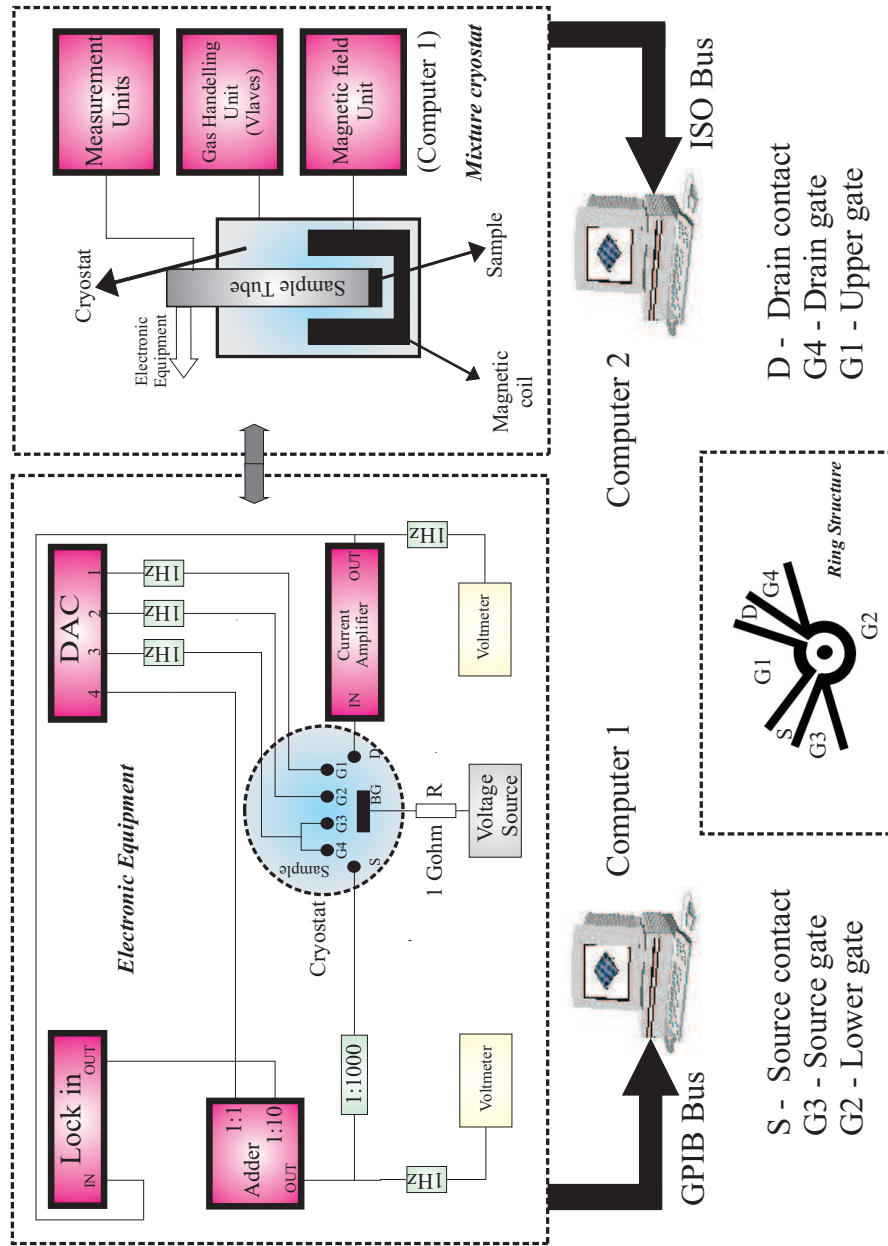


Figure 5.10: Bloc diagram of our experimental setup.

very stable. We also had to make an optical separation between the GPIB-computer and the electronic equipment, in order to reduce the noise produced by the computer. It is also very important that the person who operates the electronic devices to be grounded, for the reason that the sample could be shocked by some electrical discharges of the human body. So you can see now, that the principle of our measurement setup is very simple, but in reality there is a complex measurement chain in order to make sensitive measurements and to reduce the noise as much as possible.

5.3 Sample preparation

This section will describe the most important steps of our sample preparation. Some steps are not physically explained here, anymore, because they were explained in section 3.1. They will just be sketched in the following.

First, we have to mention that the layers have been grown by the *Walter–Schottky Institute*, using the Molecular Beam Epitaxy technique. The layer succession you can see in figure 5.11. You can see already that the 2DEG is formed 37 nm below the surface. Also, our wafer has an electron density: $n_e = 4.59 \cdot 10^{11} \text{ cm}^{-2}$ and an electron mobility of $\mu_e = 6.43 \cdot 10^5 \text{ cm}^2/\text{Vs}$ in the dark and in the light: $n_e = 6.12 \cdot 10^{11} \text{ cm}^{-2}$ and $\mu_e = 9.32 \cdot 10^5 \text{ cm}^2/\text{Vs}$. These values are given for a temperature $T = 4.2 \text{ K}$. So we received the material, already grown with code C021212A. Due to the fact that our chip carriers are of $5 \times 5 \text{ mm}^2$, we had to cut first our wafer with a special device which uses a diamond tip. This device permitted us a very fine positioning of our material, so we were able to cut our wafer with very good precision.

The first tenth steps, we present in the following have been performed in the clean room (see section 3.1). The next steps belongs to the AFM technique (see section 4) and to the measurement setup (see section 5.2.3).

1. Cleaning the wafer

The first step in the cleaning room was to clean our wafer very good, with acetone, in an ultrasonic bath. Acetone is necessary for dissolving any dirt which is removed by ultrasonic sounds. After a time of about 5 min., we washed our wafer, first with methanol, which removed the acetone very good and so the dirt solved in there, and after that with isopropanol, which evaporates very quickly and leaves the surface of the wafer dry and clean.

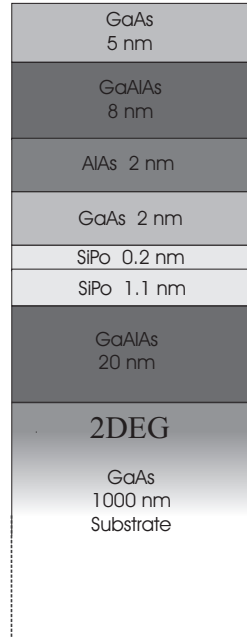


Figure 5.11: The layer succession of the wafer C021212A.

2. Resist deposition

After this preclean session, we've put our wafer in a centrifuge device, for cleaning once again. While the centrifuge was rotating we applied acetone, methanol and isopropanol, respectively. Because of the fast rotating of the centrifuge, the dust particles are dissolved and removed, due to the centrifugal force. After this second clean, we drop on some chemical photoresist type ARU 4040, which is equally distributed on the surface, because of the constant rotation of the centrifuge. After that the photoresist was heated to 92 °C for about 5 min. This operation is necessary for the photoresist to be fixed on the surface very good. I have to mention that this is a positive photoresist similar to that presented in section 3.1.3

3. Optical lithography

After the photoresist was deposited on our surface, an optical lithography process follows. The surface is covered with a mask which is very good positioned in respect with the surface. The mask and the surface are illuminated with ultraviolet light for 10 s (see section 3.1.3).

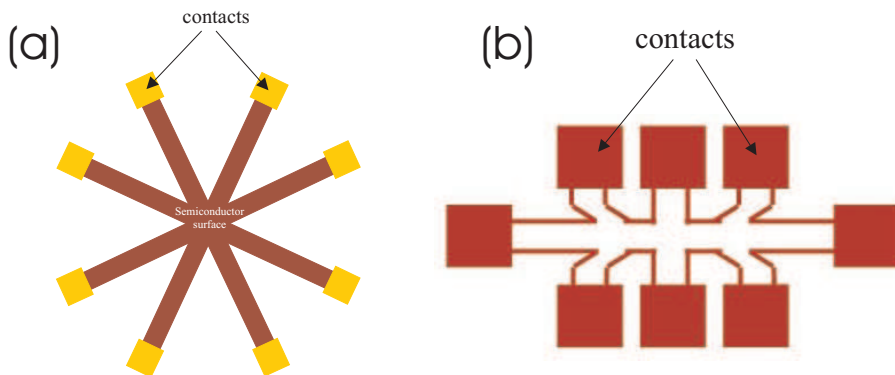


Figure 5.12: (a) A star structure, (b) A hall-bar structure.

4. Developing

After the illumination process, the photoresist parts which were illuminated can be removed by a developing process. This process is similar to developing photographic films for pictures. Do not forgot that we still have the other parts of the photoresist which were protected by the mask during the illumination.

5. Etching

The parts remained without photoresist, can be now, etched using some acids. This is called wet chemical etching and was described in the section 3.1.3. We kept the sample for a few seconds in a $\text{H}_2\text{O} : \text{H}_2\text{O}_2 : \text{H}_3\text{PO}_4$ acid solution with a concentration of 40:5:3. In the final we wash our sample with H_2O . This process permits us to create the star-like mesa and the hall-bar mesa. In figure 5.12, you can see these 2 different shapes for our mesa. Our wafer has eight stars and one hall-bar structure. We see in the next chapter why it is important to have at least one hall-bar structure on our wafer.

6. Removing the other photoresist

After the shapes are created on our surface, we have to remove the remaining resist parts from our surface. For this we used, like before, acetone, in an ultrasonic bath, and after that methanol and isopropanol. This is a step similar like 1.

7. Defining contacts

After this first important part in our fabrication steps, it follows another part concerning the defining of our contacts. This is made with a few steps that are similar with 5 and 6. We deposited again an uniform photoresist on our surface, and we used a different mask for our contacts. An optical lithography process follows again. But at this time, we transform our resist in a negative one, see section 3.1.3. For this we have heated our wafer with the deposited photoresist in a special session. After the heating, we illuminated the surface again for a short time. By this steps we transformed the positive resist into a negative one. After a developing process, similar with 4, the photoresist from the contact places will be removed. Most parts of our surface will be still covered by the photoresist.

8. Burning clean

In order to remove better the photoresist from the contact places, we have used a special technique which is similar with the one presented in section 3.1.3. We used an oxygen plasma to burn all the photoresist particles that remains on the surface where the contacts should be formed. This is necessary because we want to have a very clean surface before the metallization process.

9. Metallization

Now, we are able to deposit the metal for our contacts, in the empty spaces which remain after the developing of the photoresist. We have used the vapor metal deposition in a vacuum chamber, see section 3.1.4. This permits us to have a good control to the deposited layers. In order to create really good contacts, we had to deposite a few layers of metals. For the first we grow 2 layers of Ge (40 nm) and Au (60 nm). Germanium together with gold, will create an alloy which makes a very good contact with the semiconductor surface. These two layers are covered by a small layer of Ni (27 nm), and the very last layer is a thick layer of gold (150 nm), for a better contact with the bond-wires. Due to the fact that the Ge-Au alloy has the exact concentration of Ge and Au, respectively, Ni is necessary to separate this alloy from the rest of the gold. After the metallization process was finished, we had to expose the sample again to a special heating process. But this time, we used an annealing oven, controlled by a computer. The sample was exposed to 4 sessions of heating: 60 s at 40 °C, 30 s at 470 °C, 120 s at 470 °C and 60 s at 40 °C. This makes a good contact between the semiconductor surface and the metal layers, and the Ge+Au alloy will go inside the wafer,

and touch the 2DEG.

10. Final cleaning

This is the very last step in the cleaning room, when we clean our heterostructure again in the ultrasonic bath, and after that with acetone, methanol and isopropanol, resulting in a complete dry and clean chip.

11. Creating our quantum ring structures

Once we have finished with our wafer preparation, the next steps belong to the AFM technique. I have to mention that we had to make many tries to write a good structure. But from a lot of structures written on our surface, we choose two of them (with different shapes), that we thought to be the best. So, as we just said, we prepared our sample to put in the AFM device. First we had to bond some wires in order to have conduction between the tip and the sample, so that the oxidation would be possible (see section 4.3). We cleaned every of the stars-like mesas, for quite a long time, before writing, first a larger region of about $30 \times 30 \mu\text{m}^2$ and after that a smaller region of about $10 \times 10 \mu\text{m}^2$. Our structures have needed a space of about $5 \times 5 \mu\text{m}^2$ for writing. The cleaning of the surface was made using a silicon tapping mode tip (see section 4.1.3). Once the cleaning was finished, we prepared our structures for writing. First we start our current source which was set to give 800 nA. This current was chosen due to the reason of tip protection. We prepared our humidity system, presented in section 4.3. Our structures were written at a humidity of about 70 %. In the meantime we prepared our lithoscript-programs. Both programs are given in appendix A. We will not discuss here their functioning. I will make a brake in our fabrication steps for presenting our two quantum ring structures in detail.

You will see in the figure 5.13 AFM pictures of both structures. They are not the complete pictures. You cannot see in figure 5.13, the connections with the star arms. These connections are made for creating insulating regions, so for delimiting the gate contacts and the source and drain contacts, respectively. They are also created using local anodic oxidation technique. We have to mention for the first, that both structures were written two times without applying any current to the tip, and three times, with applying the current to the tip. This technique is very often used. When writing without current, nothing will happen on the surface, but the piezo-crystal has time to get used to the shape of the structure. This is like a memory effect. And afterwards when you write with current, the writing accuracy is much better.

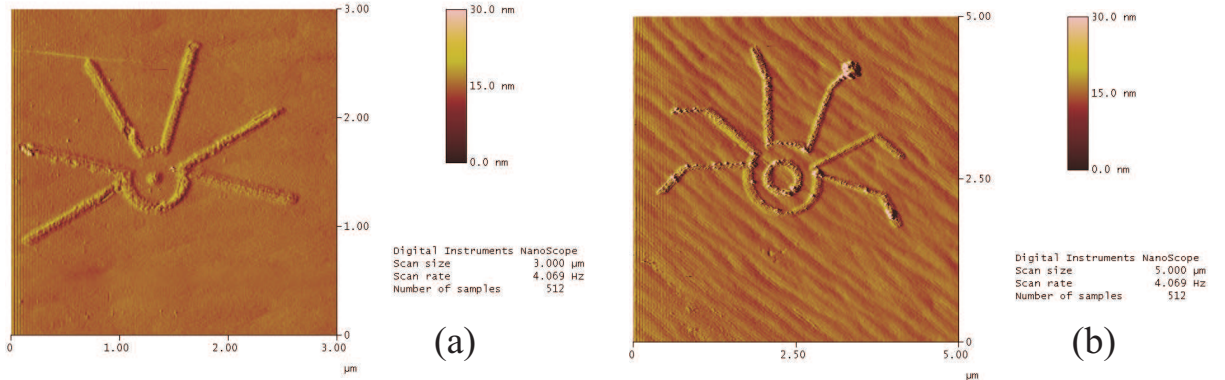


Figure 5.13: The AFM picture of: (a) a quantum ring with a dot in the middle, (b) a ring in a ring structure.

Our first structure is a quantum ring with a dot in the middle, see figure 5.13(a). It has an inner diameter of 500 nm, and the dot has 140 nm. The thickness of the lines are about 135 nm and they are about 4 nm high. This quantum ring has 2 contacts for source (S) and drain (D), respectively and also it has four gates: the upper gate (G1) which controls the energy of the electrons in the upper part of the ring and the coupling to the leads, the lower gate (G2) which mainly controls the flowing of the current in the lower part of the ring, the source gate (G3) which controls the current that enters in the ring and the drain gate (G4) which controls the current that exit from the ring. This quantum ring has the advantages that is very small and easy to write (the lithoscript-programm is quite simple), but on the other hand, it has an important disadvantage. It cannot be very well controlled. This means that if we apply, for example, a voltage to the lower gate, due to the fact that the structure is quite small, this voltage, will influence also, the flow of the current in the upper part of the ring. Sometimes we don't want this. On the other hand, if we apply a voltage to the upper part we could influence, the lower part. All 6 contacts of this ring are also shown in figure 6.1(a).

Our second structure is a quantum ring with another ring in the middle, see figure 5.13(b). The bigger ring has an inner diameter of 1 μm and the smaller ring has an inner diameter of 300 nm. The lines are about 185 nm thickness and they are of about 5 nm high. It has also, the same contacts for source (S), drain (D), upper gate (G1), lower gate (G2), source gate (G3) and drain gate (G4), who plays all of them the same rules like in the first structure. This structure, as you see, is much bigger than the first one, that is why it is much more difficult to write because of accuracy. But at this time,

it offers a better separated control of the ring-parts. You can much better control independently the flowing of the current in the lower and upper parts of the structure, respectively. All contacts for this ring are shown in figure 6.1(c)

12. Preparing for measurements

The next step after finishing our rings, was to bond all the wires that are necessary for source, drain and all four gates, respectively, and our sample was finished for measuring. We had first to make some preliminary measurements in a helium bottle, which let us to see the breakdown voltage of each barrier. For this a temperature of about 4 K (given by the He bottle) is sufficient. So, if our structures looked good, we can start our real measurements. For this we had first to build our rack with all the devices necessary for our experiments, and after that to prepare the loading of the probe (tube) (with our sample) into the cryostat. Our mixture cryostat used, is already presented in section 5.1. The preparation for measuring is quite simple, due to the fact that it is totally controlled by the ISO-Bus computer (see figure 5.10). The mounting of our sample in the probe is quite difficult, because while building, the bond wires could be broken very easily, and we had to measure with more attention, that all the contacts were working properly. The probe loading is based on a computer sequence so it is relatively simple to follow the computer instruction. Once the probe is completely load, we had just to wait for reaching the base temperature of our cryostat (about 20 mK). Our dilution refrigerator has to be refilled two times per week, with ^4He and N_2 , for the main bath of the cryostat, for the shield and for the cold trap, respectively. It is not recommended to make measurements while the system is refilling, due to the fact that the measurements could be affected.

We will see in the next section the measurements we made, and first of all it is important to know that in all our experiments we will measure the conductance through the ring, while varying different parameters.

5.4 Conclusions

In the first section of this chapter, you had a larger overview about our measurement setup and about our sample preparation.

It is obvious now that we need very special equipments for obtaining very low temperatures necessary for forming the 2DEG. In the first part you can see some properties of the liquid helium that is the essential ingredient for our equipment. You can already understand that there is a lot of different

equipment and you can decided what type to be used in your experiment. We choose to use a $^3\text{He}/^4\text{He}$ dilution refrigerator in order to obtain very low temperatures (about 20 mK). You had an overview about this cryostat and all the electronic equipment that had been used.

The next section contains a larger description of the sample fabrication. Every mentioned step has a greatest importance in preparation of our sample. We cannot jump over any step, in order to obtain a good chip. Our mesa structures were prepared in a cleaning room, and quantum rings have been made using the local anodic oxidation technique with an AFM. In this moment this technique gives good results especially for writing very complex structures and the highness of the oxide lines is about 10 nm. Our potential barriers hold up to about ± 400 mV breakdown voltage so it's sufficient.

Chapter 6

Experimental results

In this chapter we will look at some of our experimental measurements. Every studied phenomenon is first based on a theoretical review and after that, the real measurements follow. We will try to compare every time with the theoretical concepts. The section will start with some basic results, and it follows the Ahoronov-Bohm effect. It will continue with Fano-resonances and other possible effects. All our measurements have been performed at the base temperature of $T \sim 20$ mK, if not stated otherwise. I have to mention also, that there are different setups for rings and Hall-bar measurements, and we will specify the differences every time¹.

6.1 Basic results

As you will see, during our measurements, sometimes we need our ring to be quite open, other times to be more closed. We have started our measurements with some basic experiments that let us know the different regimes of our rings.

This means that we can make such a plot where we can step a gate, and sweep another gate. The sweep procedure consists in tuning a parameter in certain steps. The step procedure means that you can tune one parameter in larger steps and for every step you tune (sweep) another parameter. These kind of measurements are quite long because we have to make a lot of trials with different gates and with the back gate, too, for choosing the correct values for different regimes. We choose two such plots to show, and they are presented in figure 6.1. I have to give some explanations for the clarity of these plots. They show the conductance of the rings as a function of gate

¹Parts of the theoretical concepts of the presented experiments are published in special literature, listed to the end of this thesis, see ref. [13, 19]

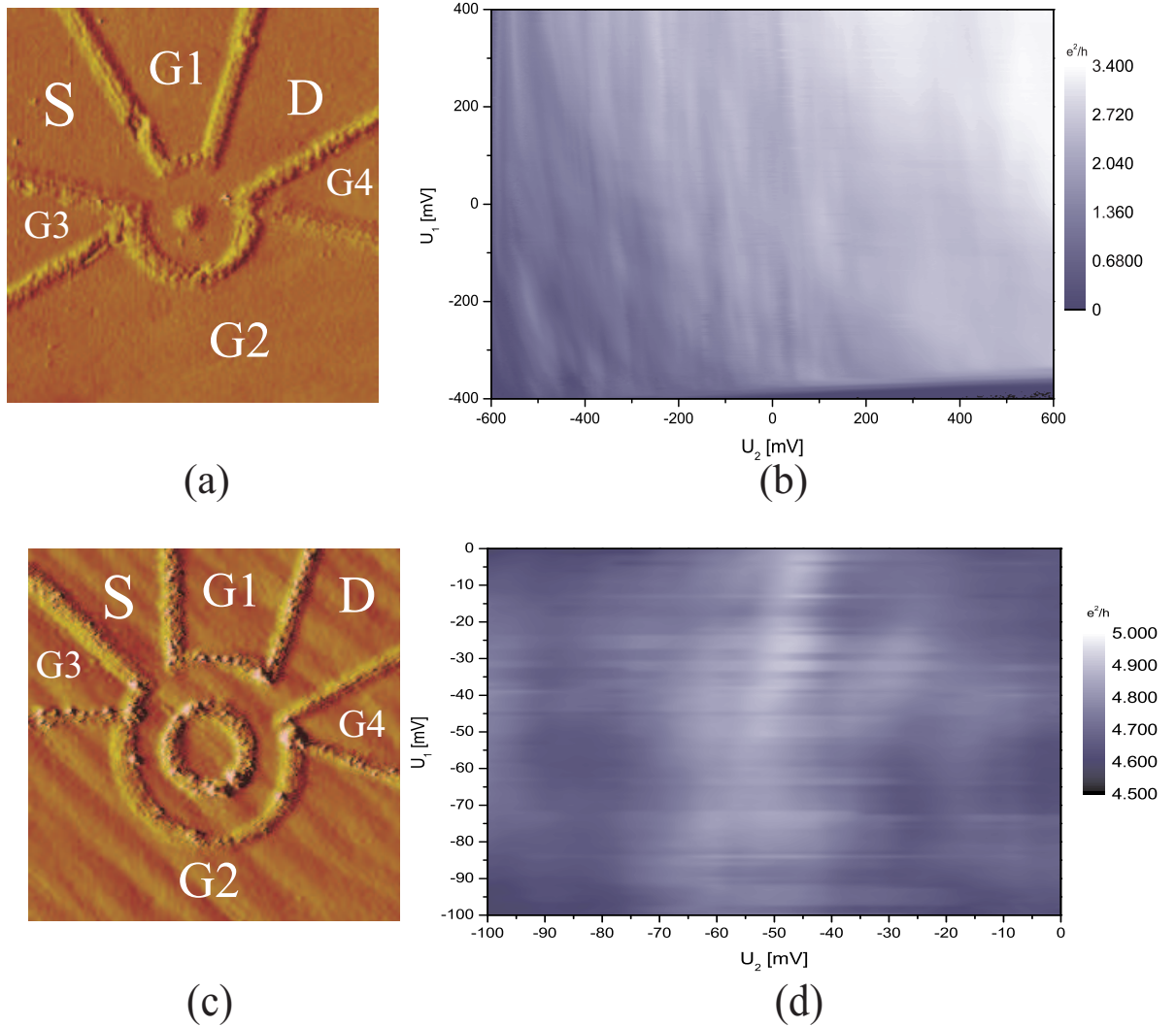


Figure 6.1: (a) The ring with a dot in the middle. (b) A gate-gate plot for the ring with a dot in the middle, with $U_3 = U_4 = -250$ mV and $U_{BG} = -100$ V. (c) The ring with another ring in the middle. (d) The gate-gate plot for the ring with another ring in the middle with $U_3 = U_4 = -20$ mV and $U_{BG} = -25$ V.

1 and gate 2 voltages, respectively. As you see in the legend (on the right sides of the plots), the white color means high conductance and the dark blue color means low conductance. On base of this plots we can notice the behavior of the rings. For example, for the first ring (see figure 6.1(b)), you can see that in the lower left corner, the ring is quite closed, but begins to be opened more and more with increasing gate voltages. In case of the second ring (see figure 6.1(d)), the structure is quite open for all the range (please note the scale in the right-side of the plot). As we said before, these plots help us to have a larger overview about our structures. After some of such graphs we can decide about the gate voltages to use for a certain regime.

6.2 Ahoronov-Bohm effect

In this subsection we will show the measurements on our two quantum rings with a dot in the middle, and with another ring in the middle, respectively (see section 5.3). The first ring has a diameter of 500 nm and it is fabricated by nanolithography using an atomic force microscope (AFM). The second ring has a diameter of 1 μm and it is fabricated using the same technique. With direct local oxidation by an AFM tip two ring geometries were directly written into our GaAs/AlGaAs-heterostructure, presented in section 5.3. The exceptionally short circumference of the rings reduces decoherence due to the scattering. We will start with some theoretical concepts and after that look at the real measurements.

6.2.1 Introduction

In quantum mechanics electrons are described by the wave function Ψ . This leads to many phenomena unexpected from the classical description of electrons as point-like particles. One of the most striking effects, tunnelling through a potential barrier, has been investigated in an earlier section of this thesis, see chapter 2. The wave nature of the electrons has an even more surprising consequence. Electrons can interfere with themselves if they are transmitted through a ring structure like the one shown in figure 6.2. Such a ring acts as a beam splitter for the incident electronic wave function. Ψ will split into an upper and a lower part that traverse the respective ring arms. If we assume that the phase coherence length l_Φ is long compared to the circumference C of the ring there will be an interference between the two parts at the ring exit. For a perfectly symmetric ring the phase difference is zero and thus we have constructive interference. In the contrary case we have destructive interference.

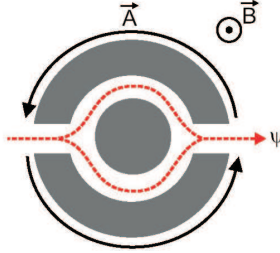


Figure 6.2: A ring structure splits the incident electronic wave function Ψ into two parts that interfere at the ring exit if scattering is absent. The vector potential \vec{A} influences the relative phase of the two parts of Ψ at the ring exit.

The relative phase in the ring arms is controlled by applying a perpendicular magnetic field $\vec{B} = \nabla \times \vec{A}$. The vector potential \vec{A} leads to an additional phase factor for the wave function in both arms [48]:

$$\exp \left[-i \frac{e}{\hbar} \int_C \vec{dl} \cdot \vec{A} \right] = \exp \left(-i 2\pi \frac{\Phi}{\Phi_0} \right) \quad (6.1)$$

$\Phi = \int_C \vec{dl} \cdot \vec{A}$ is the magnetic flux through the ring and $\Phi_0 = \frac{h}{e}$ the flux quantum. According to formula 6.1 the wave traversing through the lower part of the ring in figure 6.2 picks up a phase $\frac{\pi\Phi}{\Phi_0}$ whereas the part in the upper arm changes its phase by the negative of the above because it moves in the opposite direction relative to \vec{A} . The interference at the ring exit leads then to an oscillating phase between 0 and 1:

$$\exp \left(-i\pi \frac{\Phi}{\Phi_0} \right) + \exp \left(i\pi \frac{\Phi}{\Phi_0} \right) = 2\cos \left(\frac{\Phi}{\Phi_0} \right) \quad (6.2)$$

From this equation follows that the probability to find an electron at the ring exit oscillates with $\cos^2 \left(\frac{\Phi}{\Phi_0} \right)$. According to this result the transmission of the ring equals one if $\Phi = n\Phi_0$, with $n = 0, 1, 2, \dots$. This means for a transport measurement that each time the magnetic flux Φ threading the ring is an integer multiple of Φ_0 the conductance G will be maximal. This effect was predicted by Bohm and Aharonov in 1959 [49] and first experimentally observed by Chambers in an electron beam diffraction experiment [50].

Aharonov-Bohm oscillations with a periodicity of h/e in a condensed matter device were observed also, in a transport experiment on very small Au-loops [51]. The high electron densities in metals lead to an averaging of the Aharonov-Bohm oscillations of many different modes and thus to a reduced

amplitude. Even at mK temperatures the magnitude of the Ahoronov-Bohm oscillations lies below 1 % of the signal. Because of their relatively low carrier concentrations in the 2DEG, GaAs/AlGaAs-heterostructures were used as a substrate for the fabrication of ring systems with only few transmitting modes, see e.g. [52, 53, 54, 55] and references therein. For processing the samples usually well-established techniques like electron beam lithography and wet-chemical etching were utilized. Recently Ahoronov-Bohm oscillations with an amplitude of 30 % were observed in a vertical interferometer [56].

6.2.2 Transmission through a symmetric ring

In principle for all the experiments the basic considerations of the introduction can be applied. For a more accurate description of (real) rings a calculation based on scattering matrix theory yields a transmission probability t through a symmetric ring with no elastic scattering:

$$t(\chi, \Phi, \epsilon) = \frac{4\epsilon \sin^2(\chi) \cos^2(\Phi)}{[a^2 + b^2 \cos^2(\Phi) - (1 - \epsilon) \cos^2(\chi)]^2 + \epsilon^2 \sin^2(\chi)} \quad (6.3)$$

with $\Phi = \pi\Phi/\Phi_0$. ϵ measures the scattering at the ring exit and entrance and $\chi = k_f C/2$ the product of the Fermi wave factor k_f and the circumference C of the ring. An exact derivation of the above equation can be found e.g. in Ref [57, 58]. a^2 and b^2 are coefficients that directly result from the scattering matrix and depend on ϵ . In this section we work with a device in the limit of open point contacts. For such quantum point contacts in the ballistic regime we have to choose $\epsilon = 0.5$ which result in $a^2 = 1/4$ and $b^2 = 1/4$ [58].

In figure 6.3 a plot of the transmission t as a function of Φ/Φ_0 is shown. The phase coherence length l_Φ is infinite and χ was set to $\pi/4$. t varies between $t = 0 \Leftrightarrow G = \min$ and $t = 1 \Leftrightarrow G = \max$ as a function of the applied magnetic field. Please note the periodicity of the curve with Φ_0 .

6.2.3 Transmission through an asymmetric ring

For a realistic device equation 6.3 has to be modified because there exists usually a length difference of the ring arms ΔL . This leads to an additional phase difference δ between the two parts of the wave function of $\delta = k_f \Delta L$. Considering this in the model the transmission probability has to be modified to:

$$t(\chi, \Phi, \delta, \epsilon) = \frac{4\epsilon [\sin^2(\chi) \cos^2(\Phi) + \sin^2(\Phi) \sin^2(\delta) - \sin^2(\chi) \sin^2(\delta)]}{[a^2 \cos(2\delta) + b^2 \cos^2(\Phi) - (1 - \epsilon) \cos^2(\chi)]^2 + \epsilon^2 \sin^2(\chi)} \quad (6.4)$$

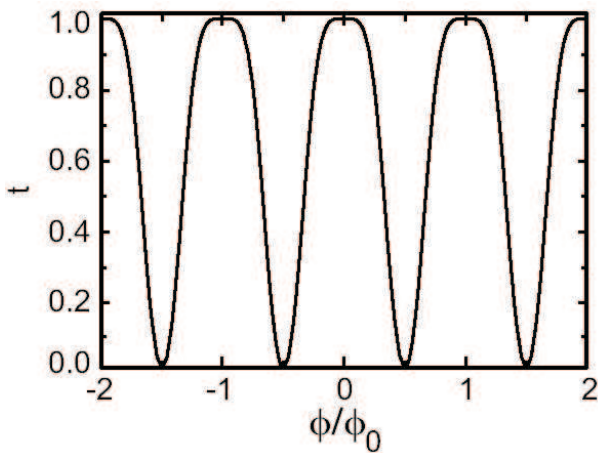


Figure 6.3: Transmission t through a symmetric ring structure as function of the flux Φ threading the ring. $\Phi_0 = h/e$ is the flux quantum.

Please note that equation 6.3 is a special case of the above equation for $\delta = 0$. Equation 6.4 also applies when e.g. in a symmetric ring the Fermi wave length is different in the ring arms. This can be achieved by e.g. an outer gate voltage that couples to one ring arm. This changes the Fermi wave length and thus the effective arm length. As a consequence δ is controlled by an outer parameter.

The result of calculations with equation 6.4 for $\delta = 0, \pi/4, \pi/2$ and $\chi = \pi/4$ are shown in figure 6.4. As mentioned above, for $\delta = 0$ we get the same oscillations with a maximum at zero flux (upper curve) as for the symmetric case in figure 6.3. $\delta = \pi/4$ leads to a signal with halved period and a much smaller amplitude (central curve). Additionally the maximum at zero magnetic field changes into a minimum indicating a phase change of the wave function in the ring. This becomes even more clear when looking at the third and lowest curve in figure 6.4 with $\delta = \pi/2$. The original curve reappears but is shifted by half a period. The occurrence of the phase jumps is periodic with a period $\delta = \pi$.

The tuning of the phase at zero magnetic field is sometimes called electric or electrostatic Aharonov-Bohm effect. It seems as though one can influence the phase of the wave function with the scalar potential of an electric field. But the underlying process is completely different from its magnetic pendant. Whereas the vector potential \vec{A} changes directly the phase factor in Ψ the electric field changes the Fermi energy and thus the wave length and energy of the incident electron.

In the above equation the phase coherence length l_Φ is not considered.

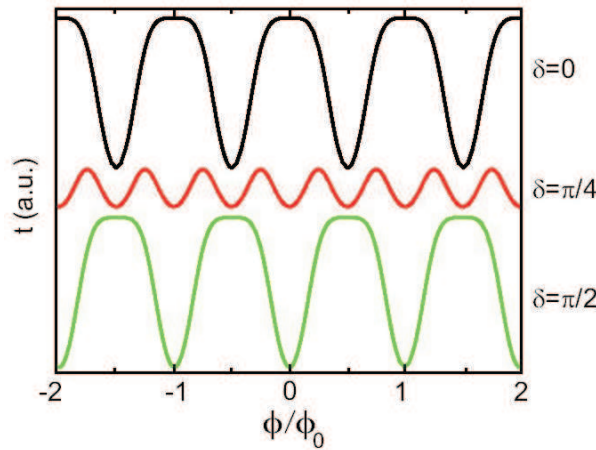


Figure 6.4: Transmission t through an asymmetric biased ring structure as function of the flux Φ/Φ_0 for $\delta = 0, \pi/4, \pi/2$ and $\chi = \pi/4$. The curves are offset for clarity. The maximum at $\Phi = 0$ for $\delta = 0$ changes into a minimum for $\delta = \pi/2$. Note the frequency doubling and the reduction of the oscillation amplitude for $\delta = \pi/4$.

In a real device l_Φ will be finite because of scattering, finite temperatures, and defects. If an electron is scattered during the passage in one ring arm this can be considered as a "which-path" measurements. The interference pattern is destroyed [59] and leads to a reduced oscillation amplitude of the conductance in the Aharonov-Bohm effect.

6.2.4 Ahoronov-Bohm setup and experiments

1. Preliminary remarks

In this section we present data measured on an asymmetric quantum ring with two tuneable point contacts. The ring was fabricated using an atomic force microscope (AFM) as nanolithographic tool, see section 5.3. We focus on the ballistic regime, where the conductance of the point contacts G lies around $2(e^2/h)$. The quantum ring acts in this regime as an electron interferometer.

The electronic setup is shown in figure 6.5. As we just said in section 5.2.3, we used a lock-in amplifier, which generates an oscillation to the source contact. This signal is received from the drain contact by a current amplifier. The amplified current is then converted into a voltage which is proportional to the current. This voltage is measured by an electronic multimeter. We measured all the time the conductance through the ring and we applied

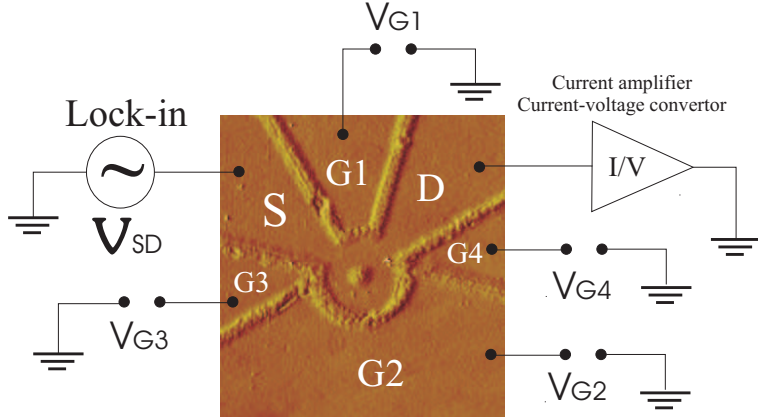


Figure 6.5: Setup for measuring Ahoronov-Bohm effect.

different DC voltages to the gate contacts, using a digital-analog converter, see section 5.2.3. We first had to choose the correct gate-voltages to have an open ring, but not to open. The values for the gates have been chosen on base of measurements presented in section 6.1.

A schematic picture of the ring is shown in figure 6.6(b). The solid lines depict the oxide and the light grey areas around them the depletion width of some ten nanometers in our structures, see Chapter 3. We illustrate the expected electron path in the open transport regime with the dashed lines. The diameter of this electronic path is ~ 260 nm. Since the phase coherence length in the unstructured 2DEG is $l_\Phi \sim 5 \mu\text{m}$ and the circumference of the ring is only $C = 500$ nm we assume that the ring is in the ballistic regime and neglect effects of inelastic scattering.

Figure 6.7(a) shows the conductance $G(B)$ of the quantum ring with a dot in the middle, in the open regime with $U_1 = -335$ mV, $U_2 = -315$ mV, $U_{3,4} = +50$ mV, $U_{BG} = -100$ V and $T = 18$ mK ($R < h/e^2$) in a perpendicular magnetic field B . We observe Ahoronov-Bohm oscillations with an oscillation amplitude of about 15%. We extract a period $\Delta B \sim 74$ mT from the data in figure 6.7(a). The clear oscillations without any distortions together with the high amplitudes indicate that we could have few conducting channels in the ring.

For a further analysis of the periodicity we use a Fourier transformation of the data. The amplitude spectrum of the measurement in figure 6.7(a) as a function of the oscillation frequency f is shown in figure 6.7(b). The dominating feature is at frequency of $11/T$. This corresponds to $\Delta B \sim 74$ mT and indicates that a flux quantum $\Phi_0 = h/e$ enters the area enclosed by the electron path every ~ 74 mT. Each additional flux quantum in the

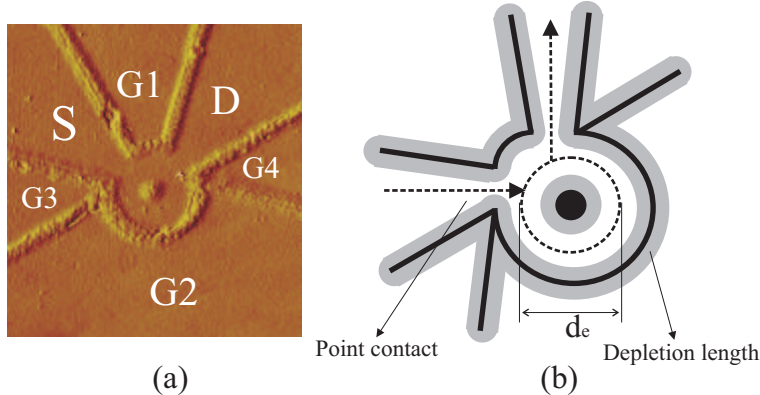


Figure 6.6: (a) AFM image of the ring structure. (b) Schematic picture of the ring. The solid lines indicate the insulating lines and the grey area the width of the depletion in the 2DEG. The dashed trajectory has a diameter of $d_e \sim 260$ nm.

ring changes the phase by 2π and thus we observe a full oscillation period. We estimate the diameter of the electron orbit in our ring from the period of $\Delta B = 1/f$:

$$\Phi_0 = \frac{1}{4} \Delta B \pi d_e^2 \Rightarrow d_e = 2 \sqrt{\frac{h}{\pi e \Delta B}} \quad (6.5)$$

With $\Delta B \sim 74$ mT a flux quantum is added to the ring area and we determine the diameter d_e of the dominating electron orbit in our ring to $d_e \sim 260$ nm. This fits perfectly to the geometry of our device. The observation of only one dominant frequency at $11/T$ indicates that only a single conducting channel is present in this voltage regime. In figure 6.7(c), you see the Aharonov-Bohm oscillations for the second quantum ring with another ring in the middle, in the open regime with $U_1 = -170$ mV, $U_2 = 0$ mV, $U_{3,4} = -100$ mV, $U_{BG} = -100$ V and $T = 8$ mK. In this case, Aharonov-Bohm oscillations have an amplitude of about 3 %. In figure 6.7(d) is depicted the Fourier transformation for this ring. The periodicity of the oscillations is $\Delta B \sim 7.5$ mT and we notice one dominant frequency at $132/T$. With similar calculations we can find the electronic diameter of the second ring: $d_e = 840$ nm. This value also fits perfectly in our ring geometry. I have to mention that Fast Fourier Transforms involves the subtracting of the background conductivity.

Also, if we look closely to both Fast Fourier Transforms, we can notice other peaks that appear at about the double base frequencies. These double frequencies can be explained by interference with an electronic wave that has travelled a full circle in the ring before exiting.

This type of measurements gives us some information about our rings. In

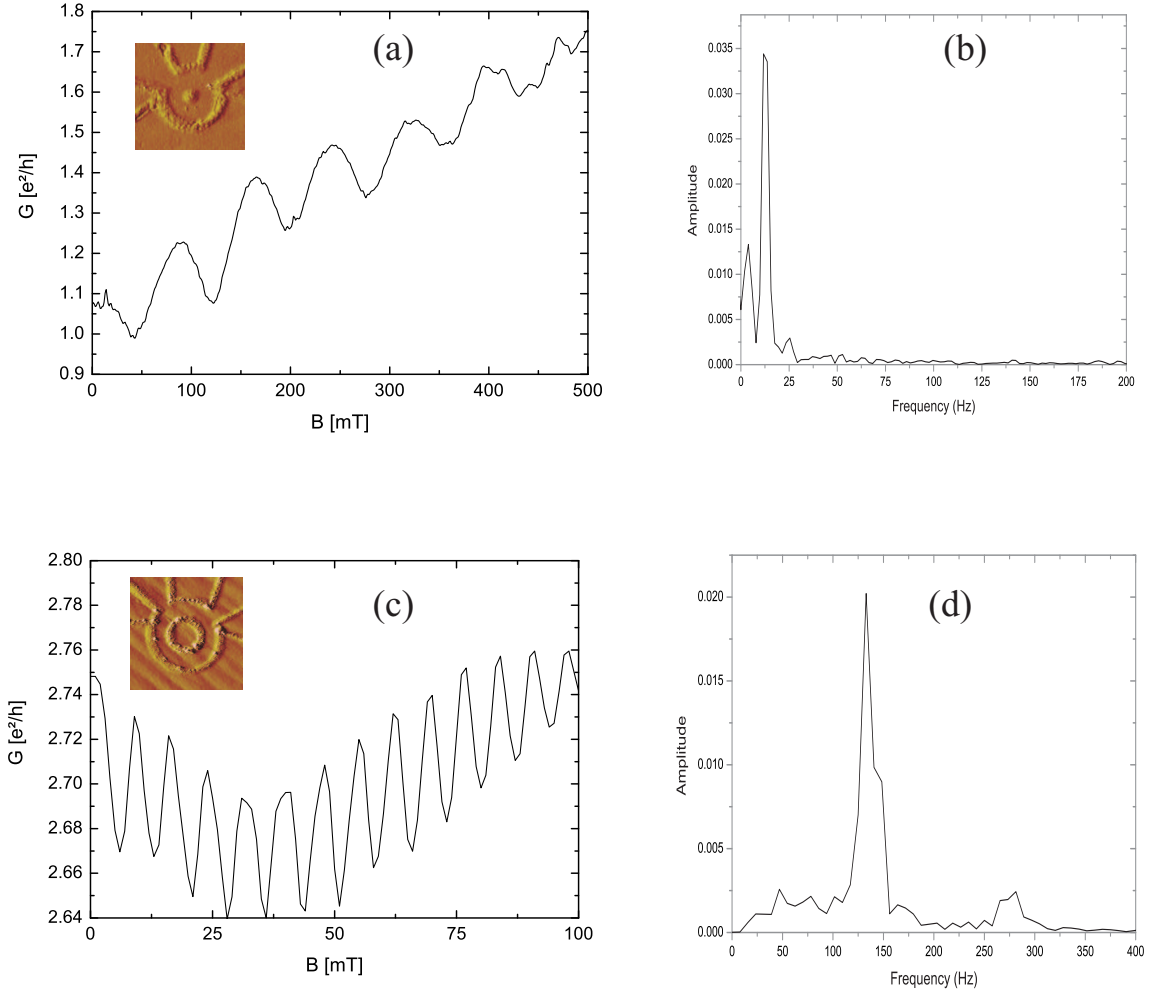


Figure 6.7: (a) Conductance G through the quantum ring with a dot in the middle, as function of the magnetic field B at $U_1 = -335$ mV, $U_2 = -315$ mV, $U_{3,4} = +50$ mV, $U_{BG} = -100$ V and $T = 18$ mK. The period is $\Delta B = 74$ mT (b) The Fourier transformation of the data shows one distinct peak at $\sim 11T^{-1}$. (c) Conductance G through the quantum ring with a ring in the middle, as function of the magnetic field B at $U_1 = -170$ mV, $U_2 = 0$ mV, $U_{3,4} = -100$ mV, $U_{BG} = -100$ V and $T = 8$ mK. The period is $\Delta B = 7.5$ mT (d) The Fourier transformation of the data shows one distinct peak at ~ 132 T⁻¹. All the plots have subtracted the background for clarity.

fact this is a confirmation that our ring works properly.

2. Gate voltage dependence and magnetic field dependence

In this paragraph we will study the ring conductance as a function of B and U_2 . We will start first with the ring with a dot in the middle. You can see in figure 6.8(a) a large plot of the conductance as a function of B and U_2 . You can already see Ahoronov-Bohm oscillations. I remind you again that white color means high conductance and dark blue color means low conductance. You can see for different positions that the conductance fluctuates between white and blue. This means that it oscillates. For better clarity we make sections across the U_2 -direction (figure 6.8(b)) and across the B -direction (figure 6.8(c)). Following the discussion of asymmetric ring structures, as we have tuned only one lateral gate, we expect to observe phase jumps in the Ahoronov-Bohm oscillations of our quantum ring. A closer look at the plot in figure 6.8(a) already indicates this. For a clear demonstration of this characteristic we depicted the conductance G as a function of U_2 for three magnetic fields: $B = 195$ mT, $B = 230$ mT and $B = 247$ mT, in figure 6.8(b). At $B = 195$ mT (lowest curve), G has a minimum at $U_2 = -320$ mV whereas at $B = 230$ mT the curve is shifted and shows a maximum at $U_2 = -320$ mV. Thus the phase of the wave function changed by π by applying an outer gate voltage. This is the so-called "Electrostatic Aharonov-Bohm Effect" (see theory). More than that we can also see such phase jumps with magnetic field and a constant gate voltage (see figure 6.8(c)). We depicted also just three curves corresponding to $U_2 = -320$ mV, $U_2 = -340$ mV and $U_2 = -355$ mV. This is the real Aharonov-Bohm effect. You can see that $U_2 = -320$ mV (the lowest curve), G has a minimum for $B = 300$ mT (destructive interference) and for $U_2 = 355$ mV (the upper curve), G has a maximum for almost the same magnetic field (constructive interference).

Similar results are depicted in figure 6.9 for the ring with another ring in the middle. Here the oscillations are much more clearly to see on the large plot (see figure 6.9(a)). Figure 6.9(b) shows the electrostatic Aharonov-Bohm effect that is quite similar with the plot depicted for the first ring. Also here, the curves show relativ phase shifts due to the different magnetic fields, but note that they are spaced much further then just a single magnetic Aharonov-Bohm-period. The oscillations themselves appear as a consequence of the changing of the electric field. In figure 6.9(c) you can see again oscillations for different gate-voltages. The shifting of the phases is much more clearly to see here. In the mean time, if you look closely to this plot, you can notice some kind of slow modulation of the Aharonov-Bohm oscillations. For different curves, the oscillations vanished in the beginning

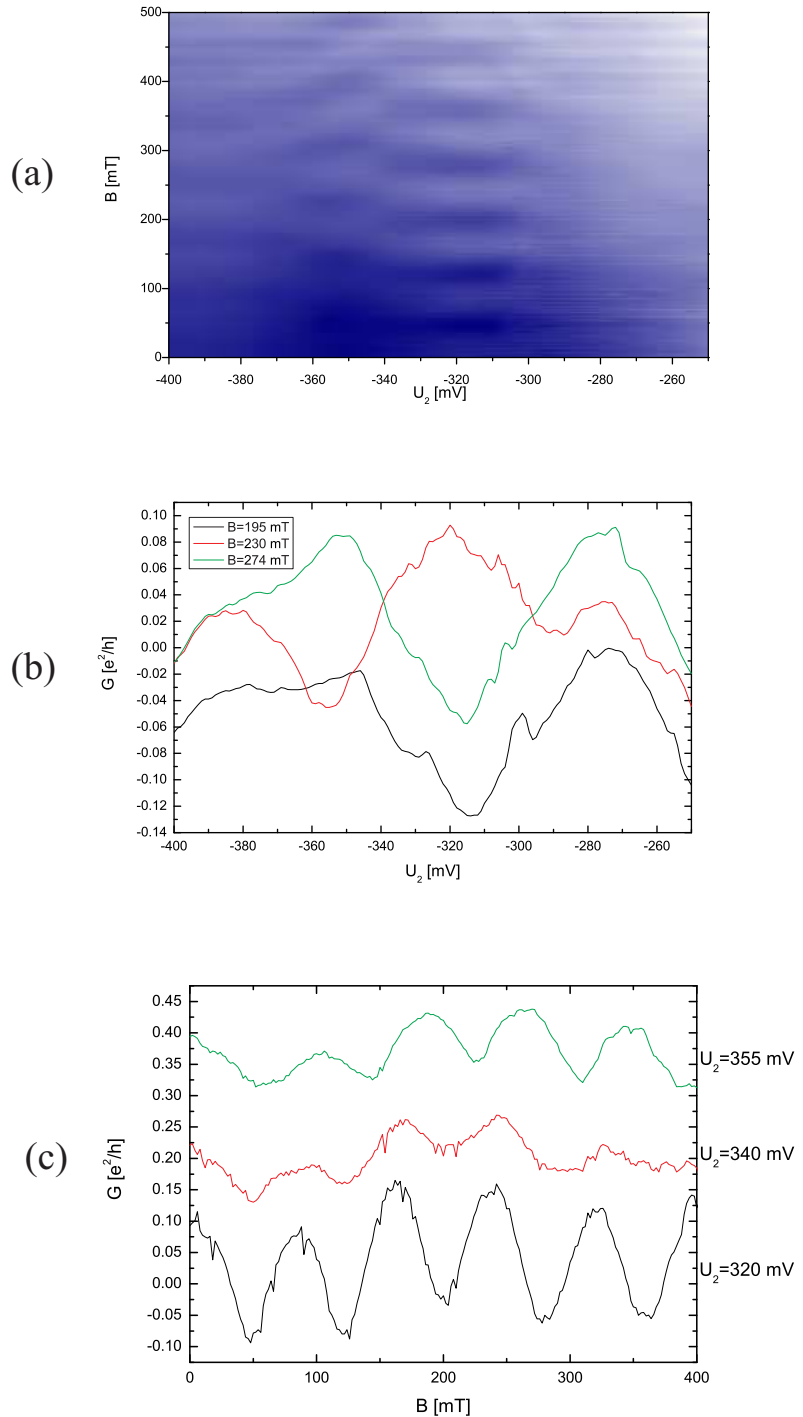


Figure 6.8: (a) Conductance G through the quantum ring with a dot in the middle, as function of the magnetic field B and gate 2 voltage U_2 . (b) A cross section along the x-direction showing the conductance as a function of U_2 for different magnetic fields. (c) A cross section along the y-direction showing the conductance as a function of B for different gate voltages. The background is subtracted and the plots are offset for clarity.

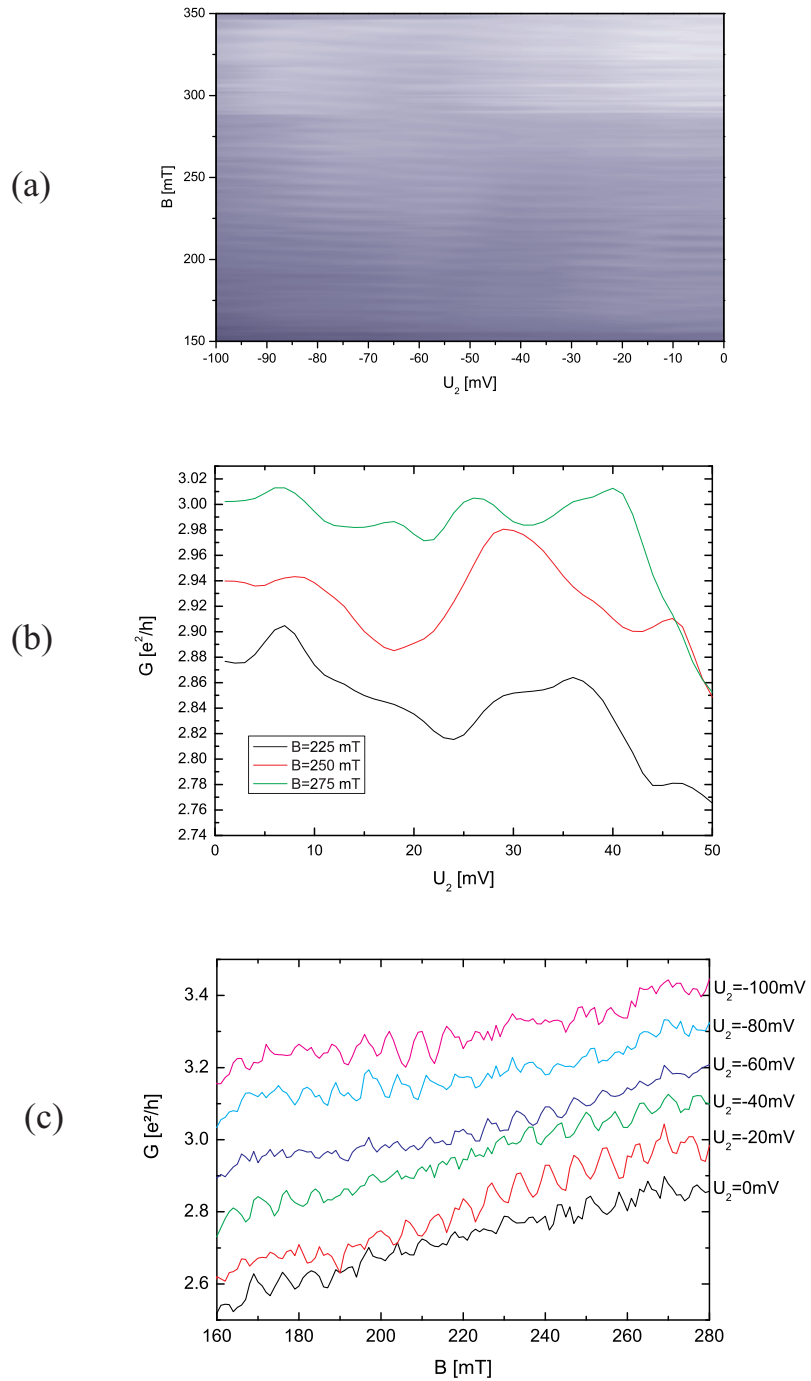


Figure 6.9: (a) Conductance G through the quantum ring with a ring in the middle, as function of the magnetic field B and gate 2 voltage U_2 . (b) A cross section along the x -direction showing the conductance as a function of U_2 for different magnetic fields. (c) A cross section along the y -direction showing the conductance as a function of B for different gate voltages. The background is subtracted and the plots are offset for clarity.

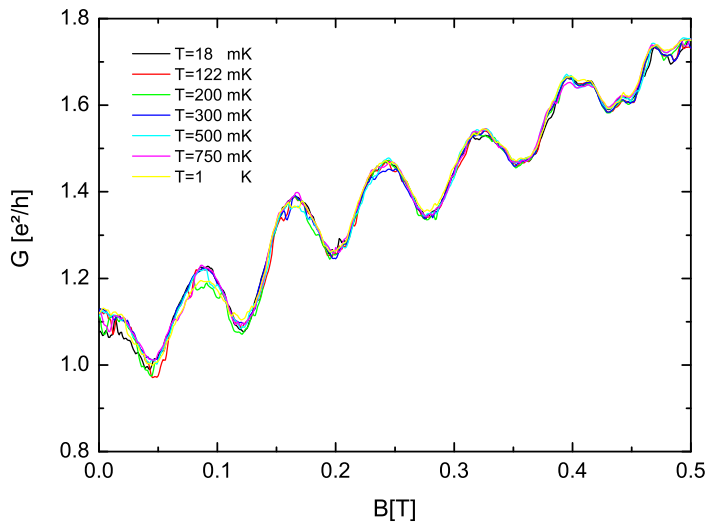


Figure 6.10: The magneto-conductance for different temperatures.

and start to appear and increase slowly following a new vanishing again. We didn't expect to see such a behavior here, and for moment we cannot explain it.

2. Temperature dependence

In figure 6.10 is depicted the magneto-conductance $G(B)$ for different temperatures in case of the first ring with a dot in the middle. We can notice that our curves are nearly identical, meaning that all the time we have a single occupied subband with electrons. If the curves had changed their shape, it could mean that with raising the temperature more subbands in our 2DEG were occupied.

6.3 Shubnikov-de Haas oscillations

We now turn our attention to the Shubnikov-de Haas (SdH) oscillations at small and intermediate magnetic fields. This oscillations are quite interesting because they permit us to find out the density of states and the density of the electrons.

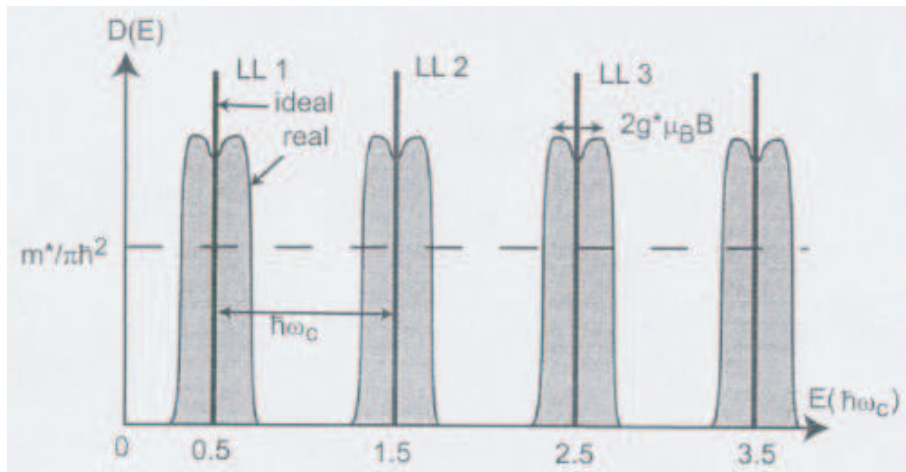


Figure 6.11: Ideal and real density of states of a Landau-quantized 2DEG which is spin-degenerate at $B = 0$. The δ -functions broaden due to fluctuations of the conduction band bottom, while the spin degeneracy is lifted, and Zeeman doublet results for non-zero effective g -factors g^* [19].

6.3.1 Landau levels

If our sample is placed in a perpendicular magnetic field, the z-direction is of no further interest for us, since B does not influence the electronic motion in that direction. We therefore assume that the z-direction can be treated separately, leading to a quantized energy E_z , which is the conduction band bottom of the two-dimensional electron gas. We can define the cyclotron frequency ω_C as the angular frequency of the electron in the magnetic field and the corresponding energy eigenvalues are [19]:

$$E_j = \hbar\omega_C \left(j - \frac{1}{2} \right) \quad (6.6)$$

with j being a positive integer. This leads to form the so-called Landau levels, as you can see in figure 6.11.

In real samples, the Landau levels are broadened to an approximately Gaussian shape by potential fluctuations and split via the two possible alignments of the electron spin with respect to the magnetic field (see figure 6.11). The spin splitting is described by the effective g -factor, g^* . For bulk GaAs, $g^* = -0.44$. In general, the Landau level at the Fermi energy is only partly occupied, and it is thus useful to introduce a quantity that measures the degree of filling of Landau levels. This is the task of the filling factor ν , defined

as:

$$\nu = \frac{g_s E_F}{\hbar \omega_C} \quad (6.7)$$

For the frequent case of $g_s = 2$ (spin degeneracy), $\nu = 2j$ means that j Landau levels are completely filled. Furthermore, in sufficiently strong magnetic fields, the spin degeneracy may be lifted due to the Zeeman effect. In that case, an odd integer value of ν means that one spin direction of Landau level $j = \nu/2$ is full, while the other is empty. The density of states of an ideal 2DEG in a perpendicular magnetic fields reads:

$$D(E) = \frac{g_s}{2\pi l_B^2} \delta(E - E_j) \quad (6.8)$$

with E_j given by equation 6.6 and l_B is the magnetic length. These Landau levels have been greatly treated in special books like ref. [19].

6.3.2 The quantum Hall effect and Shubnikov-de Haas oscillations

Back in 1980, K. von Klitzing and coworkers [60] discovered a quantization of the Hall resistance in 2DEGs residing in Si-MOSFETs. The resistivity in the 2DEG is a tensor with four components which are defined as:

$$\rho = \begin{pmatrix} \rho_{xx} & \rho_{xy} \\ \rho_{yx} & \rho_{yy} \end{pmatrix} \quad (6.9)$$

with $\rho_{yy} = \rho_{xx}$ and $\rho_{yx} = -\rho_{xy}$. When a current flows in x -direction, then the perpendicular resistance is $R_{xy} = \rho_{xy}$ and the longitudinal resistance is $R_{xx} = \frac{l}{b} \rho_{xx}$, where l and b are the geometrical dimensions of the Hall-bar in x and y directions (see figure 6.14). The Hall resistance is the perpendicular resistance (R_{xy}) in the Hall-bar structure. Measuring R_{xy} , we obtain such plateaux that are shown in figure 6.12, as well as in figure 6.13. These plateaux were observed at integer filling factors, i.e., for:

$$\rho_{xy}(B) = \frac{1}{\nu} \frac{h}{e^2} \quad (6.10)$$

where ρ_{xy} is the perpendicular resistivity, corresponding to R_{xy} and ν is defined by the equation 6.7. Subsequent experiments showed that this quantization is universal, in the sense that it is observed in all kinds of materials, provided the electron gas is two-dimensional. In fact the accuracy $\delta \rho_{xy}/\rho_{xy}$ can be of the order of 3×10^{-10} , such that the $\nu = 1$ - quantum

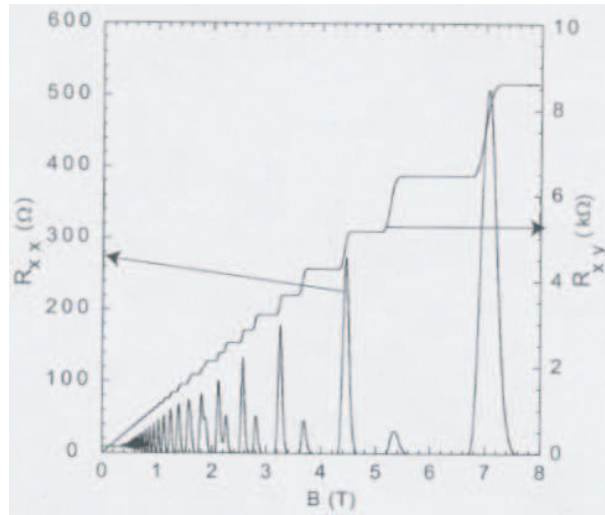


Figure 6.12: Shubnikov-de Haas oscillations and the quantum Hall effect. We look at a measurement of the longitudinal and the Hall resistance (R_{xx} and R_{xy} , respectively), of a two dimensional electron gas, as a function of a magnetic field applied perpendicular to the plane of the quantum film. The experiment has been performed at a temperature of 100 mK [61].

Hall plateau has been chosen as the resistance standard, with a resistance of $R_Q = 25812.807 \Omega$ per definition [62].

Furthermore, another quantization of ρ_{xy} has been discovered by Tsui [63]. In extremely high-quality samples, additional resistance plateaux are observed at $\rho_{xy} = h/ke^2$, with k being a rational number. This type of quantization is very pronounced in figure 6.13, but its discussion is beyond our scope. Interestingly, the accurate determination of e^2/h is highly relevant for quantum electrodynamics, since this ratio is contained in the fine structure constant, $\alpha = \frac{\mu_0 c e^2}{2 h}$, which describes the coupling of elementary particles to electromagnetic fields. The quantum Hall effect (QHE) is closely connected to another highly remarkable effect, namely the magnetoooscillation of the longitudinal resistivity ρ_{xx} , see figure 6.13. These oscillations are known as *Shubnikov – de Haas oscillations*. In fact, in these regions of quantized longitudinal resistance, ρ_{xx} becomes zero, with an accuracy comparable to that one of ρ_{xy} .

Figure 6.12 shows the resistance of a homogenous electronic quantum film along the direction of the current flow (the longitudinal resistance R_{xx}), as well as perpendicular to it (the Hall resistance R_{xy}). Any explanation for the quantum Hall effect should therefore also explain these oscillations, in particular the remarkable fact of vanishing resistance! It should be remarked

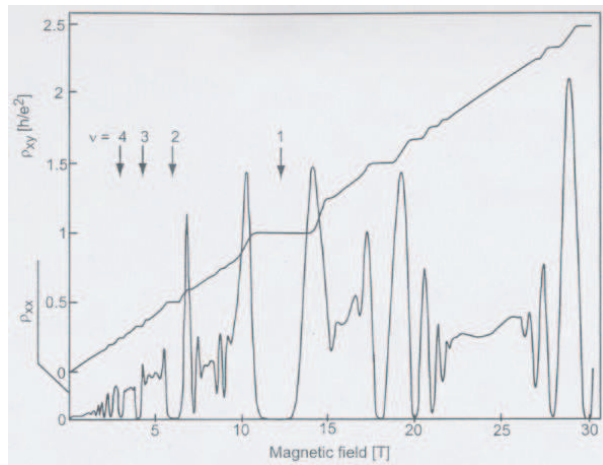


Figure 6.13: The quantum Hall effect and Shubnikov-de Haas oscillations in a GaAs/AlGaAs-heterostructure, measured in a dilution refrigerator at a temperature of 100 mK. A filling factor of $\nu = 1$ is reached at $B = 12$ T. Besides the integer quantum Hall effect, pronounced structures at fractional filling factors are observed [61].

that the quantum film does not become superconducting. You may further wonder why the resistance of a diffusive two-dimensional electron gas can vanish, while that of a ballistic one-dimensional electron gas remains non-zero. A possible explanation is that in quantum films placed in strong magnetic fields, the scattering of electrons is strongly suppressed when the density of states vanishes around the Fermi energy and the transport develops a one-dimensional character.

In fact the Schubnikov-de Haas oscillations appear as a consequence of the Landau quantization, which leads to an oscillation of the density of states over the energy-axis as it can be seen in figure 6.11. For detailed explanations you can use the literature list given at the end of this thesis [19].

6.3.3 Measurements of Shubnikov-de Haas oscillations

In this section we present data measured on the Hall-bar structure. The electronic setup is shown in figure 6.14. As we already said in section 5.3, we need for this kind of measurement (which is called "4-points measurement") an untouched Hall-bar structure. We apply a constant current between the contacts 1 and 2 so we can measure the voltage drop between the contacts 3 and 4. The signal is also given by a Lock-in amplifier, that generates a voltage which is applied to our structure over a $10 \text{ M}\Omega$ resistance, that is much higher

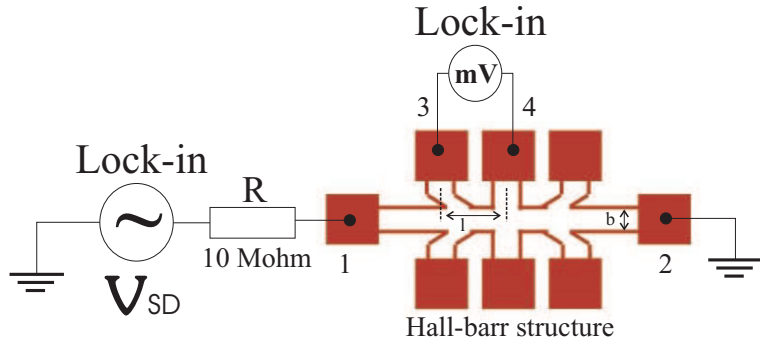
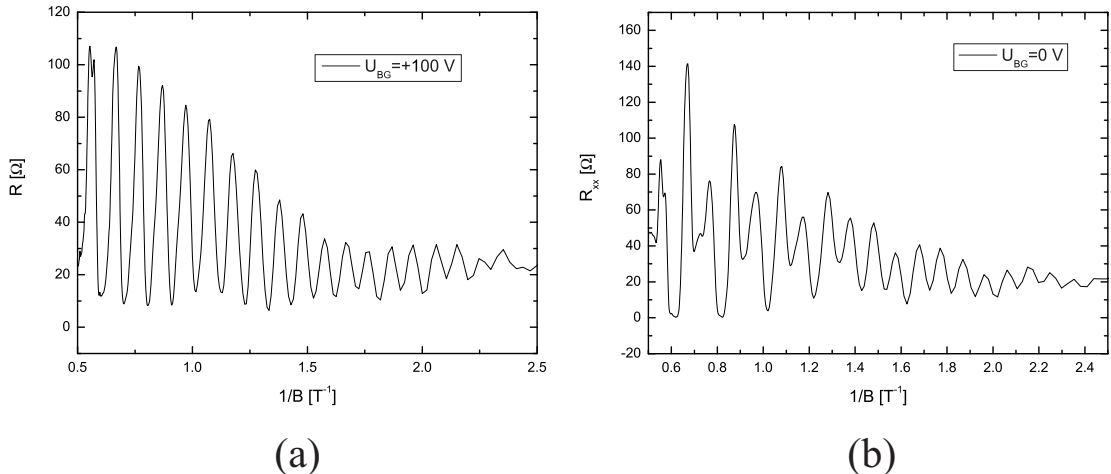


Figure 6.14: Setup for measuring Shubnikov-de Haas oscillations.

Figure 6.15: Shubnikov-de Haas oscillations for (a) $U_{BG} = 100$ V and (b) $U_{BG} = 0$ V, plotted over the inverse B -axis to obtain equidistant periodicity.

than the Hall-bar resistance. In this way we obtain a stable alternating current which passes along the Hall-bar structure (between the contacts 1 and 2). The Lock-in amplifier is also used for measuring the voltage drop between the contacts 3 and 4. The Shubnikov-de Haas measurements consist in tuning the magnetic field and measure the voltage drop between 3 and 4. You can already see in figure 6.15 the Shubnikov-de Haas oscillations for a back-gate voltage of $U_{BG} = +100$ V (figure 6.15(a)) and for $U_{BG} = 0$ V (figure 6.15(b)).

As we mentioned before, we can calculate now the density of the electrons in the 2DEG as well as the mobility of the electrons. For this we used the oscillations presented in figure 6.15(a). The period of this oscillations plotted against the inverse B -field is: $\Delta(1/B) = 0.09934 \text{ T}^{-1}$ for zero back-gate

Table 6.1: The density and the mobility of electrons for different back-gate voltages

U_{BG} [V]	n_e [cm $^{-2}$]	μ_e [cm 2 /Vs]
-200	$4.90166 \cdot 10^{11}$	$1.08833 \cdot 10^6$
-100	$4.87498 \cdot 10^{11}$	$1.13806 \cdot 10^6$
0	$4.86811 \cdot 10^{11}$	$8.85749 \cdot 10^5$
+100	$4.86615 \cdot 10^{11}$	$8.72543 \cdot 10^5$
+200	$4.73558 \cdot 10^{11}$	$8.32860 \cdot 10^5$
0 (4.2 K)	$4.59 \cdot 10^{11}$	$6.43 \cdot 10^5$

voltage. We can use the equations below:

$$n_e = \frac{g_s e}{h \Delta \left(\frac{1}{B} \right)} \quad (6.11)$$

and:

$$\mu_e = \frac{1}{R_{xx}} \frac{l}{e n_e b} \quad (B = 0\text{T}) \quad (6.12)$$

g_s is a spin parameter that is 1 for spin degeneration and 2 for spin splitting. e is the elementary charge, R_{xx} is the longitudinal resistance of the Hall-barr at zero magnetic field and l and b are the geometric dimensions of the Hall-barr structure. With this we can calculate the density of the electrons and obtain: $n_e = 4.86 \cdot 10^{11}$ cm $^{-2}$ and $\mu_e = 4 \cdot 10^6$ cm 2 /Vs. If we compare with the values from the institute that has grown our layers (see section 5.3) we will see that their density of electrons is almost the same, but the mobility is lower. For zero back gate voltage we can see that (see figure 6.15(b)) between high peaks some small peaks appears. In other words, between the larger peaks, the resistance alternatingly drops to higher and lower values. This clearly shows that we have to do with a spin peak splitting. We can also calculate the density of states for different back-gate voltages. This is depicted in the table 6.1.

The last row corresponds to the values given by the institute that has grown our layers. A strange thing is that our density decreases with increasing the back-gate voltage. For the moment, we cannot explain this anormal behavior.

6.4 Other possible phenomena

This section wants to show to the reader that Ahoronov-Bohm oscillations are not the only phenomena that could be studied on such type of rings.

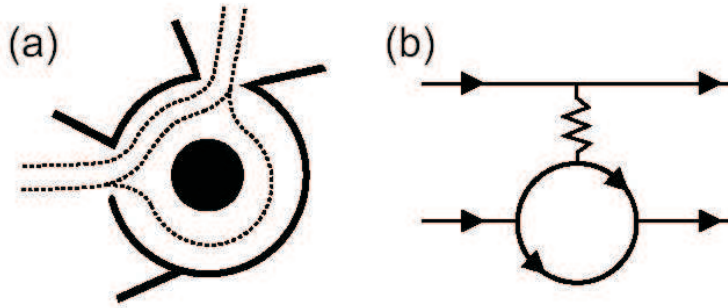


Figure 6.16: (a) Schematic picture of the ring shows the paths of the electrons in the ring that interact with the state around the center. (b) Simplified picture of conducting channels that interact with a bound state in the ring.

There are more interesting phenomena, which have not been described in this work yet. I will make a brief overview about few of them. For further information, you can consult the literature list given in the end of this work [13, 19].

6.4.1 Fano resonances

Another phenomenon which appears in a quite open regime are fano-resonances. As you see in figure 6.16(a), 2 channels (energy levels) of electrons could appear in our ring, in the upper part and one channel in the lower part (if the ring is asymmetric). These channels can create some kind of interferences between them as is depicted in figure 6.16(b).

The interference between two channels results in spectra with resonant lines shaped similar compared to some we observed in our ring. In general these lines are described by the following expression proposed by Fano in 1964 [64]:

$$S \propto \frac{(\tilde{E} + q)^2}{\tilde{E}^2 + 1} \quad (6.13)$$

q is a parameter that describes the relative phase between the two paths. $\tilde{E} = (E - E_{\text{res}})/(\hbar\Gamma/2)$ is the dimensionless detuning of the energy E of the incident electrons from the energy E_{res} of the resonant state. $\hbar\Gamma$ measures the line width of the resonances. The left-hand side figure 6.17 depicts two so-called Fano resonances for $q = 0.5$ and $q = 2$ [13]. The curves were normalized to their respective maximum S_0 . The difference in q leads to a change from a dip to a peak. A measurement of Fano resonances is depicted in figure 6.17(b) for $B = 0$ (lower curve) and $B = 320$ mT (upper curve). This so-called Fano resonances were studied in recent experiments on quantum

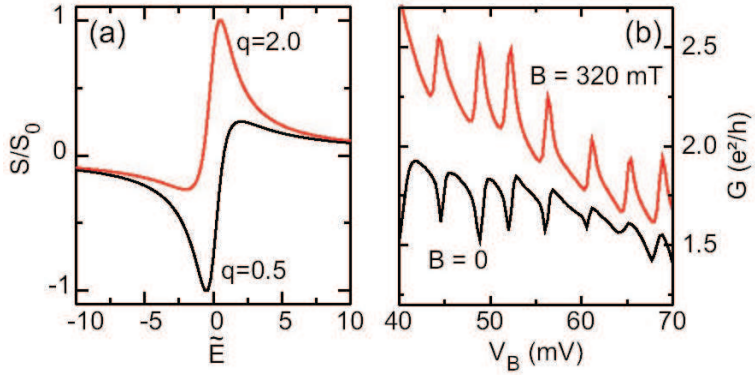


Figure 6.17: (a) Fano resonance for $q = 0.5$ (lower curve) and $q = 2$ (upper curve) as function of $E - E_{\text{res}}$. (b) Conductance $G(V_B)$ in region 1 at $B = 0$ (lower curve) and $B = 320$ mT (upper curve). The sharp dips change into maxima in the field. These Fano resonances have been measured by Felix Keyser [13].

dots see ref. [65, 66].

We tried to view this Fano resonances in our rings but there are not so good results. You can see in figure 6.18(a) the conductance as a function of U_3 and U_2 for the ring with a dot in the middle. In the middle of this plot we can see some Fano resonances. For clarity you can look in figure 6.18(b), where you have a section along the x -axis. You can see the oscillation somewhere between -200 mV and -150 mV.

6.4.2 Coulomb blockade regime

This effect could be obtained if our ring is in such a regime that it has a stable number of electrons N in it. If this regime is reached we can control the number of electrons in our ring. In addition we can study a lot of few-electron phenomena. Coulomb blockade is a quite important regime because it allows to have an overview about capacitances that are present in our gate-, source- and drain-contacts and also we can calculate from here the total capacitance of our structure. These calculations result from certain kind of measurements and plots, which have been treated in some books and papers, see ref. [19, 13].

6.4.3 Kondo effect

For strong coupling to the leads a Kondo effect is observed and used to characterize the spin structure of the system in a wide range of magnetic

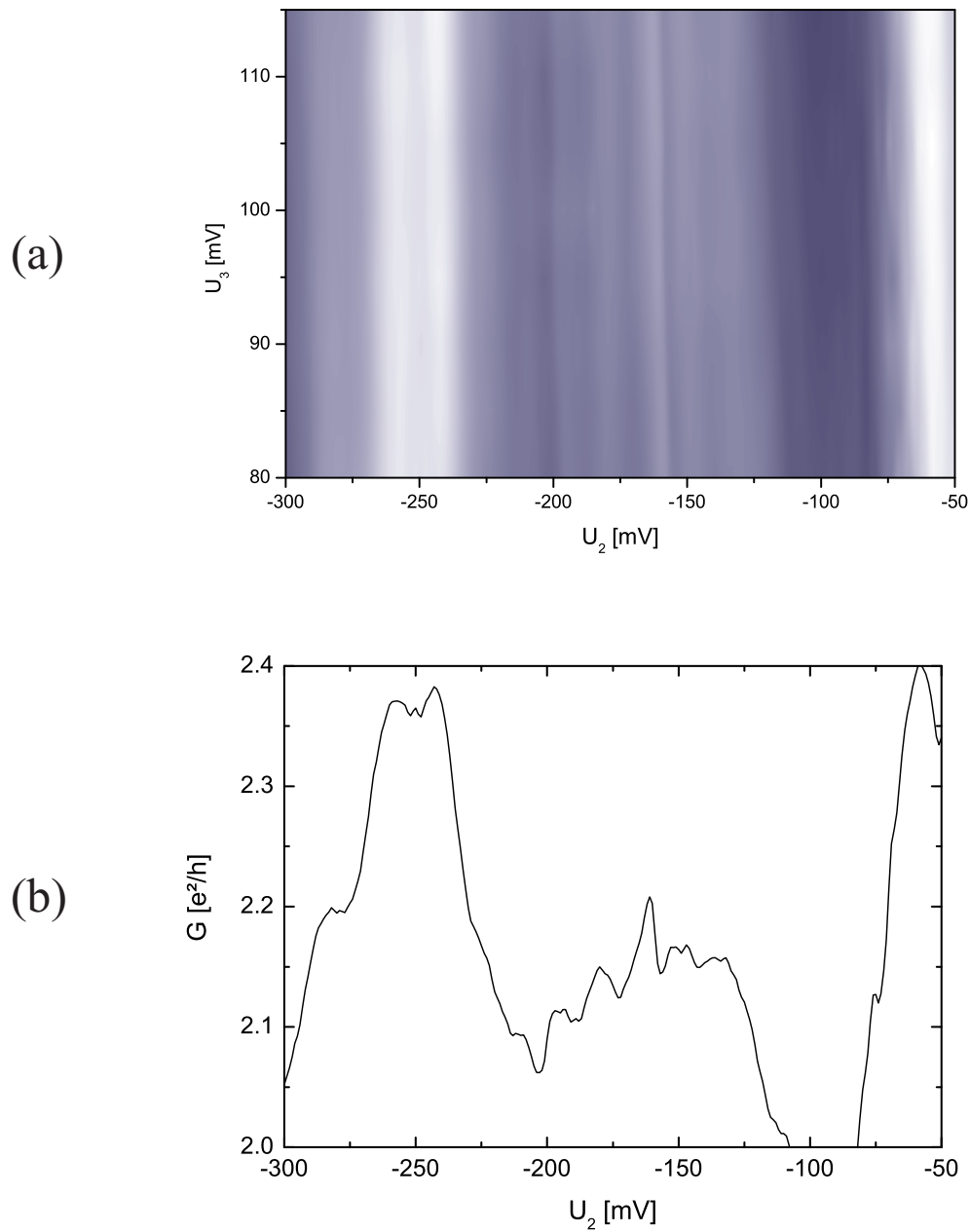


Figure 6.18: (a) The conductance G as a function of U_3 and U_2 . (b) A section along the x -axis.

fields.

In the late eighties theoretical studies predicted a Kondo effect for a quantum dot with an unpaired electron in the topmost occupied state. The tunnelling barriers of the device should become perfectly transparent with a conductance of $2(e^2/h)$ [67, 68]. The Kondo effect was discovered by Kondo and it originates from the similarities between a single quantum dot and the scattering of electrons in metals induced by diluted magnetic impurities. The resistance of a metal is enhanced by an interaction of the electrons with the spins at the magnetic impurities. This effect was first explained by Kondo in 1964 in terms of correlations in the scattering of localized spins [69]. A quantum dot with a net spin of $1/2$ acts as an "impurity" as well, but the "scattering" of electrons from the contacts leads to an enhancement of the conductance. This effect could be considered as a few-electron effect, because it acts in the Coulomb-blockade regime, where there are just several electrons in the structure. You can look to the literature list, for further details about this effect [13].

6.5 Conclusions

In this chapter you had some real measurements made on our quantum structures. In order to measure our rings, we had first to take some larger view gate-gate plots to have an idea about our rings' behavior. Our first ring (with a dot in the middle) can be controlled properly, but the second (with a ring in the middle) is almost all the time opened. In order to study the Ahoronov-Bohm effect we need an open ring, so we choose certain values for the gate voltages on base of the experiments presented before. We saw the Ahoronov-Bohm oscillations with an amplitude of about 15 % for the first ring and 3 % for the second ring. These kind of oscillations permit us to see the effective diameter of the electrons in our rings. We obtained 260 nm for the first ring and 840 nm for the second ring. These results make us thinking that our rings are working properly. We study some oscillations at different magnetic fields and at different gate voltages in order to see the phase jumps expected from the theory. We study also a temperature dependence of the oscillations for the first ring, and we notice that in our 2DEG exist just only one occupied subband with electrons.

We turned our attention to Shubnikov-de Haas oscillations made on the Hall-barr structure using the "4-points measurement" technique. These oscillations permit us to find out the density of the electrons in the 2DEG, as well as their mobility.

We finally tried to study Fano resonances and we obtained some results

for the first ring. This could be important to find some properties about the electron-electron interaction.

We presented also other possible phenomena such as Coulomb blockade or Kondo regime. The interested reader could consult the literature list for further detail.

Chapter 7

Summary

The thesis begin with an introduction that presents the place of nanoscience in nowadays. You can see the Moore's law which predicted the doubling of the transistors per chip every year. But up to when? Starting with nanostructures field, the Moore's law could be finished? During this thesis we try to find an answer to this question.

This work continues in Chapter 2 with a short theoretical overview about low-dimensional electron systems. We find out that our base in experiments is the so-called "2DEG" and it is formed because the doping profile and the layer succession of our wafer. With this support we afterwards can study the ballistic regime, which is very important in our case. It tells us that the conductance through 1D-channels is quantized in e^2/h . The supposed is used in all our measurements. Another important thing are the tunnelling barriers, that let us understand our oxide lines functioning.

After this short theoretical introduction about the basic principles, we turn our attention to the samples fabrication and to the depletion of the 2DEG presented in Chapter 3. You will find there a talk about the basis of the fabrication of heterostructures, beginning with the crystal growth using the Molecular Beam Epitaxy technique, and finishing with the bonding of the chip. The depletion process of the 2DEG using the AFM is explained. You can see that our oxide lines protrude into the GaAs surface and shift up the conductance band, over the Fermi level and the 2DEG is depleted.

With this important explanations we will have in the Chapter 4 a larger overview about the Atomic Force Microscopy Technique that let us manipulate the surface of our heterostructures and to create our quantum structures. We started to present the AFM device and to talk about its functioning. We continued with tips presentations. You can understand that the silicon tip can be better used in order to write complex structures like ours. We presented 2 writing methods: the nanomachining and the local anodic oxidation.

We used for our structures the second method that is presented in further detail.

The Chapter 5 is dedicated to the experimental procedures. We talked first about some properties of the liquid helium and we saw the big advantages offered by the liquid $^3\text{He}/^4\text{He}$ mixture technique which has a separation of phases and permit us to obtain very low temperatures of about 20 mK. A mixture cryostat that we used in our experiments is presented in the following. After this cryogenic setup, we started to present our measurement setup beginning with the sample probe and continuing with the electronic setup. You saw that the measurement setup is a quite complex system and we make very much efforts in order to reduce the noise. We used for this the lock-in technique, and convenient wires and optical separations where it is necessary. The next section presented our real sample preparation and starts with the fabrication steps of our heterostructure in the cleaning room, and continues with the writing of our quantum rings using the AFM. The AFM technique is a quite difficult one, because we have to take care in order to obtain good structures. We made many tries to obtain structures with good barriers. Our rings are presented also in this section. We created 2 ring structures. The first structure is a ring with a dot in the middle, which is smaller enough to be easy to write. It does not permit us such a good separate control of the flowing of the current through the arms of the ring, like the second structure that is a ring with another ring in the middle. This is more difficult to write but it offers a very good separate control of the different parts. The last section of this thesis contains our experimental data of this two structures, as well as that measured on the Hall-bar structure. Every studied phenomenon starts with a theoretical review followed by the real experiments. The reader can compare our measurements with the theoretical predict. The first effect is called Aharonov-Bohm oscillations. That means that if our ring is opened two conduction channels could be formed (one in the lower part and second in the upper part). This two channels could interfere at the exit of the ring and in small magnetic fields could show some oscillations. We find out that calculating the periodicity of this oscillations results in the effective diameter of the electrons inside the rings. This is a confirmation that our rings work properly. The first ring has an electronic diameter of 260 nm. The second ring has an electronic diameter of 840 nm.

These two values fit perfectly the geometry of our rings. We also studied the gate voltage dependence and the magnetic field dependence in order to see the phase jumps between oscillations which were predicted by the theory of this effect. The second phenomenon are Shubnikov-de Haas oscillations. These oscillations are a confirmation that we have a good 2DEG in our heterostructure. We apply a current along the Hall-Bar structure and we measure the resistance R_{xx} of the GaAs, while tuning the magnetic field. We observed certain oscillations with a periodicity that increases in time. $R_{xx}(1/B)$ gives us a plot with a constant period. This period helps us to calculate the density of the electrons in our 2DEG and the mobility of the electrons. We also tried to view some Fano resonances. This kind of resonances appears if our ring is asymmetrically opened. This means one gate more positive than the other. In this case two conducting channels could be formed, in the one side of the ring while the other side could remain with only one channel. These channels could interfere and give some oscillations called Fano resonances. In a small range for gate voltage of our first ring, we can see these Fano resonances. These studied phenomena are not the only ones possible. We made a short description of other effects like Coulomb Blokade regime or Kondo regime. Some further details about this effects can be found in the specific literature listed at the end of this work.

So, after all this "stuff" we can remain with an important idea. With the AFM-based lithography it should be possible to design novel geometries for mesoscopic systems, which show an unexpected variety of new effects in transport experiments. This is a very fascinating research field, because it is so new that people discover every day new geometries with new properties, and besides that there is an exciting field because you cannot make exact rules. If you think that you have just discovered something new, the next apparently identical structure will be different.

Appendix A

The lithoscript-programs

You will find in this appendix, the lithoscript-programs for writing both quantum ring structures.

The ring with a dot in the middle

This lithoscript-program is used to write a quantum-ring structure with a dot in the middle (see figure 5.13(a)).

```
//The ring with a dot in the middle
#include<litho.h>
#include<hwlit423.h>
#include<litcurv5.h>

void main()
{
    double rate=0.25;                                //writing speed
    double r=0.25;                                   //radius of arc
    double p=2;                                     //pause

    //The upper part
    LITHO_BEGIN
        LithoSetOutput(aoAna2,10);                  //Relais off
        LithoTranslate(0,1.25,rate);
        LithoPause(p);
        LithoSetOutput(aoAna2,-9);                  //Relais on
        LithoTranslate(0,-1,rate);
        LithoCircleArc(90,135,TRUE,r,rate);
}
```

```

        LithoAngLine(1,135,rate);
        LithoSetOutput(aoAna2,10);                                //Relais off
LITHO_END

//The middle part
LITHO_BEGIN
        LithoSetOutput(aoAna2,10);                                //Relais off
        //LithoTranslate(0.025,-0.025,rate);
        LithoPause(p);
        LithoSetOutput(aoAna2,-9);                                //Relais on
        LithoPause(1.5);
        LithoSetOutput(aoAna2,10);                                //Relais off
LITHO_END

//The lower part
LITHO_BEGIN
        LithoSetOutput(aoAna2,10);                                //Relais off
        LithoTranslate(-1.25,0,rate);
        LithoPause(p);
        LithoSetOutput(aoAna2,-9);                                //Relais on
        LithoTranslate(1,0,rate);
        LithoCircleArc(180,45, FALSE, r,rate);
        LithoAngLine(1,45,rate);
        LithoSetOutput(aoAna2,10);                                //Relais off
LITHO_END

LITHO_BEGIN
        LithoSetOutput(aoAna2,10);                                //Relais off
        LithoAngLine(0.3,25,rate);
        LithoPause(p);
        LithoSetOutput(aoAna2,-9);                                //Relais on
        LithoTranslate(1,0,rate);
        LithoSetOutput(aoAna2,10);                                //Relais off
LITHO_END

LITHO_BEGIN
        LithoSetOutput(aoAna2,10);                                //Relais off
        LithoAngLine(0.3,200,rate);
        LithoPause(p);
        LithoSetOutput(aoAna2,-9);                                //Relais on
        LithoAngLine(1,225,rate);

```

```

    LithoSetOutput(aoAna2,10);           //Relais off
LITHO_END

}

```

The ring with a ring in the middle

This lithoscript-program is used to write a quantum-ring structure with another ring in the middle (see figure 5.13(b)).

```

//The ring with a ring in the middle
#include<litho.h>
#include<hwlit423.h>
#include<litcurv.h>

void main()
{
    double rate=0.25;                      //writing speed
    double rh=0.5;                         //radius of larger arc
    double rl=0.23;                         //radius of smaller arc
    double p=3;                            //pause

    //The upper part
    LITHO_BEGIN
        LithoSetOutput(aoAna2,10);           //Relais off
        LithoTranslate(0,0.5,rate);
        LithoTranslate(0.01,0.01,rate);       //write corection
        //LithoAngLine(0.06,312,rate);        //write corection
        LithoAngLine(1,115,rate);
        LithoTranslate(0,0.5,rate);
        LithoPause(p);
        LithoSetOutput(aoAna2,-9);           //Relais on
        LithoTranslate(0,-0.5,rate);
        LithoAngLine(1,295,rate);
        LithoCircleArc(90,160,0,rh,rate);
        LithoAngLine(1,135,rate);
        LithoAngLine(0.5,155,rate);
        LithoSetOutput(aoAna2,10);           //Relais off
    LITHO_END
}

```

```

//The lower part
LITHO_BEGIN
    LithoSetOutput(aoAna2,10);           //Relais off
    //LithoTranslate(0.02,-0.03,rate);    //write correction
    LithoTranslate(-1.5,0,rate);
    LithoAngLine(0.5,225,rate);
    LithoPause(p);
    LithoSetOutput(aoAna2,-9);           //Relais on
    LithoAngLine(0.5,45,rate);
    LithoTranslate(1,0,rate);
    LithoCircleArc(180,70,TRUE,rh,rate);
    LithoAngLine(1,70,rate);
    LithoTranslate(0.5,0,rate);
    LithoSetOutput(aoAna2,10);           //Relais off
LITHO_END

LITHO_BEGIN
    LithoSetOutput(aoAna2,10);           //Relais off
    LithoAngLine(0.5,50,rate);
    LithoPause(p);
    LithoSetOutput(aoAna2,-9);           //Relais on
    LithoAngLine(1,25,rate);
    LithoAngLine(0.5,340,rate);
    LithoSetOutput(aoAna2,10);           //Relais off
LITHO_END

LITHO_BEGIN
    LithoSetOutput(aoAna2,10);           //Relais off
    LithoAngLine(0.5,200,rate);
    LithoPause(p);
    LithoSetOutput(aoAna2,-9);           //Relais on
    LithoAngLine(1,225,rate);
    LithoTranslate(0,-0.5,rate);
    LithoSetOutput(aoAna2,10);           //Relais off
LITHO_END

//The middle part
LITHO_BEGIN
    LithoSetOutput(aoAna2,10);           //Relais off
    LithoTranslate(-0.02,0.02,rate);    //write correction

```

```

    LithoTranslate(0.25,0,rate);
    LithoPause(p);
    LithoSetOutput(aoAna2,-9);                                //Relais on
    LithoCircleArc(0,360, FALSE, rl,rate);
    LithoSetOutput(aoAna2,10);                                //Relais off
LITHO_END

}

```

The library <litcurv.h>

The commands "LithoCircleArc" (for writing any curves) and "LithoAngleLine" (for writing any angle lines) belong to a library called <litcurv.h>, which was written by us and is presented in the following.

```

#include<litho.h>
#include<math.h>
void LithoCircleArc(int start, int end, bool clockwise,
                     double r, double rate)
{
    int i;
    double pi = 2*acos(0);
    double phi;
    double alpha;
    int deg=5;
    double dphi = deg*pi/180;
    double d=2*r*sin(dphi/2);

    if(clockwise)
    {
        if(start<end)
        {
            end=end-360;
        };
        for(i=start;i>end;i=i-deg)
        {
            phi=i*pi/180;
            alpha=(dphi/2)+(pi/2)+phi;
            LithoTranslate(-d*cos(alpha),-d*sin(alpha),rate);
        };
    };
}

```

```
    }
    else
    {
        if(start>end)
            start=start-360;
        for(i=start;i<end;i=i+deg)
        {
            phi=i*pi/180;
            alpha=(dphi/2)+(pi/2)+phi;
            LithoTranslate(d*cos(alpha),d*sin(alpha),rate);
        };
    };
}

void LithoAngLine(double d, double alpha, double rate)
{
    double pi = 2*acos(0);
    LithoTranslate(d*cos(alpha*pi/180),d*sin(alpha*pi/180),rate);
}
```

Appendix B

Symbols and abbreviations

You will find in this appendix, a list with all the symbols and abbreviations used in this work.

2DEG	Two Dimensional Electron Gas
nD	n -dimensional electron system
AFM	Atomic Force Microscope
D	Drain contact of a sample
IPG	In-Plane Gates
LAO	Local anodic oxidation
LL	Landau Level
MBE	Molecular Beam Epitaxy
QD	Quantum Dot
QPC	Quantum Point Contact
rel. H	Relative humidity
S	Source contact of a sample
SEM	Scanning Electron Microscope
SPM	Scanning Probe Microscope
STM	Scanning Tunnelling Microscope
\vec{A}	Vector potential
α	Voltage to energy conversion factor
B	Magnetic Field
C_{Σ}	Overall capacitance of a quantum dot
C_i	Capacitance between gate i and the quantum dot
C_S	Capacitance between source and quantum dot
C_D	Capacitance between drain and quantum dot
χ	Arm length of an Aharonov-Bohm ring in multiples of π
D	Depth of an oxide line

d_e	Electronic diameter of an Aharonov-Bohm ring
D_e	Electronic diameter of a quantum dot
DOS	Density of states
E	Energy for electrons
e	Elementary charge
E_C	Conduction band edge
E_F	Fermi energy
E_r	Energy of a 1D-subband relative to E_F
E_S	Single-particle energy level on a quantum dot
E_V	Valence band edge
ε	Energetic distance between $\mu_{QD}(N)$ and μ_S
ϵ	Coupling coefficient for a ring interferometer
f	Frequency of the Aharonov-Bohm oscillations
$f(E)$	Fermi-Dirac distribution
f_0	Ground frequency of our Aharonov-Bohm ring
F_C	Contact force between AFM tip and sample
Φ_0	Height of a tunnelling barrier above E_C
Φ^{eff}	Effective barrier height above $\mu_{S,D}$
$\Phi_0 = h/e$	Magnetic flux quantum
Φ	Magnetic flux
G	Linear conductance through a sample ($V_{SD} = 0$)
G_0	Conductance at $V_{SD} = 0$
H	Height of an oxide line
h	Planck constant
\hbar	$h/2\pi$
I_{SD}	Source-Drain current through a sample
I_{ox}	Oxidation current flowing between AFM tip and sample
k	Spring constant of the cantilever
\vec{k}	Wave vector of an electron
k_i	i-th component of the wave vector
k_F	Wave number at E_F
$\delta = k_F \Delta L$	Phase difference between the ring arms
k_B	Boltzmann constant
ΔL	Length difference of the arms of an Aharonov-Bohm ring
l	Angular momentum quantum number
λ_F	Wavelength of the electrons at E_F
l_{1D}	Length of a quantum wire
l_e	Mean-free pass of an electron
l_Φ	Phase coherence length
m^*	Effective mass of an electron

μ_e	Mobility of a 2DEG
μ_s	Electrochemical potential in the source contact
μ_d	Electrochemical potential in the drain contact
$\mu_{QD}(N)$	Electrochemical potential of a quantum dot
N	Number of electrons on a quantum dot
n_e	Electron density in a 2DEG
N_{Scan}	Number of scan lines for controlled nanomachining
ν	Filling factor in a magnetic field
Ψ	Electronic wave function
R	Resistance of a sample
T	Absolute temperature
T_n	Transmission through the n -th subband of a QPC
t	Transmission coefficient
T_b	Base temperature of the dilution cryostat
Θ	Heaviside function
$U = eV_{SD,U}$	Charging energy of a quantum dot
V	Voltage applied to a sample
V_i	Voltage applied to gate i
V_{ox}	Oxidation voltage applied to the AFM tip
V_{SD}	Source-drain voltage
v_n	Velocity of an electron in the n -th subband
v_{tip}	Tip velocity during the oxidation with an AFM
w	Width of a tunnelling barrier
w_{1D}	Width of a point contact
$w_{dpl,x}$	Depletion width for a nanomachined line

Curriculum Vitae

NAME: Vlad-Andrei ANTOHE
DATE OF BIRTH: 11.October.1979
ADDRESS: Vicina Street, No. 2, Bl. 29, Sc. 1, Et. 1, Ap.7,
Sect.5, Bucharest, Romania
NATIONALITY: Romanian
TELEPHONE: home: +4021.423.60.14
mobile: +4723.666.907
E-MAIL: *vlad_antoh@ yahoo.com*
vlad@solid.fizica.unibuc.ro
LANGUAGES: fluent English
COMPUTER LITERACY: Microsoft Windows 98/2000/XP, Linux, Turbo Pascal,
Borland C++, Microsoft Office, Microcal Origin, Matlab,
LabView, Computer Networks

EDUCATION: 1994-1998 Horia Hulubei High School, Bucharest
Computational Technics Diploma, series A,
no. 204337, issued by the Romanian Education
and Science Ministry, 3.August.1998
1998-2002 Faculty of Physics, University of Bucharest,
B. Sc. Physics
1998-2003 Faculty of Electronics and Telecommunications,
Polytechnic University, Diploma of Engineer
2003- Faculty of Physics, University of Bucharest,
Master Degree Programme in Electronics and
Metrology

SCIENTIFIC ACTIVITY:

FIELDS: Semiconductor Devices (Field Effect Transistors, Photovoltaic Cells), Thin Layers of AII-BVI Compounds (CdS, CdSe, CdTe)

PUBLICATIONS: *Electrical Properties of Non – Irradiated and Electron Irradiated Thin Polycrystalline CdSe layers* [70]
The structural and Electrical Properties of Thin Polycrystalline CdSe and CdS Layers Before and After Electron Irradiation [71]
The Effect of the Electron Irradiation on the Structural and Electrical Properties of AII – BVI Thin Polycrystalline Films [72]
The Study of the Defects Induced by High Energy Electron Irradiation in CdSe Thin Films [73]
The Effect of the Electron Irradiation on the Electrical Properties of A2 – B6 Thin Polycrystalline Layers : A Review [74]
Thermally Stimulated Current Measurements Applied to Study of Electron – Irradiation Induced Defects in CdSe Thin Films [75]

INTERESTS: Solid State Physics, Nanostructures Physics (Microscopic and Mesoscopic Devices), Physical Electronic, Electronic Devices and Circuits, High-frequency systems, Telecommunication Equipments, Multimedia Equipments (especially Dither Effect in Digital Audio Systems).

Bibliography

- [1] J.S. WILLIAMS, H.H. Tan P. Lever J. Wong-Leung ; JAGADISH, C.: Production and Processing of Semiconductor Nanocrystals and Nanostructures for Photonic Applications. In: *Materials Forum* 26 (2002), S. 74–80
- [2] *Spin and Charge Transport in Nanostructures.* – URL: <http://www.gfct.fisica.uminho.pt/sctn2003/textos/sctn2003.html>
- [3] URL: <http://uw.physics.wisc.edu/~himp sel/nano.html>
- [4] ZOZOULENKO, Igor: *Introduction to Mesoscopic Physics.* – URL: <http://www.ifm.liu.se/igorz/mes.html>
- [5] SIVAKUMAR, Vikram: *Nanotechnology - An Introduction.* – URL: <http://metallurgy.iitm.ac.in/metsa/etch/nanotech.htm>
- [6] BRUUS, Henrik: *Introduction to Nanotechnology.* Lingby, 2004
- [7] MOORE, G. E.: Cramming more Components onto Integrated Circuits. In: *Electronics* 38 (1965)
- [8] R. DINGLE, A. C. G. ; WIEGMANN, W.: In: *Appl. Phys. Lett.* 33 (1978), S. 665
- [9] BINNING, G. ; ROHRER, H.: In: *Hel. Phys. Acta* 55 (1982), S. 726
- [10] EIGLER, D. M. ; SCHWEIZER, E. K.: In: *Nature* 344 (1990), S. 524
- [11] G. BINNING, C. F. Q. ; GERBER, C.: In: *Phys. Rev. Lett.* 56 (1986), S. 930
- [12] ISHII, M. ; MATSUMOTO, K.: In: *Jpn. J. Appl. Phys.* 34 (1995), S. 1329

- [13] KEYSER, Ulrich F.: *Nanolitography with an Atomic Force Microscope: Quantum Point Contacts, Quantum Dots, and Quantum Rings*, Universität Hannover, Inst. f. Festkörperphysik, Abt. Nanostrukturen, PhD thesis, 2002
- [14] KOUWENHOVEN, L.: *Transport of Electron-Waves and Single-Charges in Semiconductor Nanostructures*, Technische Universiteit Delft, Netherlands, PhD thesis, 1992
- [15] SHARVIN, Y. V.: In: *JETP* 21 (1965), S. 848
- [16] C. COHEN-TANOUJDJI, B. D. ; LALOË, F.: *Quantenmechanik*. 1997
- [17] PECK, A. J.: *Lateral Tunnelling in Two-Dimensional Electron Systems*, University of Bath, PhD thesis, 1994
- [18] SCHUMACHER, H. W.: *Nanostrukturierung mit dem Rasterkraft-Mikroskop: Vom Zweidimensionalen Elektronengas zum Einzelelektron-transistor*, Universität Hannover, Germany, PhD thesis, 2000
- [19] *Mesoscopic Electronics in Solid State Nanostructures*. Wiley-VCH GmbH and Co.KGaA, 2003
- [20] *Cleaning Room*. – URL: <http://www.nanostructures.com/Clean%20Room.htm> :
- [21] ADACHI, S.: *Properties of Aluminium Gallium Arsenide*. 1993
- [22] WINSTON, D.: *SimWindows Semiconductor Device Simulator 1.5.0*
- [23] H. VAN HOUTEN, M. G. J. H. ; ANDRE, J. P.: In: *Appl. Phys. Lett.* 49 (1986), S. 1781
- [24] RILEY, Peter: *Atomic Force Microscopy*. – URL: <http://www.pace.leeds.ac.uk/labs/afm.htm> :
- [25] ROUND, Andy: *Atomic Force Microscopy*. – URL: <http://spm.phy.bris.ac.uk/techniques/AFM/>
- [26] LI, Hong-Qiang: *Atomic Force Microscopy*. – URL: <http://www.chembio.uoguelph.ca/educmat/chm729/afm/firstpag.htm>
- [27] JIN, X. ; UNERTL, W. N.: In: *Appl. Phys. Lett.* 61 (1992), S. 657
- [28] H. FUCHS, L. M. E. ; GRAF, K.: *Thin Solid Films*. 210-211 (1992), S. 655

- [29] E. MEYER, R. Lüthi D. Brodbeck L. Howald J. Frommer H. J. Gütterodt O. Wolter M. Fujihara H. T. ; GOTOH, Y.: Thin Solid Films. 220 (1992), S. 1132
- [30] T. SUMOMOGI, K. Kuwhara R. K. ; MIYAMOTO, T.: In: *J. Vac. Sci. Technol.* B 12 (1994), S. 1876
- [31] KIM, Y. ; LIEBER, C. M.: In: *Science* 257 (1992), S. 375
- [32] M. WENDEL, H. Lorenz J. P. K. ; HOLLAND, M.: In: *Appl. Phys. Lett.* 65 (1994), S. 1775
- [33] BOUCHIAT, V. ; ESTEVE, D.: In: *Appl. Phys. Lett.* 69 (1996), S. 3098
- [34] MAGNO, R. ; BENNETT, B. R.: In: *Appl. Phys. Lett.* 70 (1997), S. 1855
- [35] J. C. ROSA, H. Lorenz J. P. Kotthaus M. T. ; KROEMER, H.: In: *Appl. Phys. Lett.* 73 (1998), S. 2684
- [36] H. W. SCHUMACHER, U. Zeitler R. J. H. ; EBERL, K.: In: *Appl. Phys. Lett.* 75 (1999), S. 1107
- [37] E. OESTERSCHULZE, U. F. Keyser M. P. ; HAUG, R. J.: Diamond and Related materials. 11 (2002), S. 667
- [38] GHANDHI, S. K.: In: *VLSI Fabrication Principles, 2nd. ed.* (1994)
- [39] KEYSER, Ulrich F., Universität Hannover, Germany, Diploma thesis, 1999
- [40] P. M. CAMPBELL, E. S. S. ; McMARR, P. J.: In: *Appl. Phys. Lett.* 66 (1994), S. 1388
- [41] E. S. SNOW, P. M. C.: In: *Science* 270 (1995), S. 1670
- [42] E. S. SNOW, D. P. ; CAMPBELL, P. M.: In: *Appl. Phys. Lett.* 69 (1996), S. 269
- [43] E. S. SNOW, R. W. Rendell F. A. Buot D. Park C. R. K. M. ; MAGNO, R.: In: *Appl. Phys. Lett.* 72 (1998), S. 3071
- [44] I. OKADA, M. Kawabe B. N. S. ; HARRIS, J. S.: In: *Jr. Elec. Lett.* 75 (1999), S. 1107
- [45] R. HELD, T. Heinzel K. Ensslin M. H. ; WEGSCHEIDER, W.: In: *Appl. Phys. Lett.* 73 (1998), S. 262

- [46] U. F. KEYSER, U. Zeitler R.J. H. ; EBERL, K.: In: *Appl. Phys. Lett.* 76 (2000), S. 457
- [47] N. J. CURSON, N. J. Appleyard M. Pepper D. A. R. ; JONES, G. A. C.: In: *Appl. Phys. Lett.* 78 (2001), S. 3466
- [48] SEEGER, K.: *Semiconductor Physics, an Introduction.* 1999
- [49] AHARONOV, Y. ; BOHM, D.: In: *Phys. Lett. Rev.* 115 (1959), S. 485
- [50] CHAMBERS, R.G.: In: *Phys. Rev. Lett.* 5 (1960), S. 3
- [51] R. A. WEBB, C. P. U. ; LAIBOWITZ, R. B.: In: *Phys. Rev. Lett.* 54 (1985), S. 2696
- [52] K. ISMAIL, S. W. ; LEE, K. Y.: In: *Appl. Phys. Lett.* 59 (1991), S. 1998
- [53] G. CERNICCHIARO, K. Hasselbach D. M. ; BENOIT, A.: In: *Phys. Rev. Lett.* 79 (1997), S. 273
- [54] S. PEDERSEN, A. Kristensen C. B. S. ; LINDELOF, P. E.: In: *Phys. Rev. B* 61 (2000), S. 5457
- [55] M. CASSÉ, G. M. Gusev E. B. Olshanetskii L. V. Litvin A. V. Plotnikov D. K. M. ; PORTAL, J. C.: In: *Phys. Rev.* 62 (2000), S. 2624
- [56] V. PIAZZA, W. Wegschieder C. T. L. ; PEPPER, M.: In: *Phys. Rev. B* 62 (2000), S. R10630
- [57] M. BÜTTIKER, Y. I. ; AZBEL, M. Y.: In: *Phys. Rev. B* 30 (1984), S. 1982
- [58] PEDERSEN, S.: *Aharonov-Bohm experiments in mesoscopic systems*, Niels Bohr Institute, University of Copenhagen, Denmark, PhD thesis, 1999
- [59] E. BUKUS, M. Heiblum D. M. ; UMANSKY, V.: In: *Nature* 391 (1998), S. 871
- [60] K. V. KLITZING, G. D. ; PEPPER, M.: In: *Phys. Rev. Lett.* 45 (1980), S. 494
- [61] R. WILLETT, H. L. Strmer D. C. Tsui A. C. G. ; ENGLISH, J. H.: In: *Phys. Rev. Lett.* 59 (1987), S. 1987
- [62] QUINN, T.: In: *Metrologia* 26 (1989), S. 69

- [63] D. C. TSUI, H. L. S. ; GOSSARD, A. C.: In: *Phys. Rev. Lett.* 48 (1982), S. 1559
- [64] FANO, U. ; COOPER, J. W.: In: *Phys. Rev.* 137 (1964), S. A1364
- [65] J. GÖRES, S. Heemeyer M. A. Kastner H. Shrikman D. M. ; MEIRAV, U.: In: *Phys. Rev. B* 62 (2000), S. 2188
- [66] I. G. ZACHARIA, G. Granger M. A. Kastner Y. B. Khavin H. Shtrikman D. M. ; MEIRAV, U.: In: *Phys. Rev. B* 64 (2001), S. 155311
- [67] GLAZMAN, L. I. ; RAIKH, M. E.: In: *JETP Lett.* 47 (1988), S. 452
- [68] NG, T. K. ; LEE, P. A.: In: *Phys. Rev. Lett.* 61 (1988), S. 1768
- [69] KONDO, J.: In: *Progress of theoretical Physics* 32 (1964), S. 37
- [70] V. ANTOHE, S. Antohe R. Schiopu V. R.: Electrical Properties of Non-Irradiated and Electron Irradiated Thin Polycrystalline CdSe layers. In: *Romania Reports in Physics* 53 (2001), S. 451–459
- [71] V. ANTOHE, L. I.: The structural and Electrical Properties of Thin Polycrystalline CdSe and CdS Layers Before and After Electron Irradiation. In: *Rom. Journ. Phys. Supplement I* 48 (2003), S. 511–519
- [72] V. ANTOHE, S. A.: The Effect of the Electron Irradiation on the Structural and Electrical Properties of $A^{II} - B^{VI}$ Thin Polycrystalline Films. In: *Journal of Optoelectronics and Advanced Materials* 5 (2003), S. 801–816
- [73] V. ANTOHE, S. Antohe D. Tutuc L. Ion C. T.: The Study of the Defects Induced by High Energy Electron Irradiation in CdSe Thin Films. In: *SUMMER SCHOOL on Physics of Advanced Materials* June 28-July 9 (2004)
- [74] V. ANTOHE, S. Antohe L. I.: The Effect of the Electron Irradiation on the Electrical Properties of A2-B6 Thin Polycrystalline Layers: A Review. In: *Annual Scientific Conference - Program and Abstracts* May 31 (2002)
- [75] V. ANTOHE, S. Antohe L. Ion M. Ghenescu H. A.: Thermally Stimulated Current Measurements Applied to Study of Electron-Irradiation Induced Defects in CdSe Thin Films. In: *Abstracts Book of 5-th International Balkan WORKSHOP on Applied Physics* July 5-7 (2004), S. 44